Department of Engineering Science

MSc by research in engineering

An investigation on the Bauschinger effect in titanium alloys for aerospace applications: strain rate and pressure dependence

Nil Constans Sole

St Anne's college

2021

Supervisors:

Nik Petrinic

Antonio Pellegrino

Contents

Abbreviations and acronyms

B.E.	Bauschinger effect
C-T	Compression followed by tension
T-C	Tension followed by compression
RL	Reverse loading
SHB	Split Hopkinson bar
Ti64	Ti-6Al-4V
DIC	Digital image correlation
Ti	Titanium
CP	Commercially pure
SD	Strength differential
HR	High strain rate
QS	Quasi-static strain rate

List of Figures

Abstract

A comprehensive study of the reverse loading in Ti-6Al-4V hereafter, Ti64 alloys including strain rate and pressure effects (strength differential), is conducted in order to improve the understanding of the deformation mechanisms in Ti64 and characterise its Bauschinger effect.

Strain controlled quasi-static, and high strain rate reverse loading tests are performed, providing novel data to conduct a series of explicit finite element (FEA) simulations with the objective to determine the capabilities of widely used constitutive models to predict the material response under cyclic loading.

The analysis of the experimental data shows that the Bauschinger effect (B.E.) in the material is manifested principally as the loss of a distinct transition between elastic and plastic dominated deformation regions (transient softening), leading to the lowering of the plastic work expended during the straining of the material.

The analysis of the strain rate effects on the cyclic response of the material, allows to identify an inversely proportional relationship between strain rate and B.E. as well as a higher prominence of the aforementioned drop in the plastic work when the loading is conducted in the opposite direction to the pre-strain.

The numerical study conducted shows that general, widely used constitutive models calibrated with monotonic data are not able to accurately predict the cyclic loading response of Ti-6Al-4V alloys, proving the importance of the Bauschinger effect as factor to consider in order to obtain reliable models of the material's response to complex loading.

1. Introduction and objectives

Most of the studies concerning the mechanical behaviour of materials traditionally focus on the material response during simple, monotonic loading. However, in recent years, the study of the mechanical response under more complex loading paths has gained great relevance for a broad spectrum of applications and fields of research, particularly for metallic materials. Not only because it allows for a better representation of the service conditions to which parts and components are exposed, but also because studying the response of metals to more complex loading cases, such as reverse loading, is essential to fully characterise their plastic behaviour and the mechanisms behind work hardening [1]. A better understanding of the response of metals to reverse loading can, therefore, result in substantial improvements in several industrial design applications relevant to the metal forming, petrochemical and transportation (automotive, aerospace, etc.) industries [2–4], among others.

In the case of the aerospace industry, where impact is often the most critical load case, it becomes necessary to take into consideration also the effects of strain-rate, pressure, and temperature. Titanium alloys are of particular interest in this field, because of their specific strength and stiffness, manufacturing properties, and chemical stability, which gives them very good resistance to high temperatures and corrosion, making them ideal for use in aero-engines, gas turbines and other highly demanding applications [2]. However, much of the work done to characterise and understand the mechanical response of these materials has been focused on monotonic loading conditions. Therefore, a better understanding of their response to impulsive loading is crucial to the current weight and cost reduction effort within the aerospace industry. More specifically, studies on the reverse loading response of these materials at high strain rates will allow for further investigation into the effects and consequences of reflected stress waves, which is one of the main causes of dynamic failure [1], on their mechanical response and integrity. This can be further illustrated by some specific aero engine design applications and

scenarios, such as trailing blade, containment damage and damage caused by foreign objects (FOD) [3], where materials are subjected to dynamic reverse loading conditions, affecting their mechanical response and occasionally leading to premature and unexpected failure. Because of the above, the development of dynamic reverse loading experimental techniques and constitutive modelling are topics of great importance.

The focus of this project is, therefore, the characterisation of the mechanical response of aerospace materials under quasi-static and dynamic reverse loading. More specifically, the Ti64 alloy, of particular interest for the aerospace industry, is investigated. However, this goal poses several technical challenges. While the response of metals under monotonic and high-cycle fatigue loading at different strain rates is a largely covered topic in the literature, the current knowledge on their behaviour under low-cycle high-strain reverse loading still poses a challenge and requires further investigation, even more so at high strain-rates.

The main reason for this is the technical difficulty in developing experimental techniques able to provide reliable data for reverse loading conditions of this kind. In dynamic reverse loading, the gap time between forward and reverse load has a direct effect on the material response due to adiabatic heating effects [5]. This fact means that, in order to obtain valid data, it is necessary that the loading cycles have the lowest possible pause between the forward and reverse steps.

All of this adds up to make experimental studies of the high-strain rate, reverse loading behaviour of materials a very complex task that has rarely been assessed in literature [4]. While some work has been done on the development of reversible Split-Hopkinson bar systems [1,6], these still face technical limitations, mainly on their ability to obtain dynamic equilibrium, the controllability of the strains generated by the system, as well as their effectiveness at lower strains. Chapter 2.1.1 expands on their characteristics and limitations.

With all of this in mind, the main goal of this study is to contribute to the better understanding of reverse loading behaviour in Ti-6Al-4V alloys using novel experimental techniques that allow for the comprehensive study of the influence of strain rate on the Bauschinger effect and, with the data acquired, calibrate some of the leading constitutive models for this material and evaluate their performance under such complex loading conditions.

The work carried out in this study is described in the following chapters, starting with a review of the relevant literature in chapter 2 and continuing to the novel experimental and numerical work done to investigate this phenomenon in chapters 3 and 4. The experimental work at both quasi-static and high strain-rates is described in chapter 3, while chapter 4 contains a deeper analysis of the experimental results and additional numerical modelling work, including the evaluation of leading constitutive models for Ti64. Finally, conclusions are given in chapters 5 and chapter 6 contains areas identified for future research.

2. Literature review

The literature relevant to this project falls into four main categories following the objectives set out above:

- Experimental techniques: reverse loading at different strain-rates
- Review of the Bauschinger effect on metallic materials
- Characteristics and deformation mechanisms of Ti-6Al-4V
- Current constitutive modelling techniques of B.E.

2.1 Experimental reverse loading techniques

The following review is focused mainly on experimental techniques used to study the effect of reverse loading on the plastic behaviour in metals, known as Bauschinger effect. These can be classified depending on the regime in which the testing occurs: quasi-static, and dynamic loading techniques. Testing in the quasi-static regime can be done by strain-controlled loading using universal testing machines and hydraulic testing machines with specially designed specimen geometries. For reverse loading at high strain rates, on the other hand, more advanced experimental techniques, such as modified split-Hopkinson pressure bars, are required.

2.1.1 Quasi static loading

The first works dedicated to the study of reverse loading and Bauschinger effect in metals relied on much simpler strategies based on the concatenation of monotonic loading tests, which showed very poor results and led to conclusions later proven false [7], such as the strain rate independency of B.E. reported by Nevill and Myers [8]. Since, techniques that allow the completion of load cycles without interruption between load directions have been standard [9].

These techniques eliminate the necessity of using critical dimensions for tension-compression specimens and the uncertainties involved in machining compression out of tensile specimens, as in [7,8], which risks altering the microstructure. Uninterrupted reverse loading techniques also allow usage of the same geometry in tension and compression tests avoiding the influence of geometric effects [10].

Traditionally the use of a unique geometry in tension and compression testing was avoided due to barrelling and geometric section changes during testing [11]. Nowadays, however, these limitations can be overcome through direct measurement of strains using full field strain visualization techniques, such as DIC (digital image correlation). Thanks to these advances, more recent studies on reverse loading and B.E. have had good success using strain controlled testing [2,10].The study of B.E at quasi-static loading rates is, therefore, relatively mature, with the much greater challenge being its study at high strain-rates.

2.1.2 Dynamic loading

The only currently known experimental techniques that allow cyclic dynamic testing in a single step are techniques based on the split Hopkinson bar (SHB).

Split Hopkinson pressure bars, also referred as Davies bar or Kolsky bar [1,12–14] consist of two symmetrical, input and output bars with a specimen between them, where the dynamic stress-strain response of the material will be measured *Figure 2* show the diagrams of the experimental rig of a compression and of a tension SHB [10]. A controlled compressive or tensile pulse (depending on the loading mode of the specific bar in question) is generated by the impact of a projectile with the input/incident bar. The stress wave generated by this pulse propagates along the input bar until it reaches the specimen. At the interface, part of the pulse is transmitted through to the specimen and the other part is reflected back from the free end

surface of the input bar. The transmitted pulse propagates through the specimen and is again partially reflected at the interface within the output bar. The reflected pulse in the specimen bounces back and forth and establishes a state of stress equilibrium, ideal for the specimen to deform at constant strain-rate. The elastic displacements measured by the strain gauges on the input and output bars are used to determine the stress-strain conditions at the end of the sample.

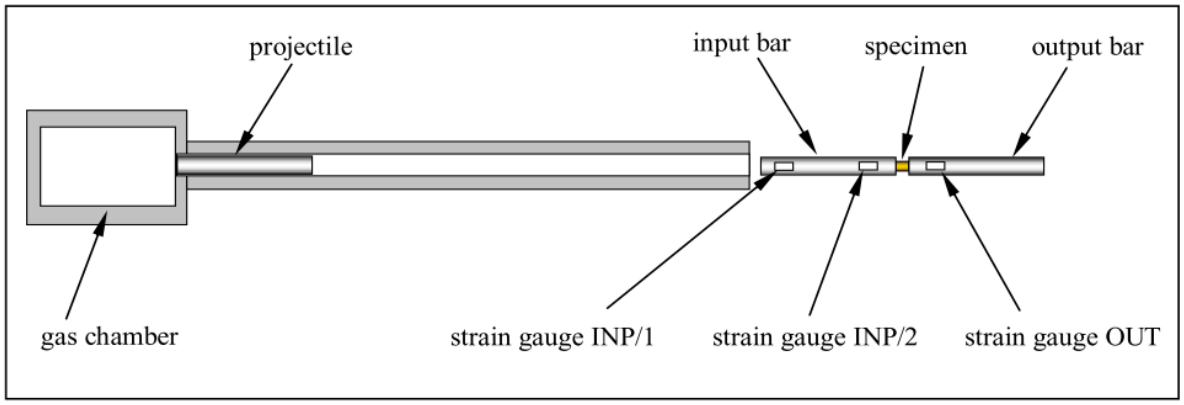

Figure 1 Monotonic compression SHB configuration [10]

.

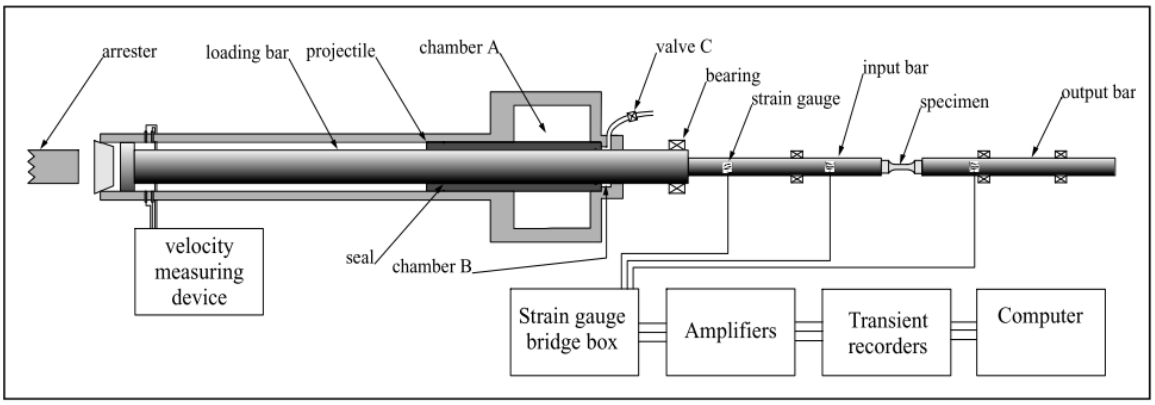

Figure 2 Monotonic tension SHB configuration [10].

As mentioned in the first paragraph of this section, techniques that allow for the study of cyclic loading are modified SHB, either in the form of torsion reverse loading Hopkinson bars [7,15], or tensile reverse loading split Hopkinson bars [10,16].

On one hand, the torsion bars present certain advantages, such the use of a simpler and more stable specimen geometry, which allows for easier strain measurements since the specimen does not suffer from barrelling, necking, or buckling. On the other hand, they don't produce the same strain rate in the two loading steps of the specimen and, although minimal, a gap of 1ms affects the study of the influence of adiabatic heating on reverse loading as it minimises the temperature rise within the specimen [17].

Therefore, for the scope of this study, the compression-tension (C-T) or tension-compression (T-C) bar systems are of more interest than torsion to this study.

Ogawa pioneered the design of reverse loading tensile Hopkinson bars proposing a very flexible system based on one-dimensional propagation of stress waves applicable to various kinds of one-dimensional deformation at high rates of strain, such as a dynamic tensile unloading and reloading, and dynamic tension-compression, compression-tension and tension-compression-tension tests [18].

More than just proposing the experimental set up, Ogawa's work presents an analytical development based on one-dimensional longitudinal pulse propagation in elastic bars to generate different multiple pulse loading configurations [16,18].

In the case of interest for this study, the compression-tension and tension-compression loadings are generated when the block mass (A3 in Figure 3) is infinite and the components are dimensioned so the incident and reflected waves impact the specimen consecutively without superposition.

The tension-compression reverse loading rig is shown in Figure 3 and a schematic depiction of the pulse generating section of the compression-tension is shown in Figure 4. The impact of a step shaped striker (A0) propagates an incident elastic wave along the input bar (A1) and dynamically deforms a specimen placed between the input and the output bars. By varying the

mass of the block (A3) and the relative dimensions between the anvil, striker and bars to synchronize the impact of the different waves reaching the specimen the specimen, different loading conditions can be achieved. When a striker hits the connecting end of the anvil and the input bar, the stress waves are generated both in the anvil and the input bar. The wave in the anvil is reflected at discontinuities and a series of stress pulses propagate down the input bar for the reasons above mentioned.

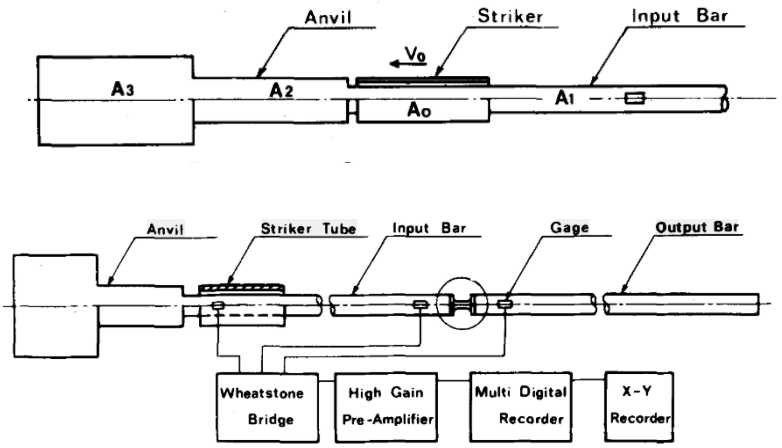

Figure 3. Tension-compression reverse loading split Hopkinson bar design by Ogawa[16,18]

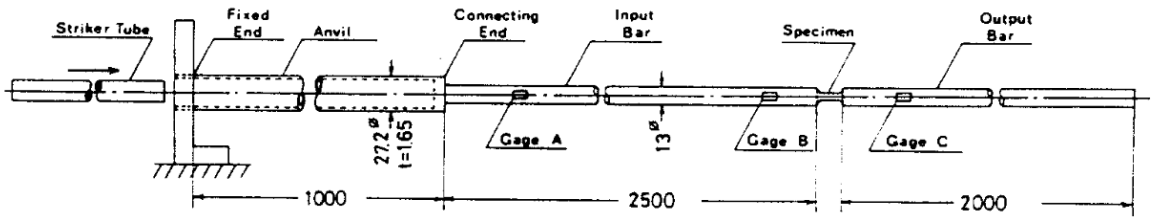

Figure 4. Compression-tension reverse loading split Hopkinson bar design presented by Ogawa[16,18]

Experimental set ups that follow Ogawa's design have as main limitations a non-constant strain rate between forward (tension) and load reversal (compression), the second being always lower, and they only allow to test the material under stress reversal, not strain reversal, since the stress pulses generated are symmetric. In addition, unwanted incident reflections can be problematic in the case of tests where the specimens do not break after the first reverse cycle. The magnitude of these reflected waves can be substantial and introduce an uncontrolled loading history in the specimen.

Nasser [19], and later Sathianathan [10] proposed an alternative type of C-T reverse loading SHB rig shown in Figure 5 and Figure 6. The baseline for both of their designs was the classical split Hopkinson pressure bar configuration, *Figure 1*, where the compressive pulse is generated by a projectile shot against the transfer flange of the input bar.

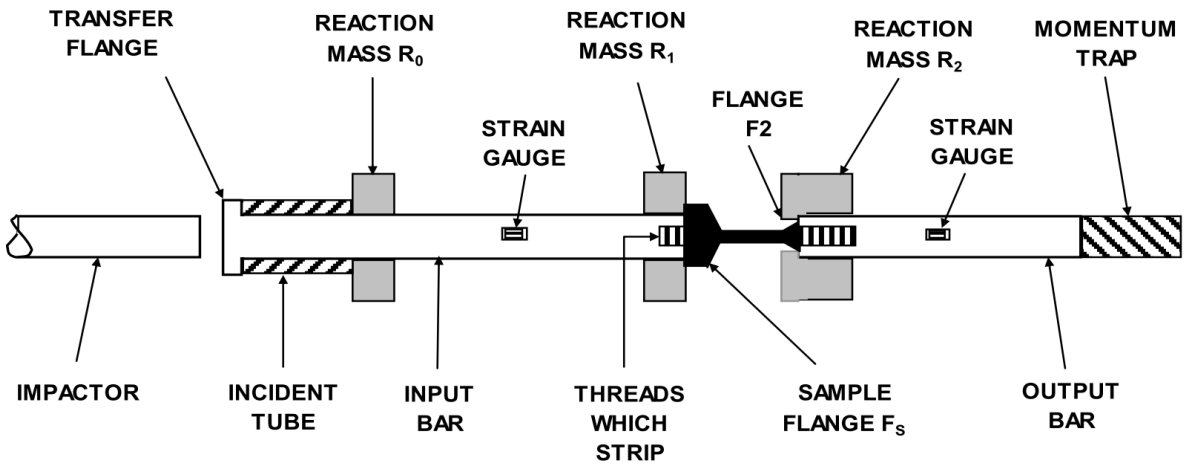

Figure 5. Compression-tension split Hopkinson bar proposed by Nasser [19]

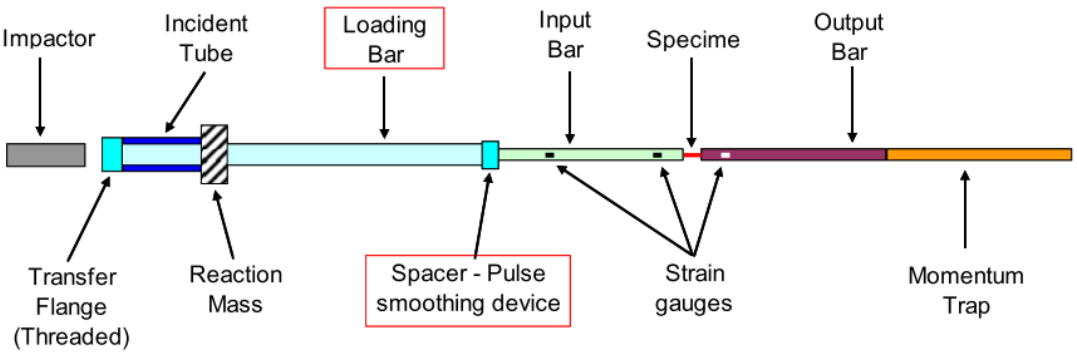

Figure 6. C-T RL SHB design by Sathianathan[10]

In order to generate the tension part of the compression-tension loop, a reaction mass is added, and the input bar is substituted with a set containing: a transfer flange, an incident tube and an input bar, all screwed together. The tension pulse is generated when the transfer flange impacts the incident tube, which hits the reaction mass. Since the reaction mass has a mass of orders of magnitude bigger than the incident tube it acts as an ideal infinite mass, and the compression pulse reflects as a tension pulse in the incident tube. The tensile pulse is transmitted to the transfer-flange-input-bar-specimen-output-bar set, loading the specimen in tension. Dimensioning is key in order to synchronise the compression and tension pulses and avoid the interference of other parasite reflections. The space-time diagram or Lagrangian diagram on Figure 7 illustrates the wave reflections described on the above paragraph.

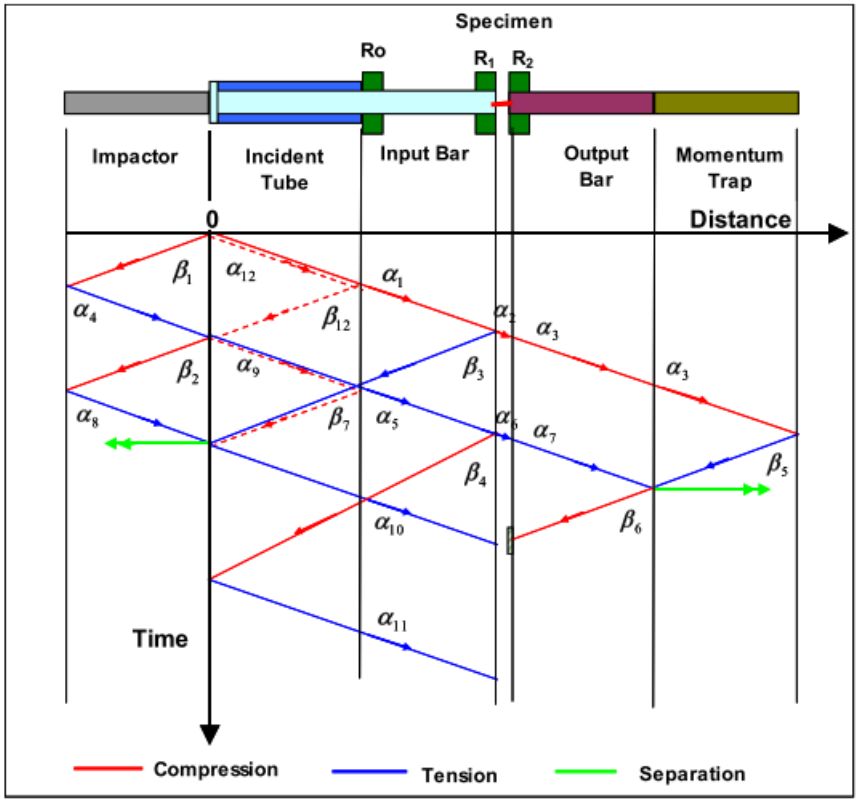

Figure 7 Lagrangian diagram of the C-T reverse loading designed by S.Sathianathan [10]

Finally, since reverse loading tests are usually realised at low or moderate strain rates and the specimens do not break after the first loading cycle, a momentum trap is needed to avoid the reflected waves from the output bar end from reaching back to the specimen. Therefore, the positioning of the momentum trap of matched impedance with the output bar is also crucial.

The differences between Nasser's [19] and Sathianathan's [10] designs are the presence of two extra reaction masses on the threaded ends of the specimen in the Nasser's rig that attempt to avoid the reloading of the specimen when the tensile pulse is reflected in the output bar. These reaction masses are designed so they generate a large reflected pulse going into the threads of the specimen, which are sheared off without the specimen being reloaded. In Sathianathan's design, these masses are removed, and a spacer that acts as pulse shaper is added to improve the wave dispersion.

For the case of T-C, Sathianathan proposed a new design for a T-C reverse loading SHB Figure 9 based on the monotonic tensile SHB Figure 8. Tensile SHB by Gerlach *[20]*, and very similar to Ogawa's [16], where a momentum bar and a mass were added to generate a compressive reflected wave that allowed the loading of the specimen in tension-compression succession in Figure 3.

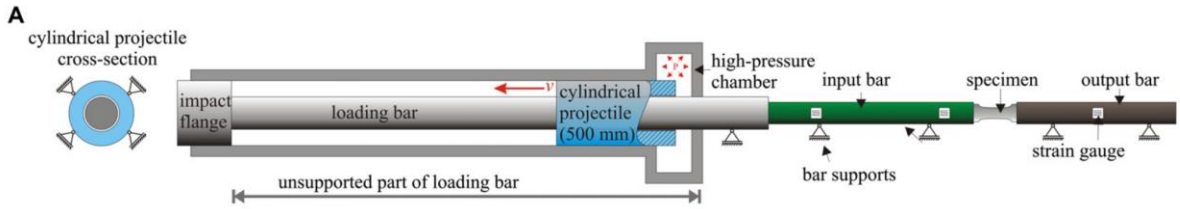

Figure 8. Tensile SHB by Gerlach [20]

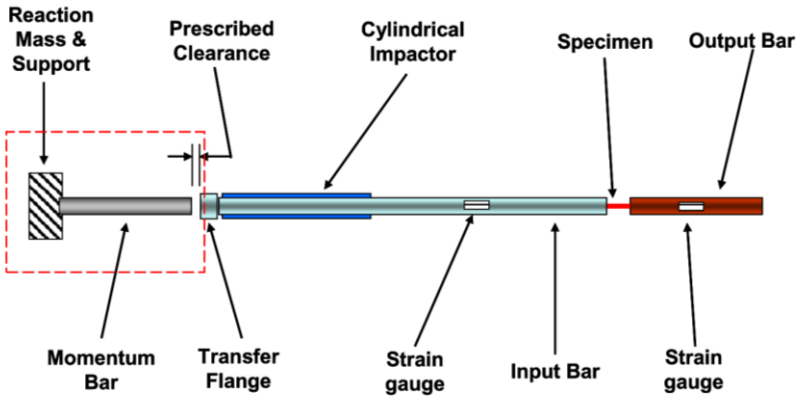

Figure 9. T-C RL SHB design by Sathianathan[10]

The general functioning principle of the technique proposed is similar to the C-T SHB: the tensile pulse is generated by the impact of the hollow impactor on the transfer flange, which

causes the flange to impact with the momentum trap, generating a compressive pulse back towards the specimen, loading it consecutively in tension-compression.

The described currently available designs, however, present a series of problems that limit their effectiveness and practical usage:

- They tend to suffer from many issues in achieving dynamic equilibrium.
- Their momentum trapping systems are not sufficient, making the control of the total deformation of the specimen very difficult due to reflections.
- They are only effective reversing substantially high strains.
- They only allow to execute stress recovery tests, where the specimen is strained and recovers back to 0 with almost no negative, or reverse, strain.

Therefore, there is not only room for, but arguably a need for improvements in experimental capabilities for reverse loading at high strain-rates.

2.2 Bauschinger Effect

Having covered the currently available experimental techniques for reverse loading, the next question is how this type of loading may affect the material behaviour. It is well known that the stress-strain response of metals subjected to reverse loading does not comply with the ideal plastic behaviour [6,21]. The aforementioned divergence is named after J. Bauschinger [22] who, in 1881, firstly observed that the stress-strain relation in mild steel was affected it's plastic deformation history. Bauschinger defined the effect as a function of the direction of initial pre-strain and of the resultant plastic deformation inflicted in the material.

The direction of the plastic deformation is understood as the principal axis of the strain tensor with respect to a fixed coordinate system and the pre-strain is the initial strain achieved during the first (forward) load, Figure 10a. When the direction of the pre-strain is coincident with the loading direction, the applied stress is referred to as forward stress and the yield strength increases with the plastic flow. If, conversely, the load direction is opposite to the pre-strain, the applied stress is named backward stress and the yield strength is reduced, Figure 8b.

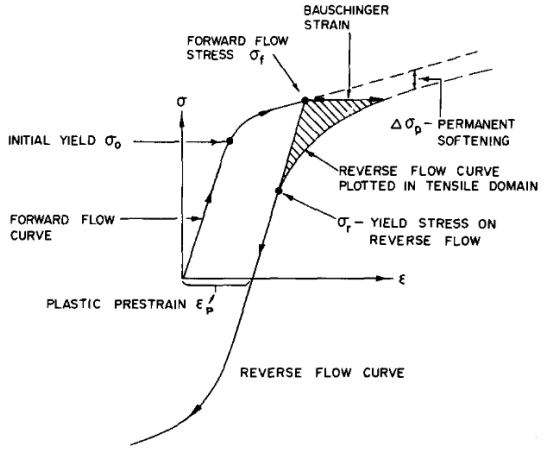

Figure 10a. Schematic representation of the uniaxial stress-strain behaviour during reverse loading in metals [23]

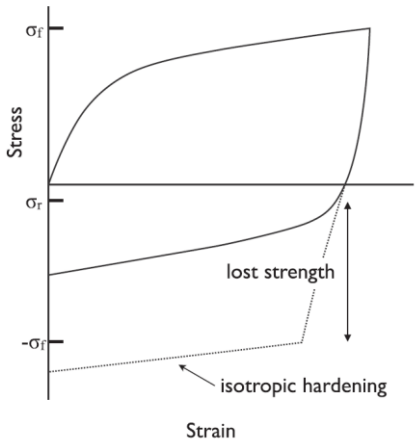

Figure 8b. Stress vs strain depicting the generalised effects of B.E.[24]

To quantify this effect multiple possible definitions have been proposed over the years. However, the most widely used parameters in literature are those from A. Muir [25] :

- Bauschinger strain (β): total strain obtained during the full cycle of load reversal.
- Plastic prestrain (εT): Plastic strain achieved in the forward load before reversal.
- Bauschinger strain parameter defined by $\beta_\varepsilon = \frac{\beta}{\varepsilon T}$
- Bauschinger stress parameter: $\beta_\sigma = \frac{\Delta\sigma}{\sigma_P}$

Where $\Delta\sigma = \sigma_P + \sigma_R$. σ_P is the maximum pre-stress in the forward load, and σ_R the yield stress in the backwards or reverse load.

- Bauschinger energy (Es), defined as "the quantity of energy saved in achieving a certain amount of deformation in reverse loading, as compared with the energy which would have been required to achieve the same increment of deformation in the absence of a B.E." by A.Muir in [25]. The energy exerted during the reverse load is defined as E_r, the expended in the prestrain as E_p. The ratio between these, $\beta_E = \frac{E_s}{E_p}$, may be taken as a measure of the Bauschinger effect as it reflects the stress and strain relationship as well as the rapid work hardening during reverse loading.

Figure 11 shows the graphic depiction of the B.E. parameters proposed by Muir in [25]:

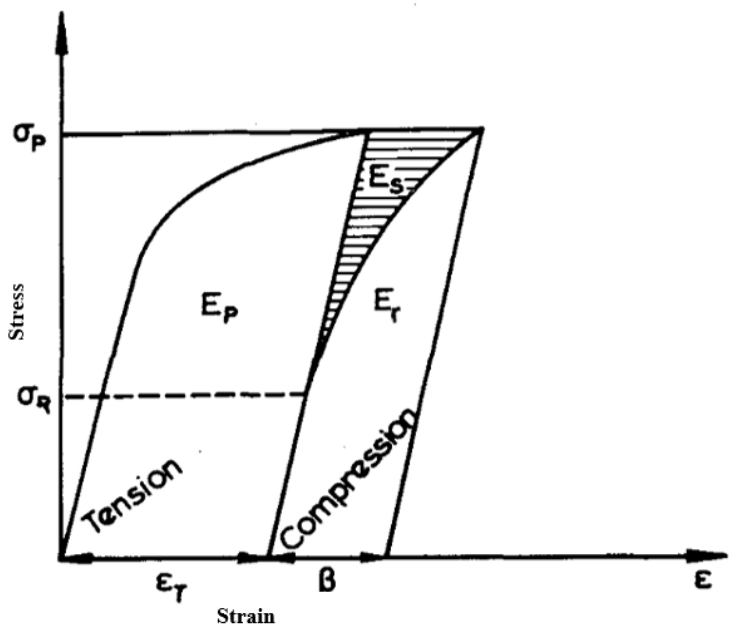

Figure 11. Graphic depiction of the B.E. parameters proposed by Muir [25]

Having defined the basic characteristics of B.E. and the most widely used definitions to quantify it, it is still not possible to identify a universally accepted theory on the causes behind

it. It is therefore necessary to carry out a thorough review of the theories that try to explain this directionality of strain hardening in metals.

The common ground shared by all of these theories is the presence of internal stresses [23], generated during the prestress or first loading of the material. These stresses are thought to interact with the plastic deformation mechanisms of the material [24], reducing the amount of plastic flow in the direction of the pre-straining but not in the reverse direction, giving as a result an asymmetric strain-stress response of the material when subjected to cyclic loads.

Thus, the study of B.E. is tied to the understanding of the predominant deformation mechanisms in the material as well as the work hardening theories and models applicable to the case of complex loading paths in metals.

Depending on the approach taken, theories can be classified as either macroscopic or microscopic in scale.

- ***Macro-scale theories***

Macroscopic scale approaches use continuum mechanics theories of plasticity to explain the causes of the Bauschinger effect. Both the initial studies on reverse loading [23,25] and more modern phenomenological work hardening theories use this approach [9].

The first observations on the B.E. [22] only detected the lowering of the yield stress as part of the strain hardening directionality, overlooking the changes to the stress-strain curve before the reverse yield of the material. However, it is now known that this directional dependency affects the entire stress-strain curve after pre-loading and is more complex than originally believed [3]

The first model created with the aim to explain the reverse loading behaviour of metals was the work of Heyn [1]. In Heyn's theory, the material is modelled as a conjunction of small volumes,

each with ideal stress-strain curves and different elastic limits giving as a result the generation of non-uniform internal stresses. Masing [26–28] applied Heyn's theory to reverse loading torsion testing. His results showed good fitting with Heyn's model for experiments with up to 0.5-1% strains before reversal. However, Heyn's approach failed to successfully represent the stress-strain curve in reverse loading at higher strains.

Subsequent work by Hencky [29], was based on the idea that the residual stresses resulting from unequal distributions of plastic flow between individual crystals was the main cause behind the Bauschinger effect [26]. This was based on the premise that, inside the polycrystalline aggregate that conforms the material, there cohabit various grains with different respective orientations. Thus, some grains would present an orientation that favoured the plastic flow in the direction of loading, whilst others would disfavour it. Therefore, materials showing asymmetry on the plastic flow during reverse loading presented an oriented texture or grain morphology.

However, the findings made by Gough, Wright and Hanson [30], discovering the presence of B.E. in single crystals of aluminium, and by Sachs and Shoji in 1927 [31], detecting the effect in brass single crystals, disproved the main theoretical school of thought at the time, which claimed that the principal cause of B.E. were the strain discontinuities at grain boundaries [1]. Several works were carried out to better understand the contribution of the grain boundaries effect, studying the B.E. in almost all crystalline metals [1], and determining that coarsely grained polycrystals and single crystal metals present the same magnitude of B.E.

From this point, grain boundary effects have been treated as a contributing factor but not the main cause of B.E., and thus research on B.E. has shifted towards new approaches.

Zener built a theory around the findings of B.E. in single crystals revoking the concept of residual stresses between grains, stating instead that "the deformation inside any one grain is

not uniform or homogeneous" [32]. He attributed the effect in single crystals to residual shear stresses between slip bands and the material adjacent to the bands [5].

Overall, efforts to explain the roots and mechanisms of Bauschinger effect through elastic-plastic continuum theories have proven partially effective, and only applied to materials where a significant volume fraction of second-phase particles is existent. Thus, "only composites, or smaller-scale alloys with large volume fractions such as dispersion-hardened aluminium are likely to have Bauschinger behaviour dominated by continuum-scale elasto-plasticity" [33]. Even though continuum mechanics-based theories cannot satisfactorily explain the causes and the physical principles behind B.E., from the engineering point of view, macroscopic models are extremely powerful to predict the material response under reverse loading conditions, and therefore are widely used in the industry.

- ***Micro-scale theories***

The theories that take a microstructural approach attribute the presence of an inhomogeneous plastic flow during reverse loading to internal stresses [9]. Depending on their nature, these internal stresses can be classified as short and long-range stresses [34]. The first are function of the dislocation arrangement and micro-scale barrier spacing (precipitates, inclusions, interstitials) and don't involve necessarily the presence of substantial internal stresses (Orowan-loop type mechanism) [34,35], while the latter are a function of the overall incompatibility between the indeformable inclusions dislocation heterogeneities present on the material and their surrounding matrix, and do imply the presence of internal stresses [34,36,37].

Two different groups of micro theories on the causes and origins can be distinguished: the first explain the existence of Bauschinger effect through the effects associated with dislocation pile-

ups and the second through the directionality of the driving force for dislocation motion during pre-straining.

Long-range internal stress (LRIS), or back stress, theories

Long-range internal stresses (LRIS) are commonly referred in literature as “back stresses” and are one of the main mechanisms that give rise to work hardening in metals. Numerous theories [38–41] explain the presence of B.E. due to the partial instability of the deformed state of the material, which results in the presence of long-range stress fields after plastic deformation on the initial, or forward, load. These long-range stresses are believed to exist as a consequence of crystal imperfections, such as the presence of inclusions or precipitates, that act as barriers for the slip or dislocation motion. The back stresses present directionality, opposing the further plastic deformation on the forward flow on one hand and, on the other hand, assisting the reverse motion of dislocations during the backwards plastic deformation and lowering the reverse yield stress.

However, the existence of long range internal stress fields in the deformed material is a debated topic [34]. Experiments in single crystal metals [28,42,43,43,44] show findings of significant B.E. already from the first cycle in aluminium and copper single crystal metals, when no cellular substructure is expected to have developed, suggesting that the Bauschinger effect is largely independent of such pronounced heterogeneities as cells or subgrains. Since LRIS are related to such heterogeneities, the direct relation between the aforementioned LRIS and B.E. is challenged. The fact that no significant elastic back stresses are required to produce large work softening during reverse loading [1,25,34], are the main arguments against back stress-based explanations of B.E.

Short-range internal stress, or dislocation motion, theories

The first to propose an alternative mechanism to explain the causes behind B.E. are Orowan and Canal [35]. They developed the first single dislocation model, where the anisotropy in the resistance to dislocation motion is the main cause of B.E. This anisotropy is introduced during pre-straining, so that, after a certain amount of pre-strain, it is easier to move a dislocation in the opposite direction to the preload rather than continue to move it in the same one due to the local, short range backstress generated on the prestrain (Orowan loop dislocation mechanism). Figure 12 illustrates this mechanism.

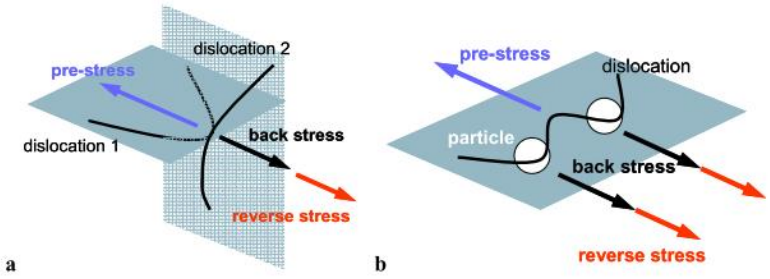

Figure 12. Schematic diagram of the a) dislocation-dislocation and b) dislocation-particle interactions in a material subjected to reverse loading [24]

The work of Abel and Muir [25], Kassner [34], Mott [39], Hirsch [45], Thakur et al [40], among others, followed the concept behind single dislocation theory to develop more complex models. These theories are based on the creation of mobile dislocations during the initial plastic deformation that adopt directionality during pre-strain and give directionality to the dislocation motion. The work of Muir et al. [25] showed that the dislocation looping mechanism described by Orowan [35] can produce significant Bauschinger effects for small volume fractions of closely-spaced particles.

Building on this idea, more recently, multi-dislocation models have also been developed [46–48]. These models consider the complex interactions between dislocation arrays during the straining of the material.

Combined Long- and Short-range internal stress theories

Although a big part of the theories on B.E. are based either on long- or short-range internal stresses, several models are based on the combined action of both as the cause of B.E., where both back stresses and dislocation motion contribute to the strength differential effects on work hardening on metals during cyclic loading. Gedeon's work [1] proves the presence of both short- and long-range internal stresses in copper and iron specimens by doing an extensive study on the effect of temperature and straining on the B.E..

The most sophisticated models currently developed in this area are the work of Mughrabi and Predersen [49]. Their "composite" models consider the combined effect of relatively high magnitude long- and short-range stresses generated by heterogeneous dislocation substructures [50].

From this section of the literature review, it is clear that there is still much to learn about the driving mechanisms behind the Bauschinger effect and reverse loading response of metallic materials in general. However, in the case of Ti-6Al-4V, in particular, there are added challenges to do with the complex deformation mechanisms it presents, such as twinning, which are discussed in the following section. The work proposed in this project may help to answer some of these questions by providing new high strain-rate deformation and reverse loading data against which to evaluate these theories and the assumptions they are based on.

2.3 Deformation mechanisms in Ti-6Al-4V

The mechanical behaviour of a material is undoubtedly linked to its microstructure [51]. To study the stress-strain behaviour Ti-6Al-4V it is indispensable to understand the particularities of the material from the microstructural point of view, even if the objective is to characterise or model it at a macroscopic scale using continuum mechanics principles.

Ti64 (Ti-6Al-4V) is a classical α + β titanium alloy, with a low volume fraction (5–10 %) of the high temperature cubic body centred phase (β phase), and a remaining volume fraction of the low temperature hexagonal close packed (α phase) allotropic form of titanium [52].

This complex microstructure affects the elastic and plastic deformation of Ti-6Al-4V. Titanium presents two main deformation mechanisms: dislocation gliding, and crystal twinning Figure 13.

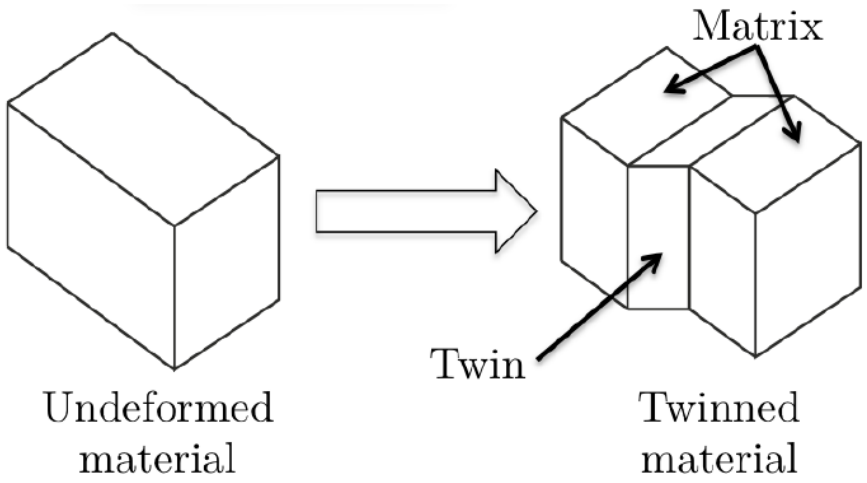

Figure 13. Schematic of deformation twinning on a macroscale causing a shape change [53]

With regard to dislocation slip mechanisms in Ti-6Al-4V, which dominate deformation behaviour at low strain rates [51,53,54] , since the HCP-α is the dominant phase, it is broadly accepted that the global material response can be assimilated to the response of the α phase of titanium [7, 33], occurring mainly along the prismatic, basal and pyramidal planes [53], shown in Figure 14.

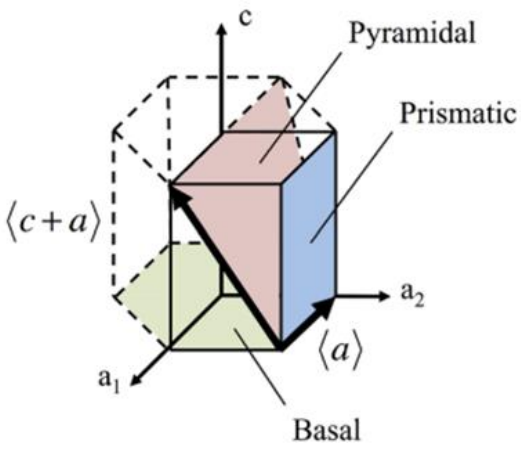

Figure 14. Main active slip systems in hcp titanium [51]

On the other hand, twinning, which occurs the higher strain-rate response, exhibits significantly different behaviour in Ti-6Al-4V and is not as well understood as it is in pure titanium (Ti CP) [55–57] There is a lack of consensus around the relevance of twinning in Ti-6Al-4V, with several works [58–60], pointing at the effects of aluminium as a twinning inhibitor, whereas [51–53,61] show a high strain rate deformation dominated by twinning mechanisms. Furthermore, research on deformation twinning in titanium alloys is scarce in general, and there is especially a lack of research into deformation twinning at high strain rates and in alloys containing Al, both at high strain rates and low temperatures [53].

However, it is widely accepted that Ti-6Al-4V presents a pronounced tension-compression asymmetry associated with the activation of twinning. This twinning is easily activated along the c axis during compression, which causes the strength differential effect (SD).

Most previous studies have focused on capturing these features (SD, anisotropy) and validation has been essentially based on the assessment of true stress-true strain curve predictions of monotonic tests. However, these same features will have a much greater impact on the material response under reverse loading, making it a critical load case to study and providing better data for model validation.

In addition to twinning, the study of the mechanical response of Ti-6Al-4V under reverse loading may require the consideration of detwinning as another potential deformation mechanism and contribute as an additional factor [62]. No studies on detwinning during cyclic loading in Ti-6Al-4V have been found but, in their absence, similar behaviour to that showed by titanium CP (HCP) [62,63] can be expected, which suggests the presence of detwinning during cyclic loading.

If this is the case, it will be crucial to take this effect into consideration. Sinha [64] concluded that detwinning due to load reversal plays an important role in the microstructure evolution during cyclic deformation, affecting the strain hardening in the material and acting as a back stress relieving factor due to the release of dislocations and stresses formed at twin boundaries.

2.4 Constitutive modelling

Even though the physical deformation mechanisms and Bauschinger effect in Ti-6Al-4V have complex micromechanical roots, more phenomenological continuum mechanics models can be very useful tools to describe the material response for most practical applications. At the same

time, there exist several arguments against the adoption of micromechanical based models. For one, these will often be too time- and resource-intensive for larger scale applications. In addition, the verification of semi-phenomenological models like these, which are based on microstructural phenomena such as dislocation cell structures, slip band evolution, and including dislocation bow-out models, presents a very high difficulty due to the inconsistency of experimental results at macroscopic scales and the lack of a universal agreement on the causes of B.E. [1]. Overall, neither the computational tools nor the current knowledge on the micromechanics behind work hardening and Bauschinger effect are ready yet to allow the use of micromechanical modelling for practical industrial applications.

Therefore, the modelling aspect of the proposed study will be focused on constitutive models for Ti-6Al-4V at the continuum scale. However, macroscopic phenomenological models for Ti-6Al-4V under reverse loading introduce technical challenges by themselves.

The complex deformation mechanisms in Ti-6Al-4V and loading paths caused by cyclic loading, in addition to strain rates effects when considering high-rate load reversal, result in a series of specific requirements for a constitutive model to accurately represent Bauschinger effect in titanium alloys [65]. Many currently available models in the literature take into consideration certain of these individual effects, but very few encompass all of the requirements for the description of B.E. in reverse loading at different strain rates.

Empirical phenomenological models are commonly used throughout the aerospace industry due to their ease of implementation and numerical robustness when validating design modifications and new mechanical material test data. This study will include some of the most well-established models, already included in commercial software packages, such as LS-Dyna and Abaqus, in order to show the extent of their capabilities for the case study of this work.

The description of the following models and their key equations has been extracted from the Ls-dyna theory manuals [66] and the respective indicated references:

- ***Initial elastic response***

The initial elastic response of Ti-6Al-4V can be described by an isotropic hypo-elastic material law. As its name implies it only includes the elastic behaviour of the material and serves as the foundation for the different plastic models described in the following points.

The co-rotational rate of the deviatoric Cauchy stress tensor (${s_{ij}}^{\nabla^{n+1/2}}$) and pressure (p^{n+1}) are computed as:

$${s_{ij}}^{\nabla^{n+1/2}} = 2G\dot{\varepsilon}_{ij}{}^{\prime\ n+1/2\#} \qquad (1)$$

$$p^{n+1} = -KlnV^{n+1} \qquad (2)$$

where G and K are the elastic shear and bulk moduli, respectively, and V is the relative volume [66].

- ***Plastic kinematic constitutive model***

Formulated by Krieg and Key [67], the implementation in LS-Dyna has the capability to represent either isotropic hardening , kinematic hardening, or a combination of both through the parameter β, which varies between 0 and 1 to represent respectively, kinematic or isotropic hardening.

The yield condition is defined by:

$$\phi = \frac{1}{2}\xi_{ij}\xi_{ij} - \frac{{\sigma_y}^2}{3} = 0 \qquad (3)$$

$$\text{where } \xi_{ij} = s_{ij} - \alpha_{ij}, \text{ and } \sigma_y = \sigma_0 + \beta E_p \varepsilon_{eff}^p \quad (4)$$

The co-rotational rate of the back stress, α_{ij}, which defines the kinematic hardening is expressed as:

$$\alpha_{ij}^{\nabla} = (1 - \beta)\frac{2}{3}E_p \dot{\varepsilon}_{ij}^p \text{ and } \alpha_{ij}^{n+1} = \alpha_{ij}^n + \left(\alpha_{ij}^{\nabla^{n+\frac{1}{2}}} + \alpha_{ik}^n \Omega_{kj}^{n+\frac{1}{2}} + \alpha_{jk}^n \Omega_{ki}^{n+\frac{1}{2}}\right)\Delta t^{n+1/2} \quad (5)$$

Strain rate is accounted for using the Cowper-Symonds [Jones 1983] model which scales the yield stress by a strain rate dependent factor

$$\sigma_y^{\nabla} = \left[1 + \left(\frac{\dot{\varepsilon}}{C}\right)^{\frac{1}{p}}\right](\sigma_0 + \beta E_p \dot{\varepsilon}_{eff}^p)\,; \quad (6)$$

where p and C are user defined input constants and $\dot{\varepsilon}$ is the strain rate defined as:

$$\dot{\varepsilon} = \sqrt{\dot{\varepsilon}_{ij}\dot{\varepsilon}_{ij}} \quad (7)$$

The isotropic expansion of the yield surface is dominated by the term $\sigma_0 + \beta E_p \dot{\varepsilon}_{eff}^p$ in equation (6) where E_p is the plastic hardening modulus $E_p = \frac{E_t E}{E - E_t}$ and $\dot{\varepsilon}_{eff}^p$ the effective plastic strain:

$$\dot{\varepsilon}_{eff}^p = \int_0^t \left(\frac{2}{3}\dot{\varepsilon}_{ij}^p \dot{\varepsilon}_{ij}^p\right)^{1/2} dt \quad (8)$$

The plastic strain rate is the difference between the total and elastic strain rates:

$$\dot{\varepsilon}_{ij}^p = \dot{\varepsilon}_{ij} - \dot{\varepsilon}_{ij}^e \quad (9)$$

The deviatoric stresses, s_{ij}, are updated following linear elastic behaviour, and a stress return algorithm, such as Newton-Raphson, is used to return them onto the yield surface during plastic deformation.

- ***Johnson Cook constitutive model***

The Johnson-Cook constitutive model [68,69] is a phenomenological model that combines strain hardening, strain-rate effects, and thermal softening in a multiplicative manner. The first bracketed term in equation (9) represents the strain hardening of the yield stress, the next term models the increase in the yield stress at elevated strain rates, and the final bracketed term is a softening of the yield stress due to local thermal effects.

$$\sigma_y = (A + B\left(\varepsilon_{eff}^{p}\right)^{m})(1 + cln\dot{\varepsilon})(1 - T^{*m}) \qquad (10)$$

A, B, C, n and *m* are user defined input constants,ε_{eff}^{p} is the effective plastic strain, and $\dot{\varepsilon} = \frac{\dot{\varepsilon}_{eff}^{p}}{\dot{\varepsilon}_0}$ is the strain rate, where $\dot{\varepsilon}_0$ is strain rate used to determine the initial yield stress, A, and hardening parameters, *B* and n. T^* is the homologous temperature defined as: $T^* = \frac{T - T_{room}}{T_{melt} - T_{room}}$

Additionally, the model requires the thermal parameters of the material C_p, T_{melt}. Typically, the shear modulus is input along with an Equation-of-State (EOS) used to define pressure versus volume strain response; for low pressures, the EOS is assumed to be defined by the elastic bulk modulus.

In [70] G. Johnson and W. Cook expanded on their model adding a cumulative-damage model for fracture:

$$\varepsilon^F = \left(D_1 + D_2 exp\left[D_3 \frac{P}{\sigma_{eff}}\right]\right)(1 + D_4 ln\dot{\varepsilon})(1 + D_5 T_H) \qquad (11)$$

With $D = \sum \frac{\Delta\varepsilon_{eff}^{p}}{\varepsilon^F}$ where failure occurs at D =1; σ_{eff} is the effective stress; and P is the mean stress.

The expression that defines the damage is similar in form to the yield strength model with three terms combined in a multiplicative manner to include the effects of stress triaxiality, strain rate,

and local heating, respectively. This portion of the Johnson-Cook constitutive model requires an additional five material model parameters (D_1,D_2,D_3,D_4,D_5),defined as fracture constants. D_4 is the strain rate constant defined at $T^* = 0$, D_1,D_2 and D_3 constants are related to the pressure-stress ratio, and D_5 to the temperature.

- ***Bammann constitutive model***

This model by D. Bammann [71], was developed from the base assumption that the inelastic flow depends on the value of the stress and the current value of two internal variables (tensor and scalar), which represent the dislocation state at any continuum point.

Assuming linear elasticity:

$$\sigma^0 = \lambda\, tr(D^e)1 + 2\mu D^e \qquad (12)$$

Where the Cauchy stress, σ, relates to the concepts included in the field of crystal plasticity of elastic spin (W^e) and elastic stretching (D^e) through the expressions:

$$\sigma^0 = \dot{\sigma} - W^e\sigma + \sigma W^e \qquad (13)$$

The elastic stretching being a representation of the stretch of material fibre in a given direction, while the elastic spin represents the angular velocity of the fibre in a material point. The formulation of the aforementioned concepts belonging to crystal plasticity modelling are further defined and formulated in the reference [72].

The implementation of the model in LS-Dyna includes temperature and rate dependent plasticity, as well as temperature change during deformation. In the absence of a coupled thermo-mechanical finite element code, it assumes adiabatic temperature change and follows the empirical assumption that 90-95% of the plastic work is dissipated as heat.

Hence, $\dot{T} = \frac{0.9}{\rho C_v}(\sigma\, D^p)$, where ρ is the density of the material, C_v the specific heat, and D^p the plastic stretching component formulated in reference [72].

The model also includes the consideration of damage evolution in the material defined by:

$$\phi = \beta\left[\frac{1}{(1-\phi)^N} - (1-\phi)\right]^{|D^p|} \qquad (14)$$

where $\beta = \sinh\left[\frac{2(2N-1)p}{(2N-1)\overline{\sigma}}\right]$, p is pressure, and $\overline{\sigma}$ the effective stress.

- ***Johnson Cook tabulated constitutive model***

This material model is based on the previously described Johnson Cook model but with the possibility of general tabulated input parameters. It consists of an elastic-plastic constitutive law with arbitrary stress versus strain curves and arbitrary strain-rate dependency. It includes plastic failure strain as function of triaxiality, strain rate, temperature, and element size.

The research conducted by the U.S. Federal Aviation Administration in [73] offers an extensive development and validation of a set of material constants using the tabulated input method of this model in LS-DYNA, with consideration given to strain rate and temperature, specifically for a rolled 1/2-inch Ti-6Al-4V sheet. The inputs generated in the report allow for the consideration of isothermal effects, strain rate dependency, including non-constant strain rates and high strain-rate sensitivity, and temperature effects. It also includes an effective failure surface model generated from experimental data. This implementation of the Johnson Tabulated model for Ti-6Al-4V offers a very detailed and potent tool compared to the other considered phenomenological models. Thanks to its extensive experimental calibration. As such, it will be utilised in the numerical simulations to investigate the performance of these models in predicting the response of the studied material to cyclic loading.

3. Experimental reverse loading of Ti-6Al-4V

In order to perform the experimental testing campaign in this study, comprised of a series of reverse loading experiments at quasi-static and high strain rates at room temperature, a number of challenges had to be addressed. The following sections describe the work done to obtain reliable test results for reverse loading on Ti-6Al-4V at quasi-static and high strain rates, including: specimen design in section 3.1; quasi-static experimental set-up and results in section 3.2; and, finally, the high-rate experimental set-up and results in section 3.3.

3.1 Specimen design

The first challenge to face is the development of a specimen geometry optimised for the various and complex testing conditions of this study, including both tension and compression at different strain rates.

For this task, the specimen is designed, in broad terms, to perform well in the dynamic loading tests, aiming at guaranteeing the alignment of the specimen with the bars in the split Hopkinson bar systems to ensure uniaxial loading conditions and avoid any potential buckling or shearing. The baseline for the chosen design is the current in house designed specimen for monotonic tension split Hopkinson bar testing, Figure 15, its technical drawing is shown in Figure 16. Following the suggestions from Sathianathan [10], who performed an extensive study on the performance of tensile specimens in reverse loading and recommended using a shortened gage length, a modified tensile specimen with a shorter gauge section, from 8 mm to 3 mm, has been used to avoid buckling in compression.

Figure 15 Comparison between 3mm and 8mm gauge length specimens

The material for the specimens was obtained from Ti-6Al-4V cross rolled plates (TFH) supplied by Rolls-Royce Plc. Specimens were then machined with their axis oriented in the radial direction corresponding to the longest dimension of the plates. These specimens were specially made to the standard shown in Figure 16. The threads at the ends of the specimen facilitate the connection of the specimen to the apparatus. These threads were held with suitable fixtures on the quasi-static machine and screwed directly into the loading bars on the split-Hopkinson-bar systems.

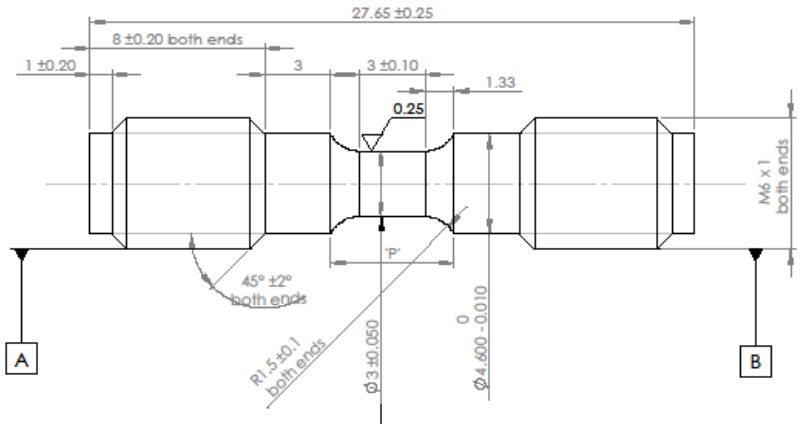

Figure 16 Final specimen design dimensions (mm)

3.1.1 DIC (Digital image correlation)

Another key aspect of the specimen design was the application of a suitable speckle pattern to allow for accurate strain field measurements through digital image correlation. Digital image correlation (DIC) is an optical measuring technique that allows for the determination of the full field coordinates of the surface of a test specimen [74]. In this work, its use is centred on the application of Virtual strain gages in the gage length area of the specimens using commercial software DIC packages.

To guarantee precise strain measurements using this technique, it is necessary to apply a good quality pattern in the specimens, using of an optimal camera set up and use the adequate software calibration and calculation parameters in accordance to the pattern characteristics.

- ***Pattern evaluation***

Technique

In all cases the pattern has been obtained applying white and black acrylic water-based paints with an airbrush. The experience obtained in the Oxford University IEL laboratory shows that the usage of this technique provides good results for titanium samples, obtaining a pattern applying with good contrast and a matte finish, allowing strain determinations during the testing even during the plastic deformation of the specimens.

- ***Pattern characteristics***

The main guidelines found in literature regarding the optimal pattern parameters for DIC [74,75] point at the importance of a pattern feature size over 3 pixels to avoid aliasing induced

error in the DIC [76]. A random, non-directional distribution such that different subregions of the pattern can be uniquely identified and a proportion between white background and black speckles around 25-40% for round specimens [74].

In order to assess if the pattern obtained complies with the desired parameters an analysis using ImageJ (Fiji) was carried out. To guarantee representative results, and account for the variability in the patterns obtained, a sample size of 10 images is included in the study. The images analysed have been taken with the same camera and lens as used for the quasi-static testing. The setup has been selected with the intention of maximising the detail acquired in the gage length of the specimens (telecentric lens, double light source to avoid shadows).

An IDS Ueye UI 3280-Cp-m-Gl Rev.2 camera (2/3" CMOS mono sensor) coupled with a Schneider-Kreuznach Telecentric Xenoplan 1:1 lens (bilateral telecentric lens, f stop 0.14 was used to obtain images with a resolution of 2456x2058 pixels.

Since the samples are meant to be tested at different strain rates, and therefore employing different cameras with their respective optical resolutions, it's necessary to conduct all the calculations scaling the proportion between the dimensions of the specimen and the pixels of the images to be able to acquire valid data independently to the camera used in the image capture. All results are presented in mm after scaling the proportion between pixels and dimensions of the specimen (298 pixels/mm).

From the pattern analysis, the following characteristics were determined:

Determining the feature size of a pattern is not an easy task [74]. The simplest method to determine it is by simple visual inspection [74]. Figure 17 shows the pattern in the gage length region of one of the specimens after converting the image to binary (white/black). The pattern obtained is well distributed along the surface of the specimen without any directionality or

order. By measuring the distance between speckles in the region where the pattern is finer, it can be implied that the pattern feature size is, for the most part, over the recommended 3 pixels.

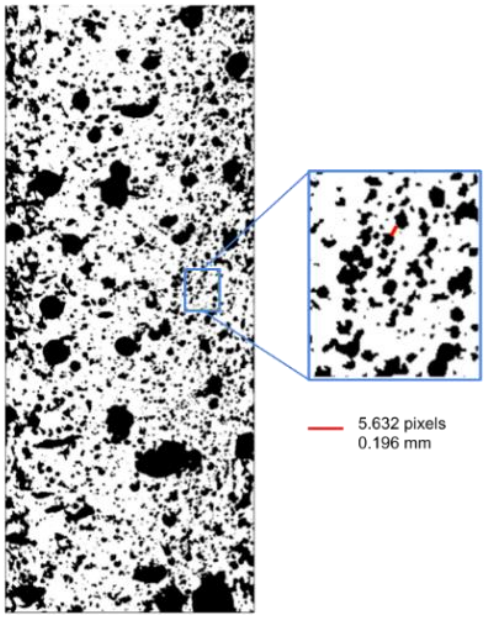

Figure 17 Pattern obtained in the ROI of a specimen; the detail shows the feature dimension scale.

The statistical study of the pattern along the 10 samples shows that the area covered by the speckles represents a 27% of the total surface of the specimens.

The pattern obtained presents a considerable variability as shown in Figure 18, the cumulative probability plot of the speckle size shows a wide spectrum of sizes. An approximate 80% of the total amount of speckles present an area under 50 $pixel^2$ ($5.6 \cdot 10^{-4}$ mm^2) of area.

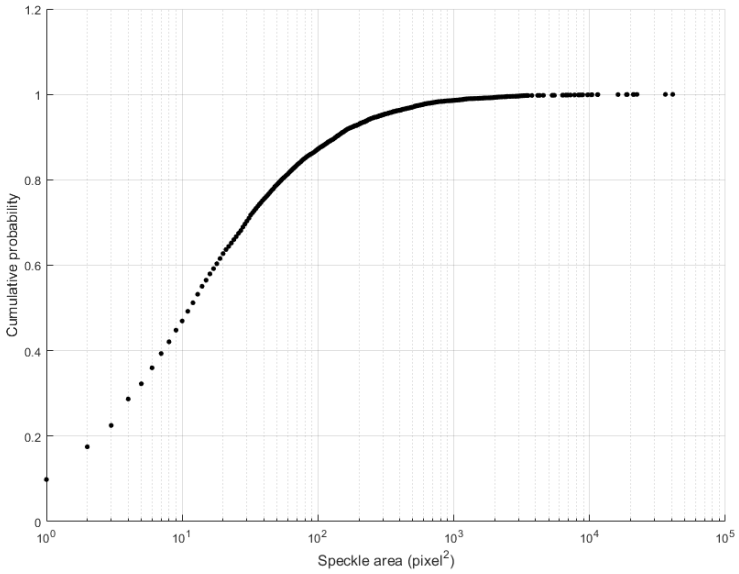

Figure 18 Cumulative plot of the speckled areas of the specimen

The obtained pattern complies with the recommendations and overall parameters seen in literature regarding DIC analysis, and therefore, as soon as the software parameters are calibrated accordingly, meaningful DIC determinations are expected.

- ***Image characteristics***

The images obtained with each of the used camera rig are studied independently since they present different resolution and field of view (FOV) influencing the DIC analysis.

QS

Figure 19 shows the Field of view (FOV) acquired by the camera and the region of interest (ROI) in the specimen. The images present a resolution of 1546x2152 pixels. The image scale

is set at 100 pixel/mm using the known gage length of the specimen and measuring it using ImageJ.

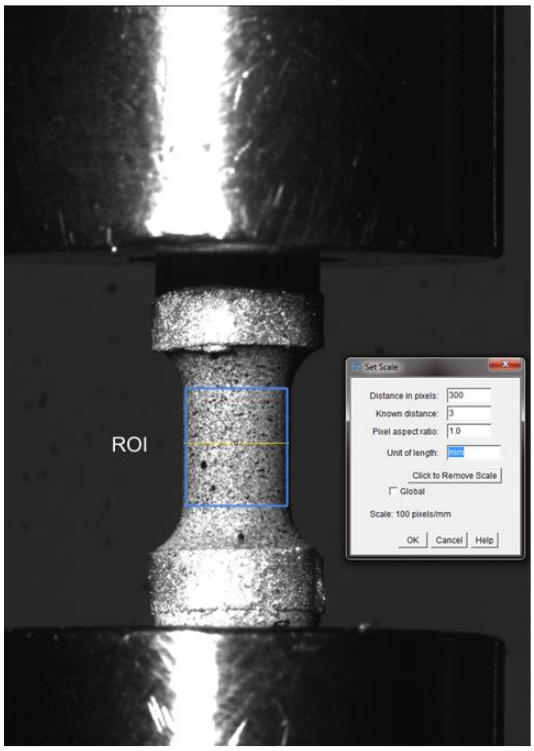

Figure 19 Field of view (FOV) acquired by the camera and the region of interest (ROI) in the specimen for the QS tests

HR

In case of the high strain rate tests the images are recorded at a frame rate of 600 kfps and an image resolution of 924x768 pixels using a Kirana high-speed camera from Specialised imaging. The image scale is 46.33 pixels/mm and Figure 20 shows the Field of view (FOV) acquired by the camera and the region of interest (ROI) in the specimen.

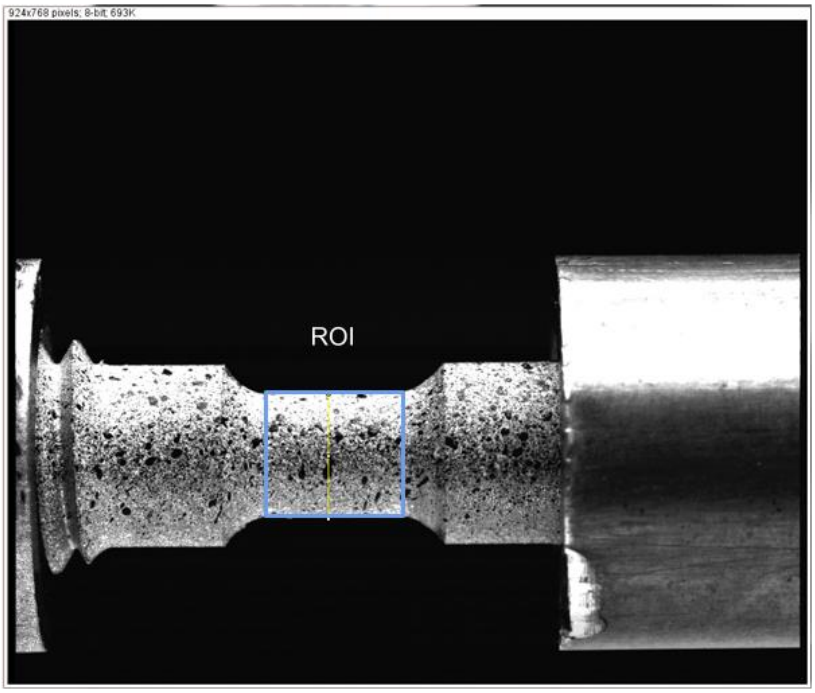

Figure 20 Field of view (FOV) acquired by the camera and the region of interest (ROI) in the specimen for the HR tests

- ***Software parameters:***

Virtual strain gauge

Once the pattern used for the DIC calculations is well characterised, we can calibrate the software accordingly in order to obtain meaningful results in the strain calculations.

The Table 1 summarizes the most important parameters in the virtual strain gage used for DIC analysis.

Table 1 Main values for the DIC analysis in the QS and HR experiments.

	Parameter	QS	HR
Image properties	Image scale (pixels/mm)	100	46.33
	Image resolution	1546x2152 pixels	924x768 pixels
Time series settings	Correlation mode	Correlative to first image	Correlative to first image
	Max displacement expected (pixels)	450	200
Displacement calculations settings	Subset size	31	33
	Step size	13	13
Calculation mode		Gaussian 6th order spline	Gaussian 6th order spline
Virtual strain gage characteristics	Strain formulation	Engineering strain	Engineering strain
	Length	2.8 mm	2.8 mm

3.2 Quasi static reverse loading

With a suitable specimen design and speckle pattern for DIC strain measurement in place, the experimental campaign can then begin in earnest. In the following sections, the work done to obtain an optimal test set-up is described in 3.2.1, and the obtained results for Ti64 under quasi-static reverse loading are presented in 3.2.2.

3.2.1 Quasi-static experimental setup

The quasi-static campaign was carried out using a Zwick/Roell Z050 screw-driven loading rig for quasi-static rate testing (controlled crosshead velocity) equipped with a 50 kN load cell and a laser extensometer Electronic Instrument Research LE-05 to acquire real-time strain

measurements, used for strain-based control of the crosshead. The laser extensometer measured the distance between the bottom edges of two pieces of retro- reflecting tape affixed to the sample. The extensometer was operated with an offset distance of 381 mm as specified by the manufacturer. The described rig is shown in Figure 21.

This setup allowed for great testing flexibility in the quasi-static loading regime. In this way, both compression-tension and tension-compression reverse loading tests, and multiple consecutive cycles were able to be carried out in the same setup without interruptions or set up changes.

Since the proposed testing method isn't affected by the loading direction, both compression-tension and tension-compression cycles are addressed indistinctly.

The tests were recorded in order to allow DIC strain determinations. An IDS Ueye UI 3280-Cp-m-Gl Rev.2 camera (2/3" CMOS mono sensor) coupled with a Schneider-Kreuznach Telecentric Xenoplan 1:1 lens (bilateral telecentric lens, f stop 0.14) were used to register images at a framerate of 1 image per second.

Figure 21 Images of the rig employed for the quasi-static reverse loading tests.

The main challenge faced for the chosen experimental setup was the displacement control for accurate strain reversal in the specimen. Since the stress-strain relationship of the material, the specimen length, and its cross-section are not constant, the experiments have to be done by controlling the crosshead displacement of the machine as a function of the specimen strain in real time. Real-time strain measurements were obtained using the described laser extensometer set-up. However, due to the issues above, slack in the fixture and machine, and settling times, which are particularly severe during the load the direction changes and can lead to stress relaxation effects, the extensometer readings needed to be calibrated against the real strain in the specimen gauge section [7,41]. Figure 22 shows the divergence in strain between the laser extensometer readings and the strain obtained by DIC:

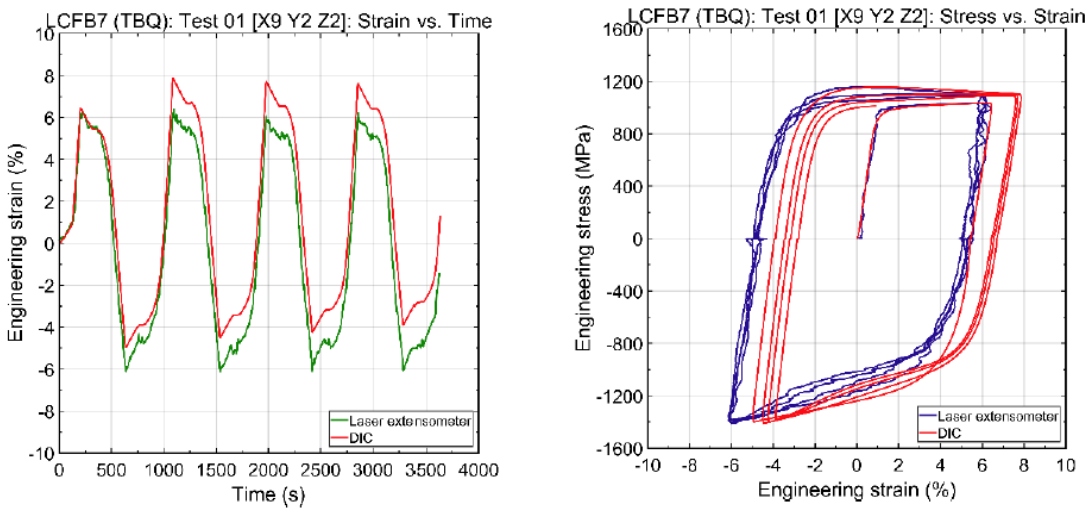

Figure 22 Comparison of laser-extensometer and DIC strains obtained

The relation between the extensometer readings and the real specimen strains is determined comparing the strains obtained through digital image correlation with the laser extensometer readings. Several tests at different strain to reversal have been effectuated, allowing the calibration curve shown in Figure 23 to be obtained:

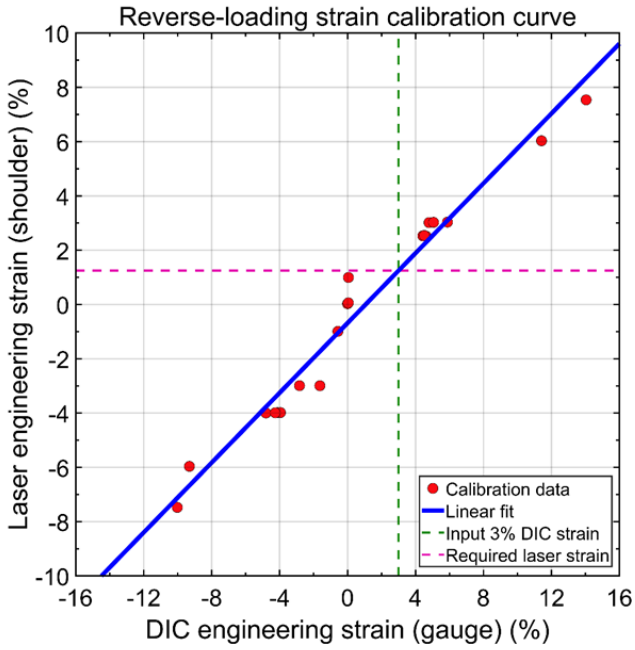

Figure 23 Calibration curve between laser extensometer strain readings and DIC obtained strains in the revere loading tests.

The obtained calibration curve allows the conversion of the extensometer readings into strains to control the crosshead displacement. In this way, corrected strain readings could be obtained in real time and the loads could be reversed at the desired strain values more accurately.

In addition, due to certain instability in the beginning of the first compression, a small compressive preload was introduced in the testing routine to allow the settling of the system and minimise the effects of the slack between the fixtures and the threads of the specimen.

Finally, in order to maximise the accuracy of the data acquired, the strains in the material were obtained from DIC calculations obtained following the procedure described in 3.1.1 and the forces registered by the load cell in the Zwick Z050 universal testing machine were synchronised in time with the DIC data to extract the stress-strain curves from the performed experiments.

3.2.2 Quasi-static reverse loading results

With an adequate, reliable methodology to perform strain controlled, quasi static reverse loading tests defined, both tension-compression and compression-tension tests were conducted as documented in the previous section. The objective is to obtain reliable stress-strain results useful for the analysis of the Bauschinger effect. Therefore, the tests aimed to reach maximum strains in each loading direction well past the yield point of the material, but low enough to avoid the introduction of issues as buckling or risking a premature failure of the specimen due to large deformations.

The graphs presented in this chapter serve as a representative sample of the data acquired by the experimental technique describe in the previous section.

- ***Tension-compression***

The tension-compression (T-C QS) tests were conducted at room temperature, with a crosshead velocity of v=0.003 mm/s and a target maximum strain of ±5.5%. The strain vs time and engineering stress vs time are shown Figure 24:

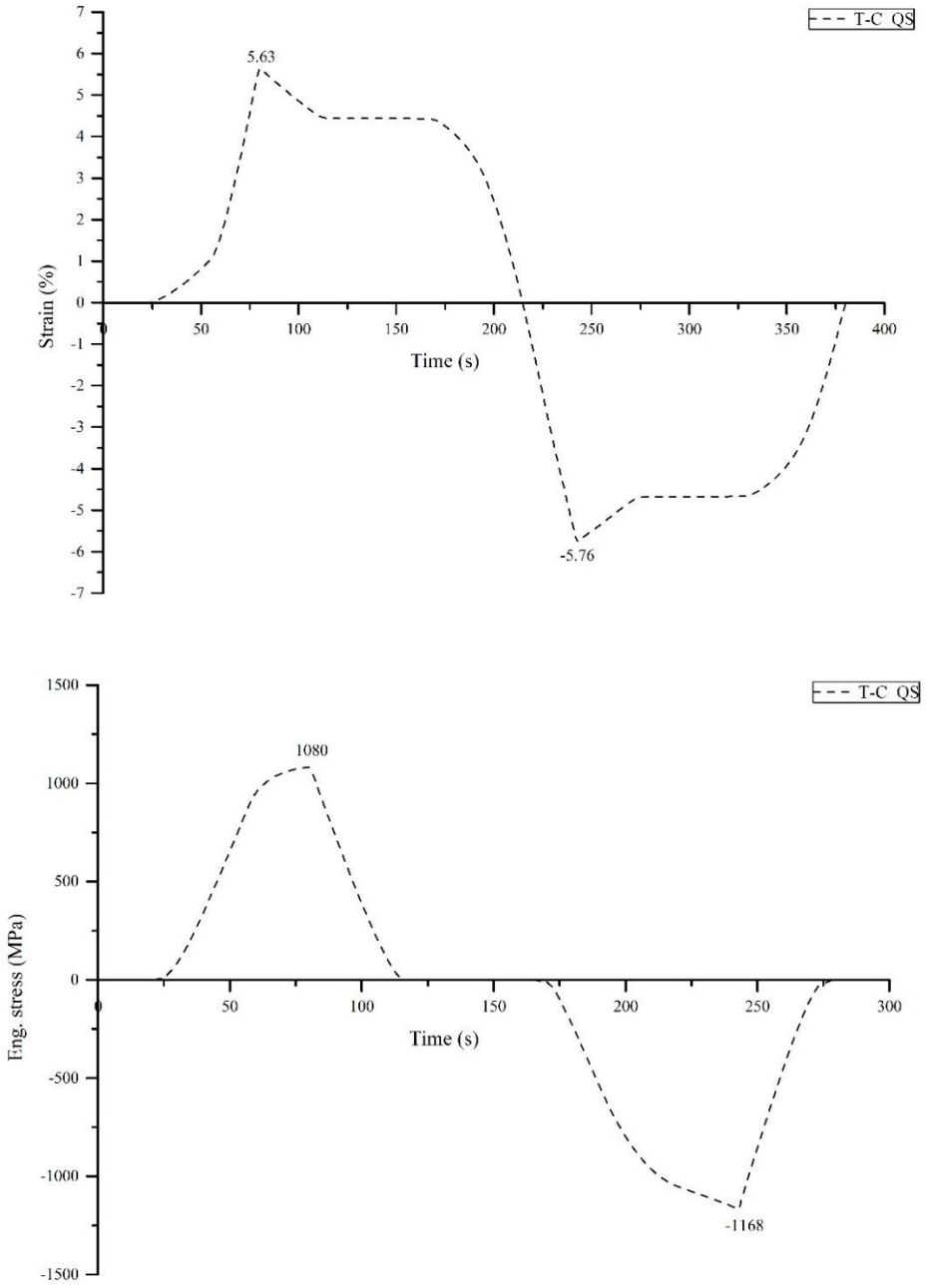

Figure 24 Compression-tension QS strain (%) and engineering stress vs time for 1 completed loading cycle.

The strain vs time response of the material confirms that the maximum strain values in tension and compression (5.63%, -5.76%) are reasonably close to the target of ±5.5%.

In addition, the stress-time curve shows that, even though the testing occurred in a single continuous step, the stress dropped to zero for a significant time (≈ 30 s). This is attributed to the mechanical slack in the specimen-fixtures-machine system. To minimise this, the addition of preload bolts is proposed for future experiments in order to enhance the rigidity of the system. However, slack due to the threads in machine (screw-driven) and specimen may not be easily corrected.

The strain-stress data in Figure 25 for the multiple cycles of tension-compression confirms the robustness of the experimental setup, showing very consistent results over subsequent cycles. All loading cycles showed very good replicability of the maximum stresses and strains.

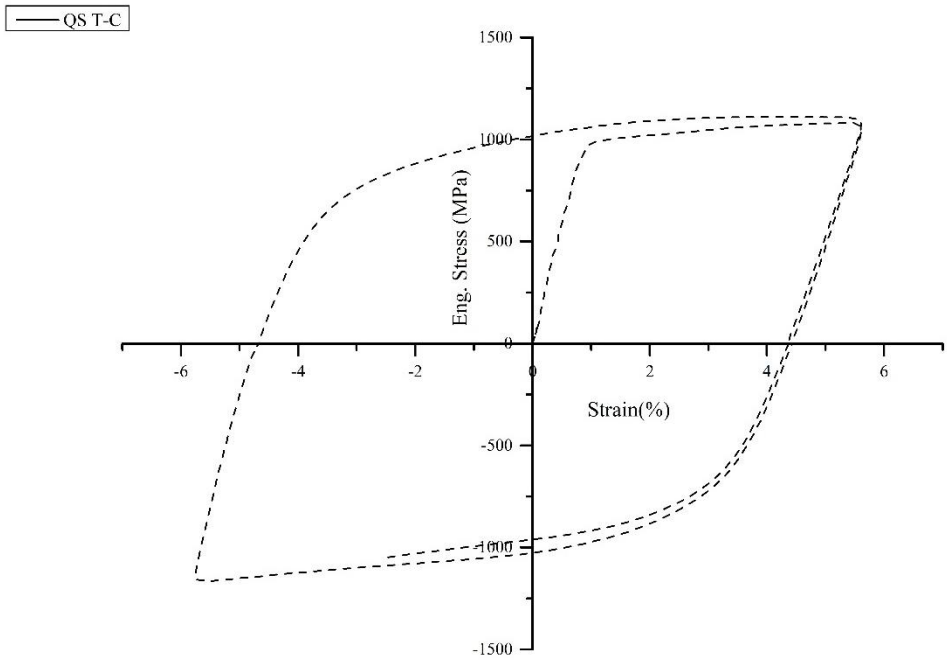

Figure 25 Engineering stress vs strain (%) for a tension-compression test in quasi-static regime.

From these results, the Bauschinger effect described in the literature review (point 2.2) can be observed after the initial forward load. Firstly, only the initial tensile load (the pre-strain equivalent to a monotonic load) shows a well-defined yield point, the rest of the loading cycles don't show a discernible transition between the elastic and plastic dominated regions of the strain-stress response. The asymmetry of the material regarding its tension vs compression response is noted, showing a considerably higher strain hardening rate in the compressive cycles versus the tensile ones, as well as overall higher yielding. However, a more detailed analysis of these effects will be given in chapter 4.

- ***Compression-tension***

The quasi-static compression-tension tests (C-T QS) were conducted using the same crosshead velocity of v=0.003 mm/s and targeted maximum strain of ±5.5% as the used in the tension-compression tests previously shown.

The results in *Figure 26* confirm what has been seen previously for the tension-compression tests (T-C QS):

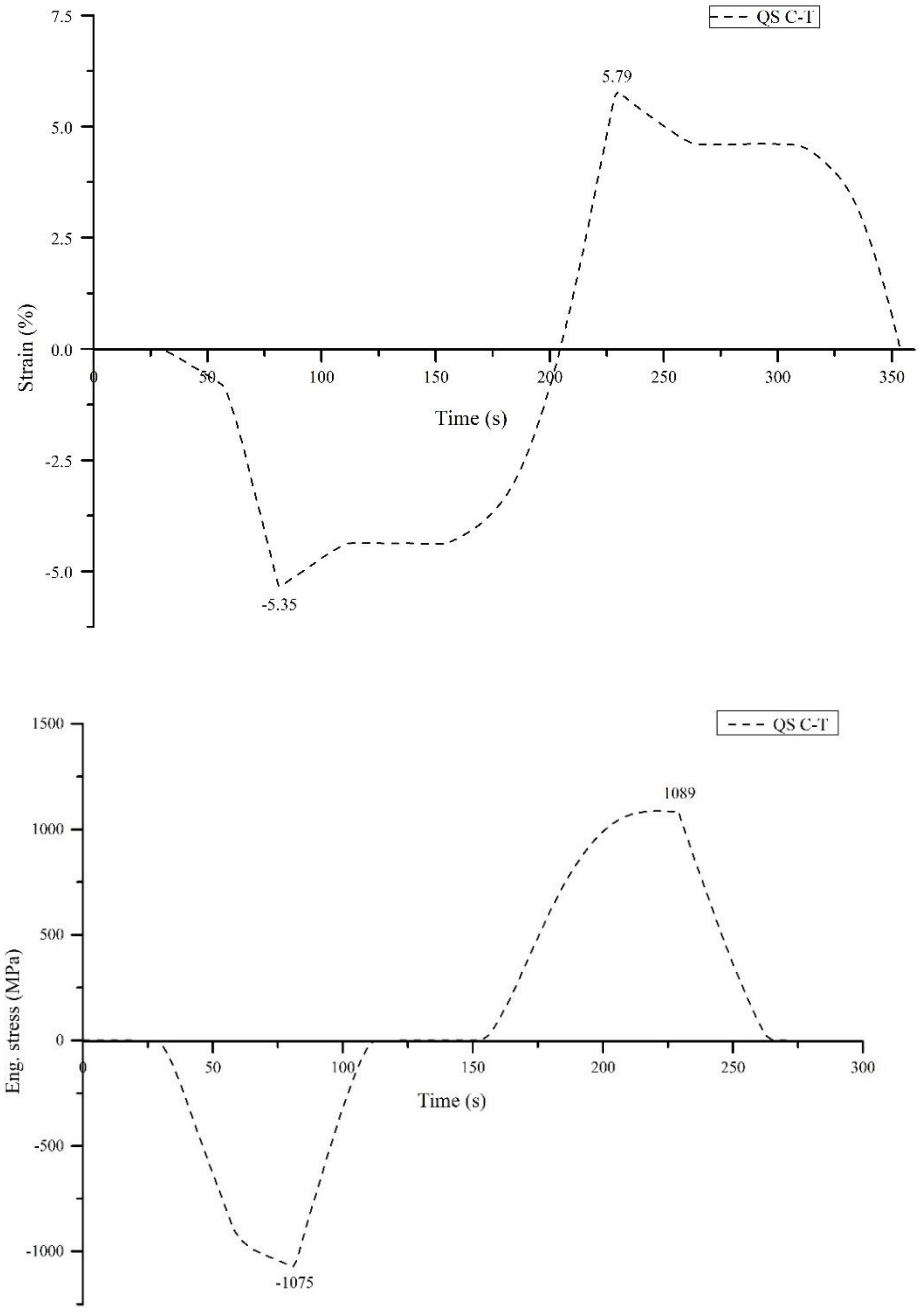

Figure 26 Compression-tension QS strain (%) vs time and engineering stress vs time for 1 completed loading cycle.

The strain vs time curve shows that the maximum strains reached (-5.35 % , 5.79 %) are close to the target value are close to the target value although a small overshoot towards tensile deformation is observed. However, since the total strain of the loading cycle matches the target,

the results obtained can be considered of great quality for the purpose of this study. In the same manner, the stress-time curve shows a time period (≈ 30 s) with zero stress during the change from compression to tension due to the mechanical slack in the specimen-fixtures-machine system of the threads and the testing.

Finally, the engineering stress-strain response of the material for the multiple loading cycles in the C-T QS tests, Figure 27, shows some imprecision in the control of the maximum strain in compression (-5.35 % 1st cycle, -5.15 % 2nd cycle, -4.9 % 3rd cycle). Nevertheless, this discrepancy should have no meaningful influence on the data acquired and its subsequent analysis.

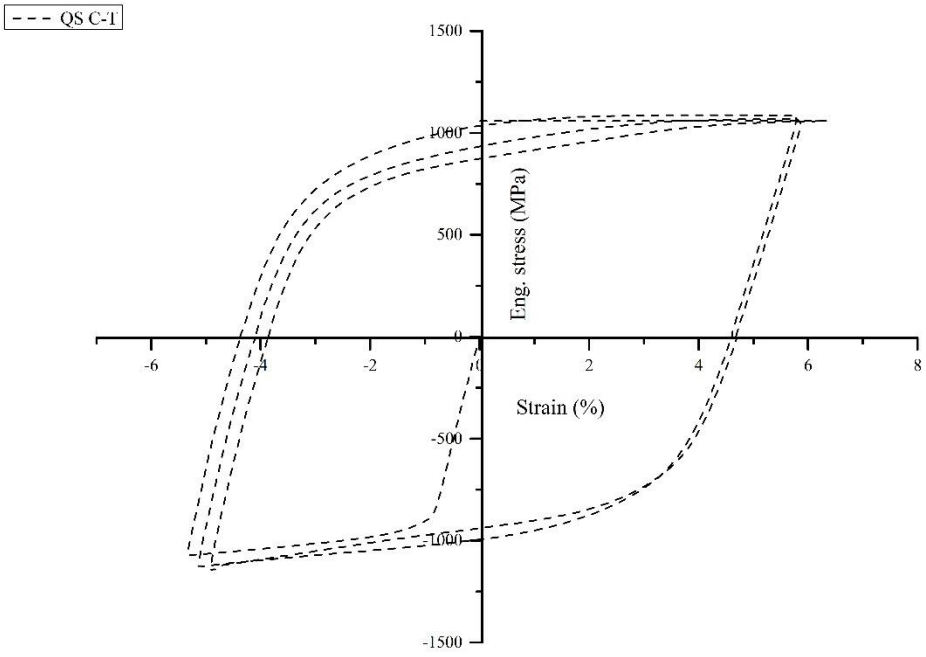

Figure 27 Engineering stress vs strain (%) for a compression-tension test in quasi-static regime.

Once again, the existence of B.E. after the first forward load can be clearly observed. As in the T-C QS case, the transition between the elastic and plastic ruled regions can be seen to change significantly after the first compressive load, with the yielding becoming more gradual in the subsequent reverse loads.

The results obtained will enable a thorough analysis of the B.E. at quasi static strain rates, including the influence of strength differential effects in chapter 4.

3.3 High-rate reverse loading

While the quasi-static reverse loading tests in the previous section presented their own particular challenges, experimentation at high strain rates becomes significantly more complex. As such, the main goal of the experimental work in this project was to obtain reliable high-rate reverse loading data on Ti64. The methodologies developed and the obtained results are presented in the following sections.

3.3.1 High-rate experimental setup

For the high-rate experiments, the systems developed by Sathianathan [10] and described in section 2.1.2 were used. Due to the experimental state of the tension-compression apparatus, and the difficulties encountered to obtain valid high-rate T-C data, the present study is restricted to the compression-tension test case. Therefore, the influence of the loading direction sequence (related to the strength differential effects of the material) and the Bauschinger effect, which requires both T-C and C-T test results, will only be investigated at quasi-static strain rates (point 3.4.1), leaving the equivalent high-rate comparison as an area for future work, along with the development of a more reliable T-C apparatus.

In the C-T split Hopkinson bar system, the compressed air is used to accelerate the impactor at the input bar and transmit a compressive or tensile pulse into the system. This first stress wave is then reflected according to the bar specifications in each case to generate the C-T reverse loading. The system is shown in Figure 28, Figure 29 and the specifics of each design are described in more detail in [10] and in section 2.1.2.

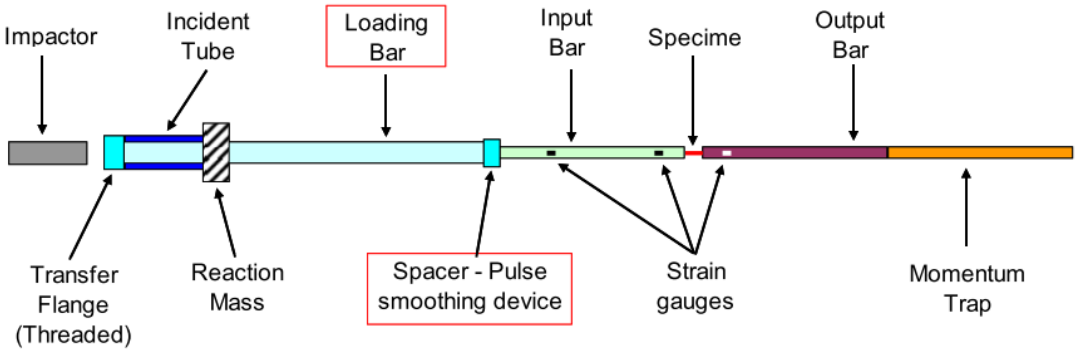

Figure 28 C-T RL SHB design by Sathianathan[46]

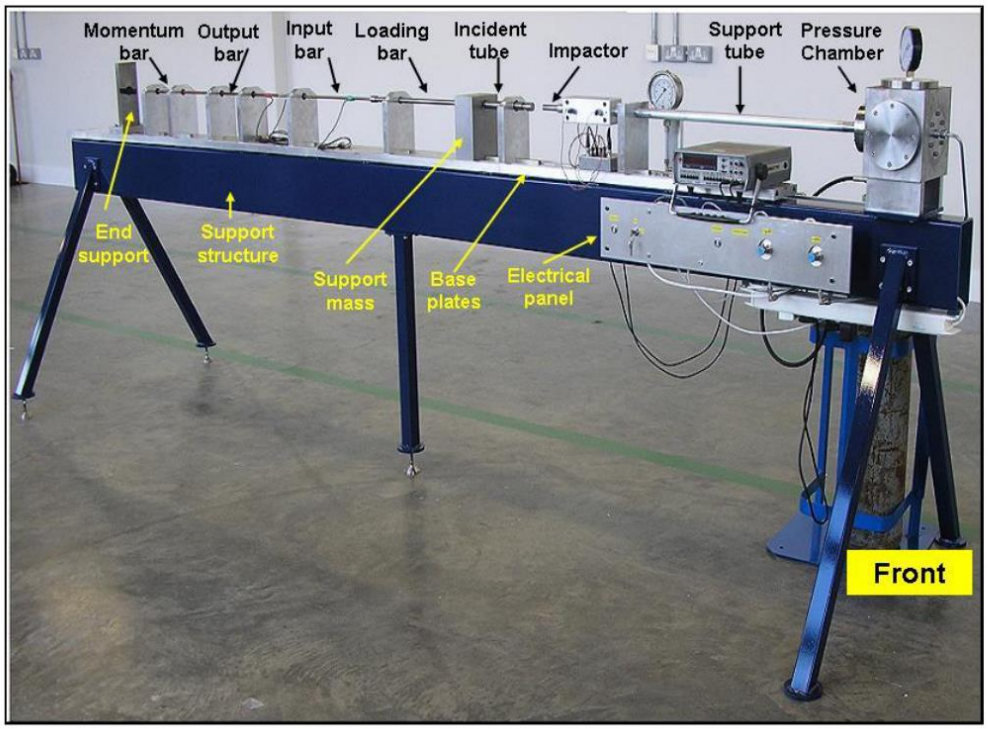

Figure 29. Compression-tension reverse loading SHB assembly [10]

During the tests, strain gauges measure the tensile and compressive waves at two different points along the input bar and at one point in the output bar. From these measurements, the forces at each end of the specimen can be determined using 1D wave superposition as described in [77].

The superposition of the incident and reflected elastic stress waves at the gauge location is tackled in the data analysis procedure hereby presented. This analysis is based on the method of characteristics and on the D'Alambert solution of wave equations, and is used to calculate the magnitude of forward and backward travelling strain waves (($\alpha(x,t)$ and $\beta(x,t)$) as functions of position and time. This allows for the calculation of the total longitudinal elastic stress and particle velocity in any selected cross section of the bar according to:

$$\sigma(x,t) = E(\alpha(x,t) + \beta(x,t)) \qquad (15)$$

$$v(x,t) = -E\rho c(\alpha(x,t) - \beta(x,t)) \qquad (16)$$

where E represents the Young's modulus of the bar material, ρ its density and c its elastic wave speed.

Figure 30 shows the Lagrangian diagram for the 1D wave propagation in a LSHB having two strain gauges G1 and G2 in the input section (INP) of the bar, at a distance $l1$ and $l2$ from the specimen, and one strain gauge G3 in the output section (OUT) of the bar, at a distance $l3$.

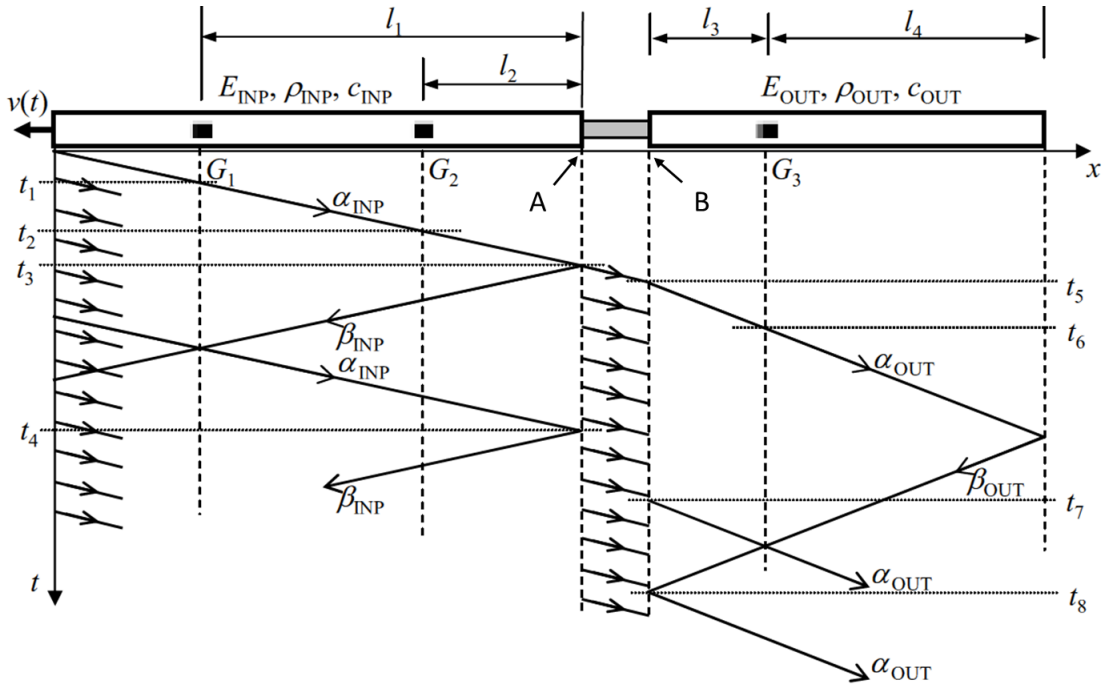

Figure 30 Lagrangian diagram for 1D propagation in the Split Hopkinson bar system [78]

The particle velocities and the stresses in the cross sections at the interfaces between bars and specimens (A and B in Fig. 28) can be evaluated from the readings of the three strain gauges by computing magnitudes of forward and backward travelling waves using the following routine:

$$t<t4 \quad \begin{cases} \alpha(xA,t)=\varepsilon(xG1,t-(t3-t1)) \\ \beta(xA,t)=\varepsilon(xG2,t+(t3-t2))-\varepsilon(xG1,t+(t3-t2)-(t2-t1)) \end{cases} \tag{17}$$

$$t\geq t4 \quad \begin{cases} \alpha(xA,t)=\varepsilon(xG1,t-(t3-t1))-\beta(xA,t-(t4-t3)) \\ \beta(xA,t)=\varepsilon(xG2,t+(t3-t2))-\{\varepsilon(xG1,t+(t3-t2)-(t2-t1))-\beta(xA,t-2(t2-t1))\} \end{cases} \tag{18}$$

$$t<t7 \quad \begin{cases} \alpha(xB,t)=\varepsilon(xG3,t+(t6-t5)) \\ \beta(xA,t)=0 \end{cases} \tag{19}$$

$$t7 \leq t < t8 \quad \begin{cases} \{\alpha(xB,t) = \varepsilon(xG3, t + (t6 - t5)) + \alpha(xB, t - (t7 - t5)) \\ \beta(xA,t) = 0 \end{cases} \tag{20}$$

$$t \geq t8 \quad \begin{cases} \{\alpha(xB,t) = \varepsilon(xG3, t + (t6 - t5)) + \alpha(xB, t - (t7 - t5)) \\ \beta(xA,t) = -\alpha(xB, t - (t8 - t5)) \end{cases} \tag{21}$$

The computed values of $\alpha(x,t)$ and $\beta(x,t)$ can then be substituted in eq.14 and eq. 15 to determine the particle velocities and stresses at the bar-specimen interfaces. However, for this analysis to be applicable the conditions of dynamic force equilibrium between points A and B must be fulfilled.

In order to obtain the stress wave measurements at points G1, G2, and G3, the strain gauges in each instrumented section were glued to the bars using a cyanoacrylate adhesive (Loctite Superglue) and connected using a half bridge configuration.

The selected strain gauges are 120 Ohm, Tokyo Sokki FLA-2-8 for the titanium input bar, and FLA-2-17 for the Phosphor bronze output bar. Phosphor bronze is a material with a very similar young modulus to Ti64 (117.8 GPa vs 113.8 GPa) while having approximately double its density (8921 kg/m^3 vs 4430 kg/m^3). This presents two advantages, all directly related to the fact that it is a material with a slower wave propagation: allowing to achieve higher strain rates in the system, and facilitating a better synchronisation between the recorded stress and the images captured during the tests.

The position of the strain gauges with respect to the interface with the specimen was measured and recorded for stress wave propagation analysis purposes, and the positioning of gauges on the opposite sides of the bar balance out any possible bending effects in the bars.

Each instrumented section of the bars was calibrated through quasi-static tension tests where the load did not exceed the elastic limit. The strain gauges were connected to the signal

amplifier used during the experiments, setting a gain equal to that used in the high-rate experiments.

From these calibration tests, a linear force-voltage correlation was obtained and interpolated (linear interpolation). The slope of the Voltage versus force divided by the gain provides the calibration factor (voltage corresponding to unit of force when gain is 1). Figure 31 shows the calibration graph for one of the gauges in the bars:

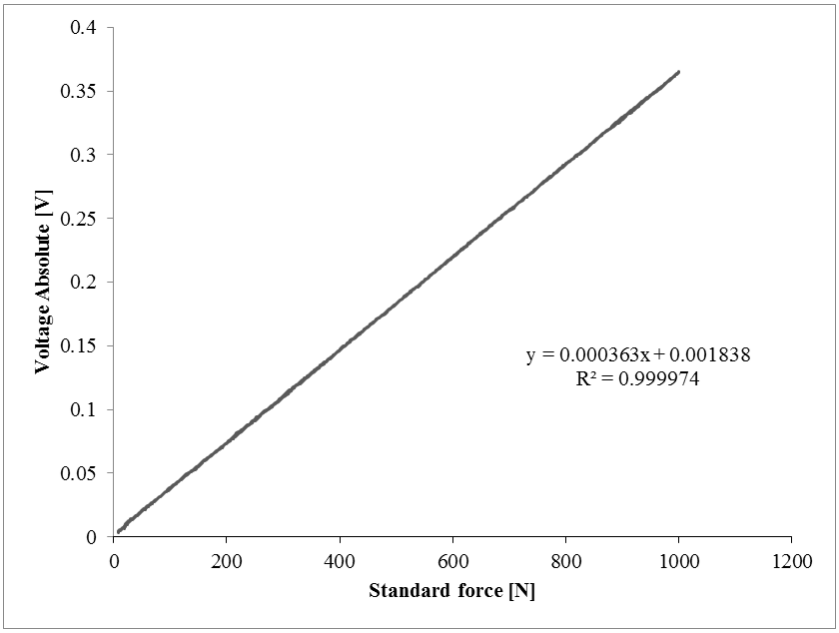

Figure 31 Voltage-force calibration for a strain gage used in the output bar in the current SHCT setup.

While the displacements can be determined through 1D wave propagation theory in a similar fashion, for better accuracy, the tests were recorded using a high-speed camera (Kirana Specialised imaging) camera coupled with a Nikon AF Micro Nikkor (focal length 60 mm, F stop 1:2.8) typically used at 600 kfps, with a resolution of 924 × 768 pixels covering an area

of approximately 30 mm × 25 mm. This allows for the full strain field data to be obtained through digital image correlation (DIC) following the procedure detailed in 3.1.1.

The usage of DIC for the strain determination allows the inclusion geometry changes in the specimen throughout the test due to barrelling during compressive and necking during tensile deformations, as well as excluding deformations outside of the gauge. In addition, the precise timings of the camera exposures were recorded along with the strain gauge signals in order to synchronise the stresses and strains.

All tests were conducted using a 1 mm thick cardboard shim (436 g/m^2) positioned in the transfer flange (see Figure 6) to reduce the transmitted Pochhammer-Chree oscillations [12] caused by the high-frequency oscillation and by the coupling between axial and radial displacements in the sample (Poisson effect).

Due to the working principle behind the split Hopkinson bar technique employed, obtaining continuous multiple cyclic testing is impossible, and therefore each one of the tests will only comprise of an individual loading hysteresis cycle. The minimum time between each test is tied to the time taken to reposition the bars and projectile to the initial shooting position and loading the gas gun. This time is clearly higher than the time required to avoid the appearance of stress recovery effects and heat dissipation, and therefore the data obtained from the tests won't be able to include factors relevant to a real reverse loading scenario comprising multiple consecutive cycles, such as the adiabatic heating.

As a final note, the experimental rig employed (described in 2.1.2) is designed to generate a symmetric stress compression-tension wave, hence subjecting the specimen to a strain recovery cycle, going from the targeted compressive strain back to the initial strain state (0% strain). This loading mode is preferred over the alternative of obtaining a full strain hysteresis cycle, as was done in the quasi-static testing. The advantage of setting for reverse loading over reverse

straining tests is the fact that this allows for the satisfactory study of the B.E. whilst minimizing the energy required to achieve the desired strains, in turn allowing the use of lower projectile velocities, less prone to induce premature failure in the strain gauges or specimen.

As in the quasi-static reverse loading case, all the results presented below serve as a representative sample of the acquired data and can be taken as validation of the experimental and analytical procedures detailed in this section

3.3.2 High-rate Compression-Tension SHB Results

The C-T tests were performed using the previously described set-up with a shooting pressure of 1.7 bar which equates to 21.54 m/s of projectile velocity, aiming for a target compressive strain of -5.5%.

Before any further analysis of the data, it is important to validate the dynamic force equilibrium requirement. As can be seen in Figure 32, showing a test with a striker velocity of 22.67 m/s, the dynamic force equilibrium between the input and output force is accomplished, validating the experimental procedure and the analytical data processing method.

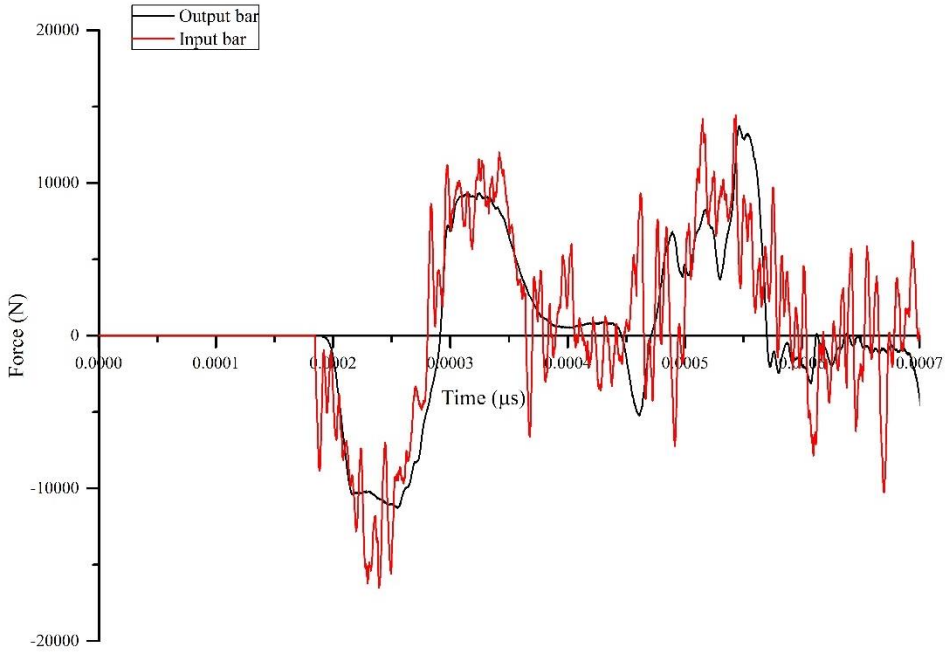

Figure 32 Input and Output forces vs time in the specimen during a C-T high-rate test.

The results in Figure 33 show that the reverse loading split Hopkinson bar system was able to reach the targeted -5.5% strain in compression with good precision (-5.64%), whereas the tensile strain reached the expected values marginally over the 0 threshold. The stress wave generated in the test is a symmetrical compression-tension wave, proving that the technique provides useful results for the intended study.

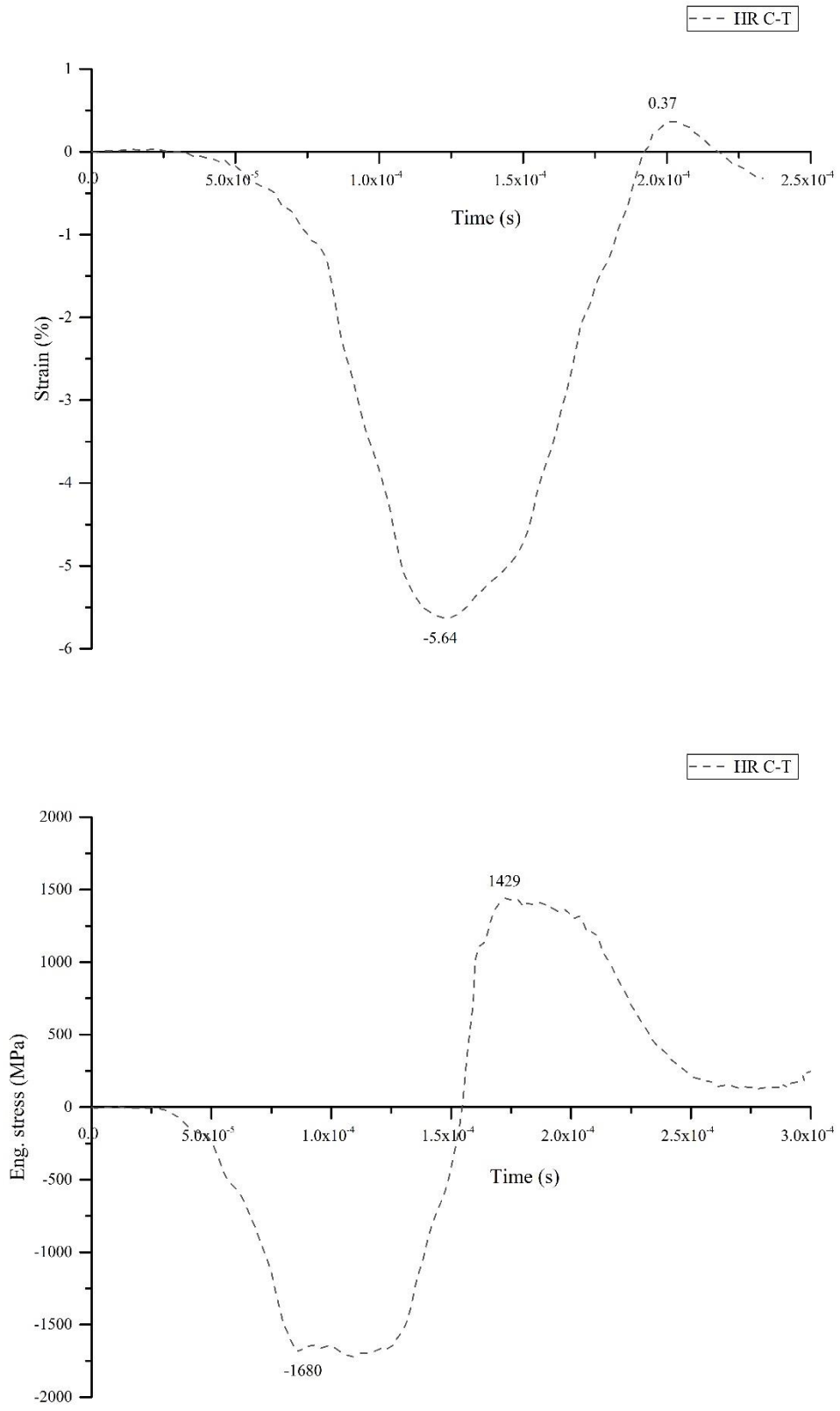

Figure 33 *Compression-tension HR strain (%) vs time and engineering stress vs time for 1 completed loading cycle.*

As expected, due to the nature of the experiments which include a change of direction along the course of the test, the strain rate is not constant, but it is reasonably symmetrical in both loading directions (Figure 34). The maximum strain rate values over the 2500 s^{-1} mark guarantees that the data obtained is indeed representative of the high-rate deformation behaviour of the material.

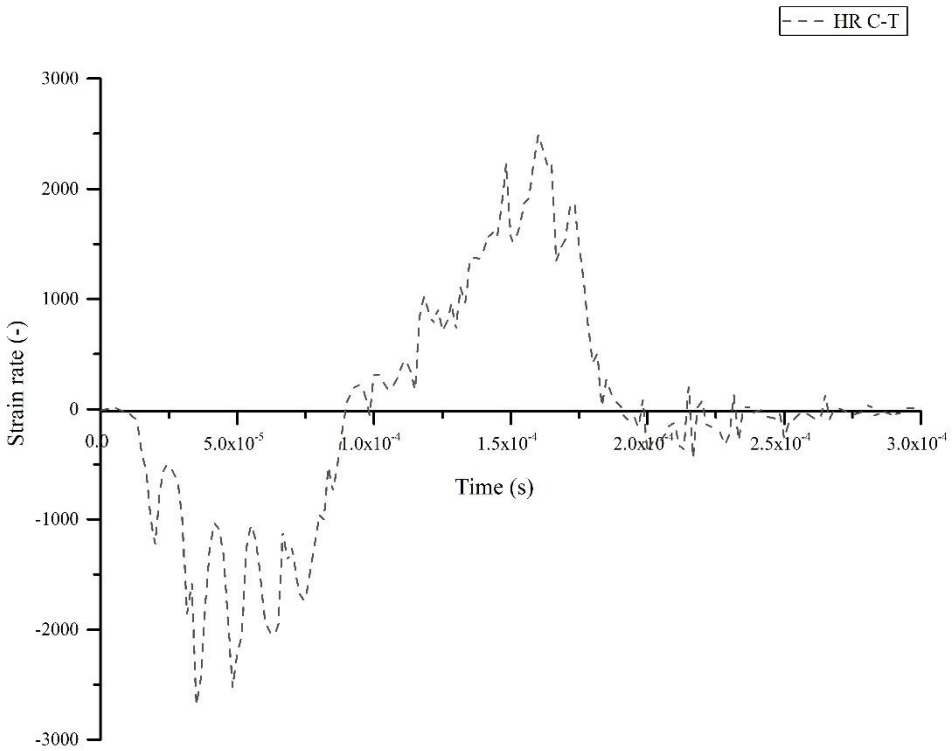

Figure 34 Strain rate vs time of a HR C-T test

The stress-strain response of the specimen under the first loading cycle, *Figure 35*, shows the presence of BE, as the yielding becomes more gradual in the reverse tension part of the hysteresis loading cycle. The referenced asymmetry between compression and tension (see

point 2.3), as well as the disappearance of a well-defined yield point in the tensile reload can be noted.

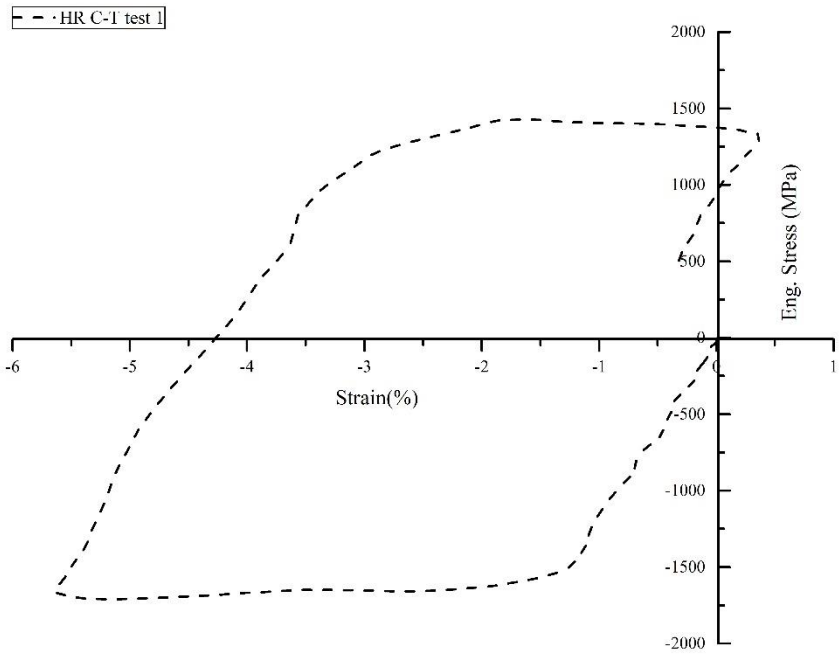

Figure 35 Engineering stress vs strain (%) for a compression- tension test in high-rate regime.

The strain rate dependency of the material is easily observed in Figure 36 when comparing the high-rate test from Figure 35 with the quasi-static strain rate test from section 3.2.2.

Finally, in order to expand the range of the study, the specimens were subjected to multiple sequential tests with the same exact testing conditions, in order to explore the effects of the accumulated cyclic loading in the material.

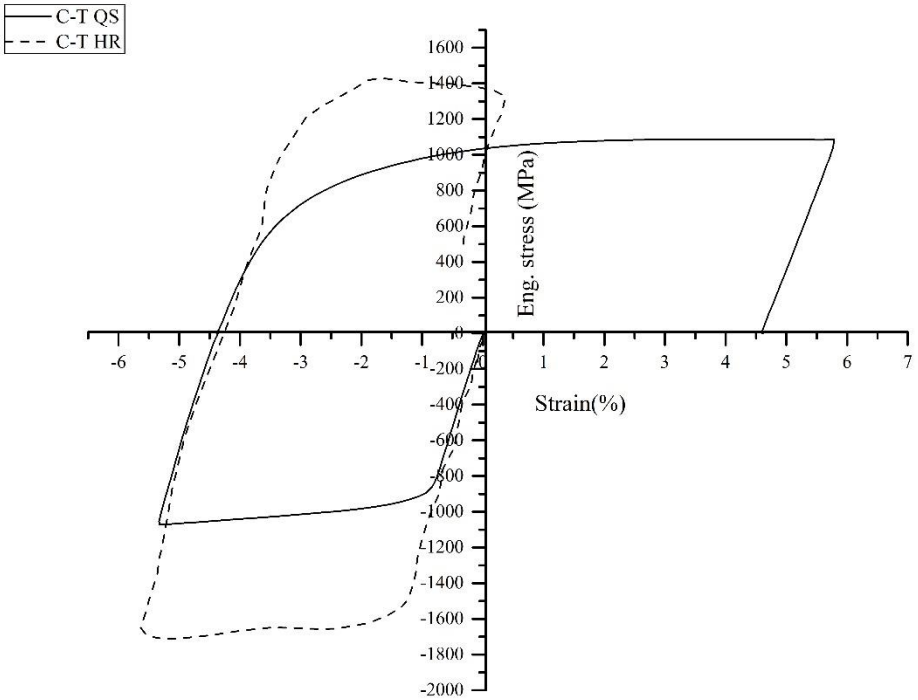

Figure 36 Stress-strain response of the material at different testing strain rates QS and HR

Figure 37 shows the stress-strain response obtained after subjecting the same specimen to three consecutive tests at the same testing conditions (Pressure 1.7 bar). The differences on the maximum strains obtained for each test are attributed to the unreliability of the compressed air system employed to propel the striker. Nevertheless, since this difference is contained under a 1% of difference in the worst of cases, the tests are completely comparable for the purposes of this study.

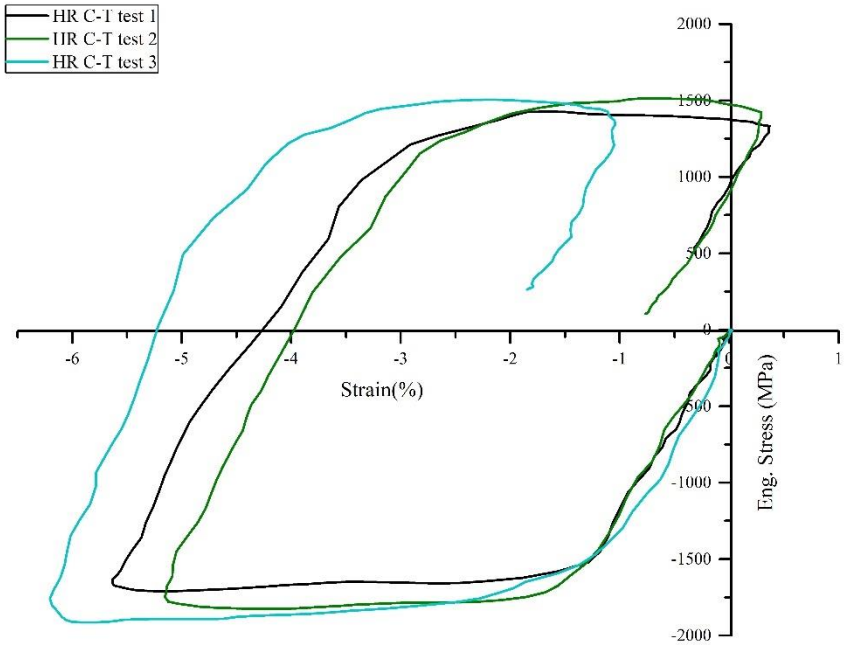

Figure 37 stress vs strain response of three consecutive tests at HR conditions

In the following chapter, a more in-depth analysis is given of this observed Bauschinger effect in Ti64 and how it changes depending on the strain rate, the direction of the forward load, or the number of cycles. However, preliminary inspection of the previous results already shows a clear difference between quasi-static and high-rate reverse loading tests and even some difference between the first and subsequent cycles for one same specimen, showing more distinct sings of Bauschinger effect as the number of cycles increases.

4. Analysis and discussion

Having successfully carried out the quasi-static and high-rate reverse loading tests on Ti64, these novel experimental results are used in the next two sections to try to answer: first, how does the Bauschinger effect manifest in Ti64 alloys and, second, how does the strain-rate affect this phenomenon. Following this analysis based on the experimental results in section 4.1, a numerical modelling study is performed in section 4.2 to evaluate leading constitutive models in their ability to describe the real material response under this kind of load.

4.1 Bauschinger effect analysis

This study aims not only at characterising qualitatively the response of Ti64 under cyclic loading, but to quantify the divergence between the monotonic "ideal" strain-stress response and the asymmetric response of the material when subjected to cyclic loads. To accomplish this, the concept of Bauschinger energy described by Muir [25] (see 2.2) is employed. The Bauschinger energy is defined as the decrease in energy required to achieve a given plastic deformation during reverse loading (due to B.E.) compared to that required for its equivalent monotonic deformation. As shown in Figure 11, corresponds to the difference between the energy elapsed on the prestrain (E_p) and the energy dissipated during the reverse loading (E_r) to achieve the same plastic strain. The difference between these energies ($E_s = E_p - E_r$) represents the difference in work dissipated (plastic work) between the pre-strain and reverse deformation after the reversal strain [33]. The ratio between (E_s) and the prestrain energy (E_p): $\beta_E = \frac{E_s}{E_p}$, may be taken as a measure of the Bauschinger effect as it reflects the stress and strain relationship as well as the rapid work hardening during reverse loading.

Defining the B.E. in the material using energetic parameters instead of stress parameters (see point 2.2) presents advantages in the cases where the reversed flow starts almost from the outset of reloading cycle as is the case of Ti64, making the identification of a distinct critical flow stress almost impossible [79], and the determination of yield stress in the reverse load very challenging.

Due to the known existence of a strong SD effect in the material studied (see point 2.3), it is necessary to introduce a nuance in the B.E. definition and concepts just described. In the classical definition, the B.E. is defined as the divergence in the material's response between a forward load (pre-strain) and a reverse load conducted in the opposite direction. Instead, here it will be defined as the difference between a pre-strain and a reverse loading both strained in the same direction, the difference being the mechanical history of the material at the start of each test. In the loading defined as pre-strain, the material starts the loading in a virgin state, whereas in the reverse loading starts it after having been loaded in the opposite direction. This modification allows to characterise the differences between the ideal mechanical behaviour of the material, equivalent to its response to a monotonic test, and its response after reverse loading.

The study presented in this chapter seeks to discern the individual effect of each factor affecting the cyclic loading response of the material and thus, distinct comparisons for each strain rate (quasi-static and high rate) and loading sequence will be included. In order to more easily identify each of these categories, the tests will be nicknamed as QS (quasi-static) or HR (high rate) depending on their strain rate, and C-T (compression-tension) or T-C (tension-compression) depending on the loading sequence employed in the tests. Within these categories, each test will be further subdivided by cycles in function of their loading direction C (compression) and T (compression) together with a counter where number 1 corresponds the initial load in each specimen, and each subsequent loading in the same direction increases the

index accordingly. Therefore, the first compressive load in a quasi-static compression-tension test will be named as QS C-T C1, the subsequent reverse tensile load QS C-T T1, and the next compressive load QS C-T C2.

In order to allow for a precise and comparable determination of the Bauschinger effect energy between all tests, they will only be considered until a maximum effective plastic strain of 3%. This value is set since it corresponds to a strain value situated well past the yield in all cases whilst allowing to phase out of the equation the differences in the strain to reverse reached in each test.

The energy dissipated in each deformation will be determined by integrating the true stress-effective plastic strain curve using a dedicated data analysis software (OriginPro Lab 9.1 by OriginLab Corporation) using the same strict integration limits in order to guarantee that the results obtained are comparable in all cases. The true stress (σ_o) being obtained through DIC following the same methodology and parameters as indicated in 3.1.1 and the effective plastic strain ($S_{eff.}$) determined through the theoretical expression:

$$S_{eff.} = S_{total} - \frac{\sigma_0}{E} \qquad (22)$$

where S_{total} correspond to the total strain of each experiment and the Young's modulus (E) has been determined experimentally with a value of 109.8 GPa.

4.2 B.E. QS

The first of the dedicated analysis will be restricted to quasi-static strain tests. Here, the loading sequence is a variable of study, and therefore, the C-T and T-C tests will be addressed separately. Due to the strength differential effects present in Ti64 both tensile and compressive cycles will also be compared separately.

- ***QS C-T***

Each complete loading cycle of the compression-tension true stress-strain response shown in Figure 38 is divided into compression and tension loadings, and named following the nomenclature advanced previously.

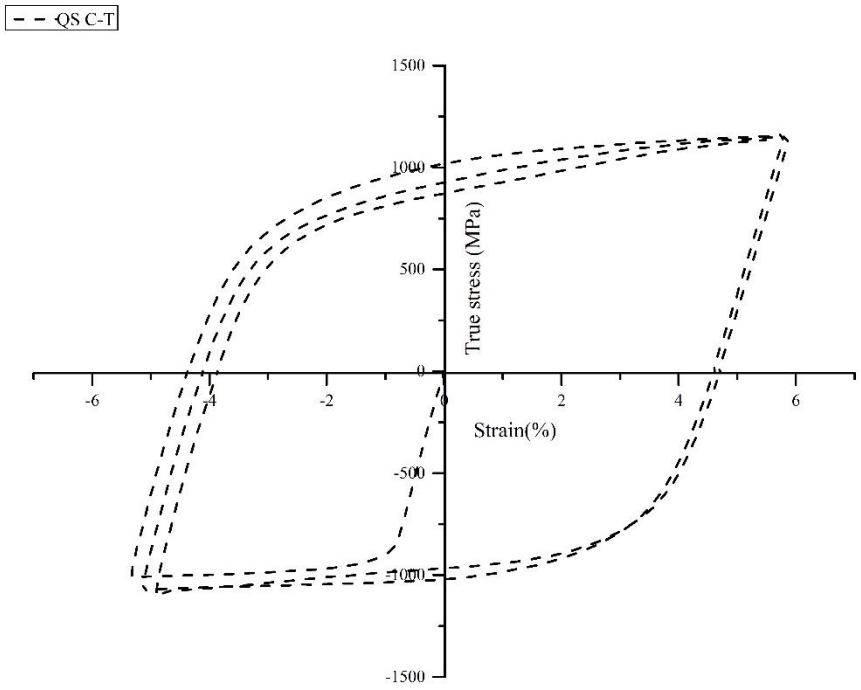

Figure 38 True stress vs strain response of the complete compression-tension quasi-static test analysed.

Plotting the absolute true stress versus the absolute accumulated strain of each separate loading cycle of the compression-tension quasi-static test allows to clearly identify them as shown in the legend of Figure 39. The known asymmetry between compression (C) and tension (T) can

be clearly observed and confirms the need for carrying out separate specific comparisons for each loading direction.

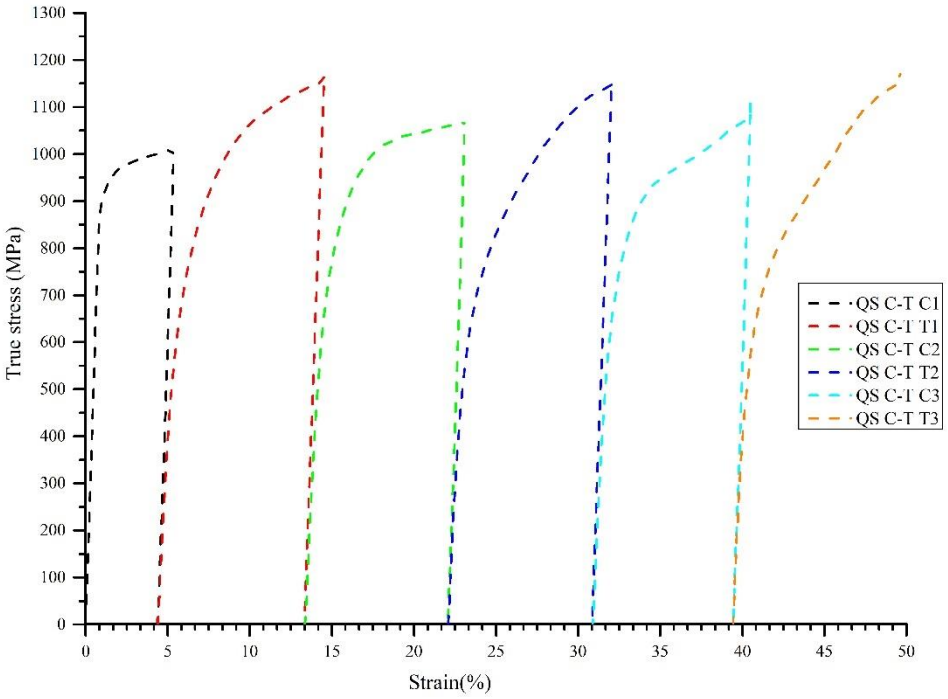

Figure 39 Absolute value of true stress vs. accumulated strain of the compression-tension quasi static response of the material.

As discussed above, due to the SD effect in the material, it is necessary to carry out separate analysis for the compression and tension loadings. The first analysis will focus on the compressive response of the material.

The true stress versus the accumulated strain of the compression cycles depicted in Figure 40 doesn't comply with the stereotypical manifestation of the B.E in metals ([80],[81]), as the documented presence of permanent softening in the reloads is not present in this case [9,82,83]. True permanent softening is defined as the permanent difference between the continued

forward stress flow curve and the inverted reverse flow curve. This definition requires that the curves become parallel. As can be clearly seen in the dotted prolongations of the flow stress for each load Figure 40 , this is clearly not the case. However the response of the material does show a noticeable loss of a distinct transition between elastic and plastic deformation (transient softening), this behaviour matches with the observations in the Bauschinger effect study of titanium-aluminium alloys by J. Paul, R. Hoppe and F. Appel in [79].

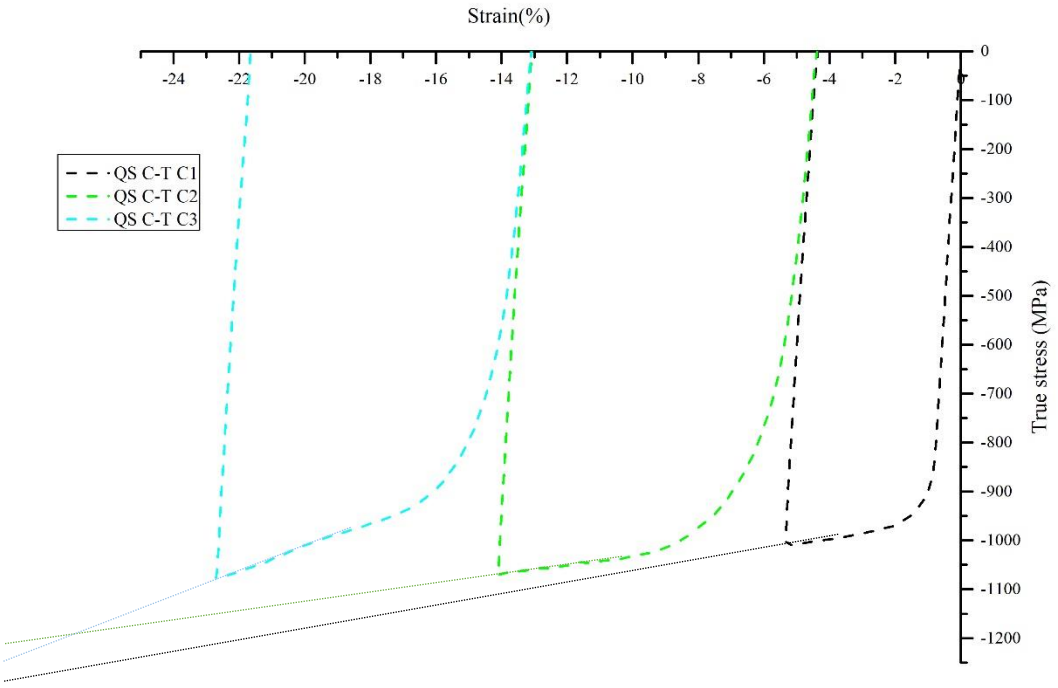

Figure 40 True stress vs accumulated strain of the compressive loads in the QS C-T test shown in Figure 38.

The comparison of the true stress vs. effective plastic strain response of the material allows for a more accurate study of the transient softening discussed above, as well as to quantify the B.E. energy parameters in the material.

The response of the material shown in Figure 41, allows to compare the first compressive cycle (QS C-T C1), equivalent to a monotonic test, and the subsequent compressive loads (QS C-T C2 and C3). The blurring of the transition between the elastic and plastic dominated regions in the Qs C-T C2 and C3 tests is very distinct, with plasticity practically starting from the onset of the curves.

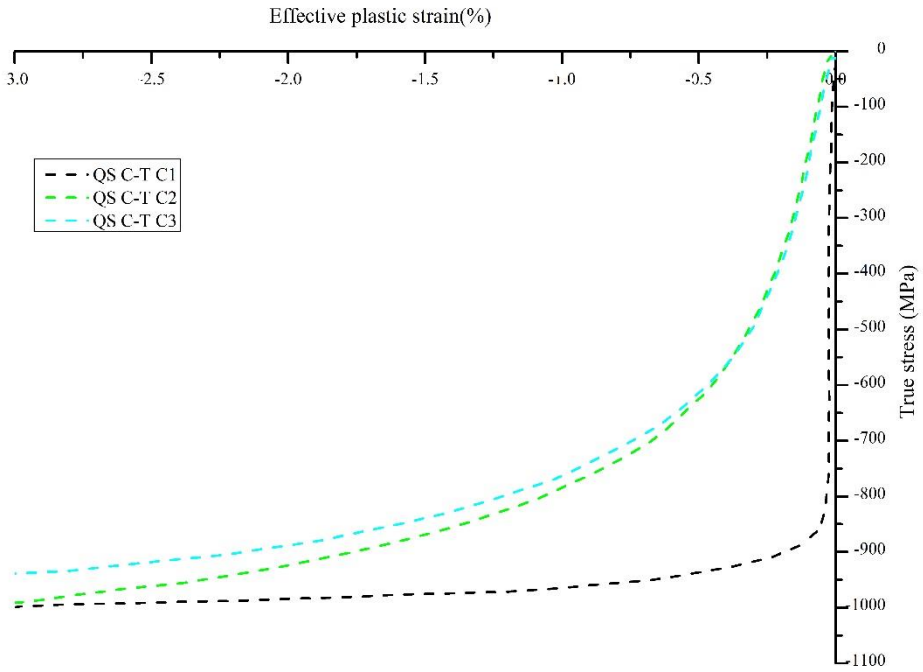

Figure 41 True stress vs. effective strain of the compression cycles of the QS C-T test.

The B.E. energy parameters (β_E) show that there is a sizeable drop in the plastic work expended during the material straining in the second and third compressions, with the QS C-T C2 β_E=0.2

and the QS C-T C3 β_E=0.225, which imply a minimum of a 20% lower plastic work in the material during the same equivalent strain as the pre-strain QS C-T C1..

- ***QS T-C***

Figure 42 shows the complete true stress vs strain response of the quasi-static tension-compression test. As in the case of the QS C-T test, each of the individual tensile and compressive loadings are named separately as per the nomenclature set in the introduction of this point.

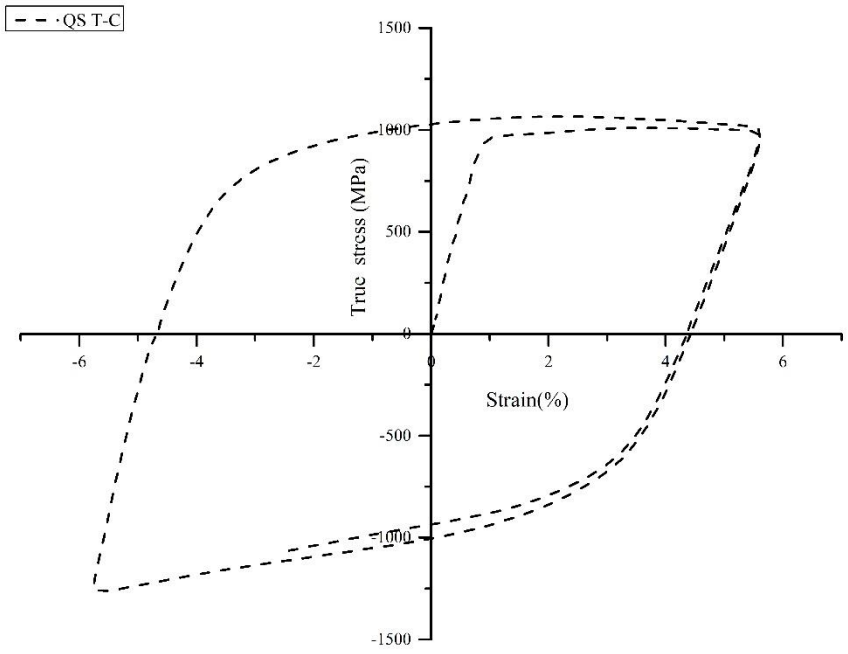

Figure 42 True stress vs strain of the complete tension-compression quasi-static test analysed.

Figure 43 allows to obtain a good overview and identification of each of the loadings constitutive of the analysed QS T-C test. The strong SD effects in the material are observed again, with clearly a distinguishable difference the strain hardening depending on the loading direction of the cycles. Despite that, in theory, the B.E. should result in the presence of permanent softening, the compressive reloads (QS T-C C1 and C2) present much higher strain hardening values than the tensile loads. Thus, the analysis of the B.E. for the QS T-C case will also be conducted segregating the loads by their direction.

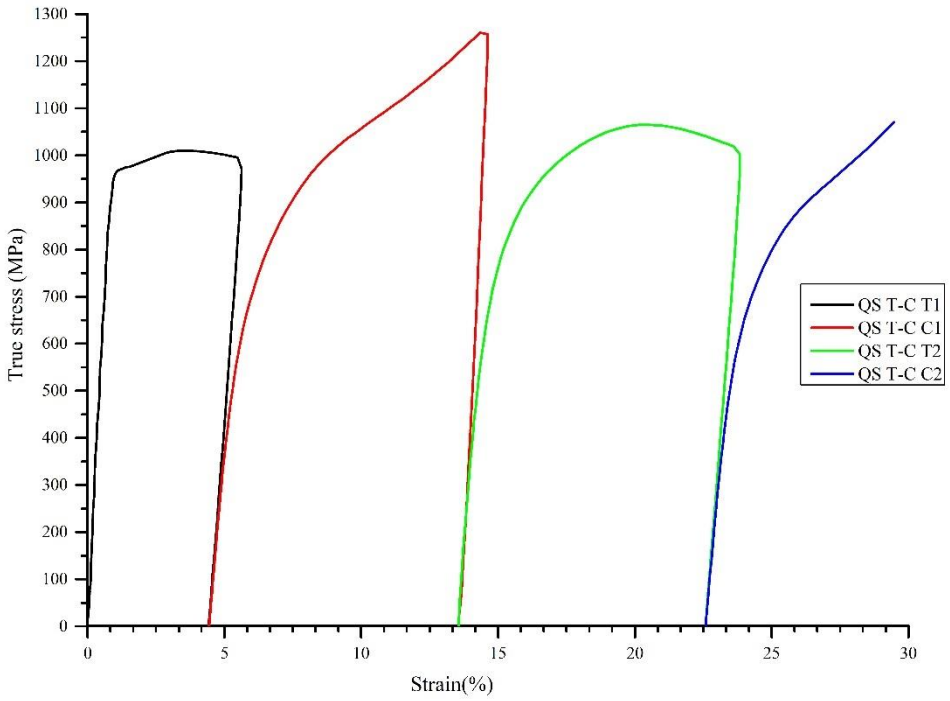

Figure 43 Absolute value of true stress vs. accumulated strain of the tension-compression quasi static response of the material.

Figure 44 shows the true stress vs the accumulated strain for the tensile cycles of the QS T-C test shown in Figure 43. As previously noted in the QS C-T test above, the main manifestation

of B.E. in the material appears in form of transient softening, a transitive elastic-plastic dominated region characterised by high strain hardenings [84]. This very long transient behaviour even reaches stress values superior to those of the pre-strain, indicating that the work hardening is much more dominant than the possible permanent softening due to the B.E.

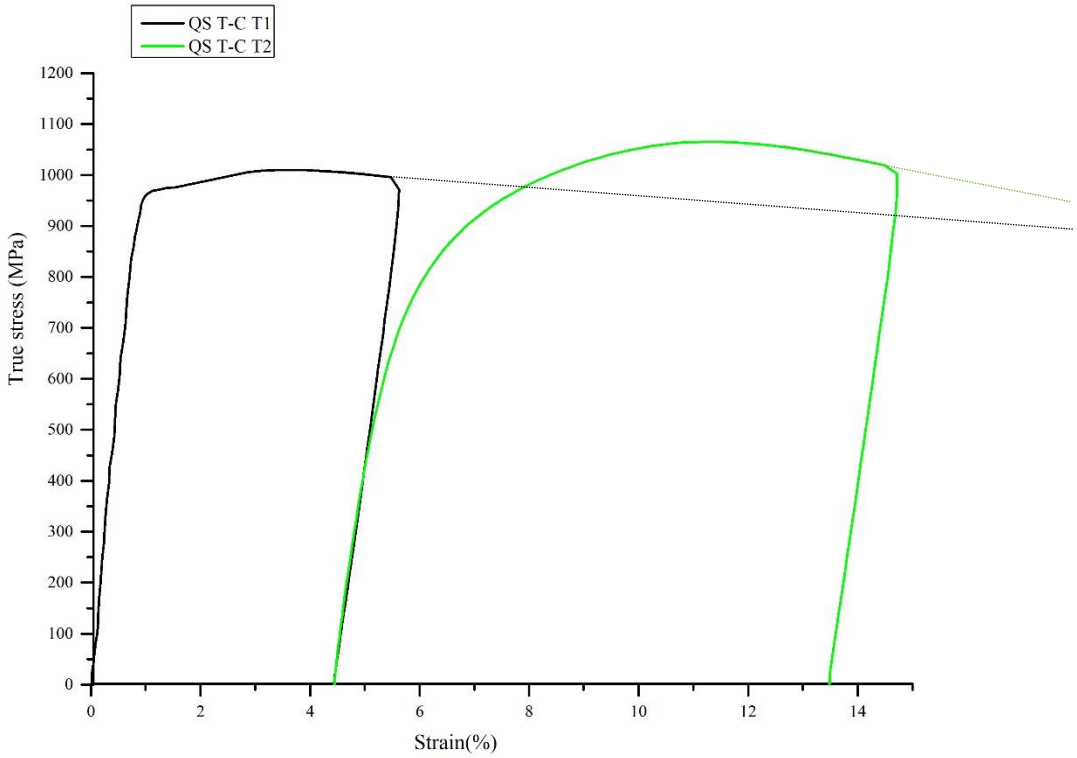

Figure 44 True stress vs accumulated strain of the compressive loads in the QS C-T test shown in Figure 43.

A comparison of the true stress versus the effective plastic strain up to 3% of the tensile cycles of the test is shown in Figure 45. The comparison shows how the second tension (QS T-C T2) presents a very distinguishable stress softening around the yielding region (around 0% of plastic strain) comparing it with QS T-C T1 which is equivalent to a monotonic tensile test.

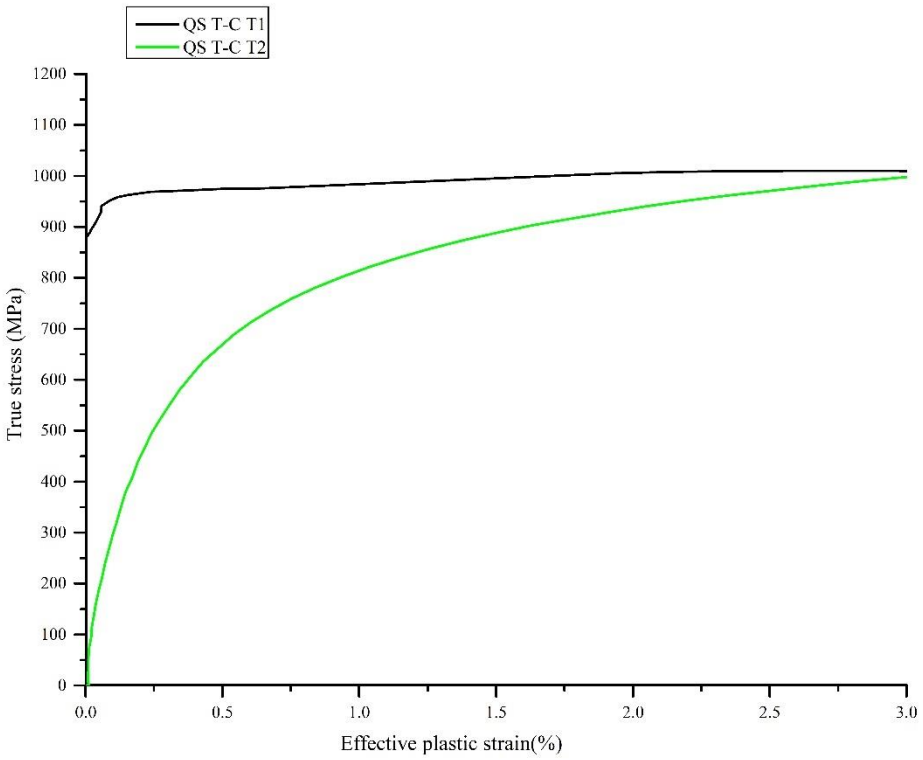

Figure 45 True stress vs effective plastic strain of the tensile loadings in the QS T-C test.

The Bauschinger effect ratio β_E= 0.173 confirms a substantial plastic work decrease in the second tensile loading QS T-C T2.

- ***Loading sequence***

Once the data of QS C-T and T-C tests has been analysed, an investigation on the effect of the loading sequence on the plastic work dissipated during the loading of the material is conducted.

By comparing, on one hand, the compressive loadings of both compression-tension and tension-compression tests in Figure 46, and on the other, the tensile loadings in Figure 47, it is possible to see the effect that the initial loading direction has on the cyclic response of the

material. Leaving aside the pre-strains QS C-T C1 and QS T-C T1, it can already be seen how the stress values are higher for the loadings effectuated in the same direction as their respective pre-strain loading. The QS C-T C2 and C3 present higher stresses than the compressive loadings of the tension-compression test, whereas the QS T-C T2 shows higher stress levels than the tensile loadings of the compression-tension test.

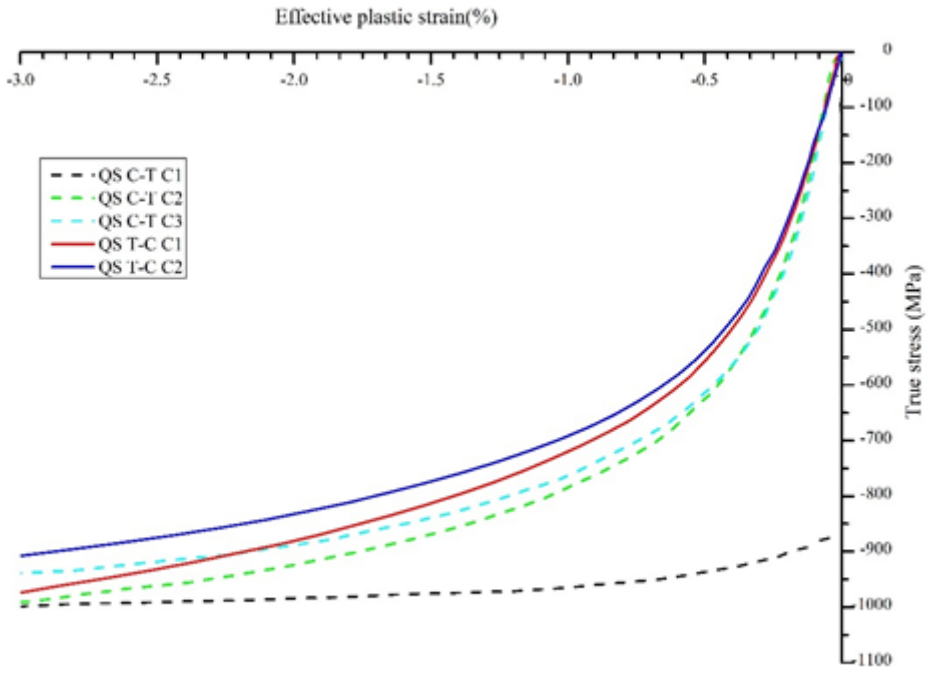

Figure 46 True stress vs effective plastic strain of all the compressive loads of both C-T and T-C QS tests.

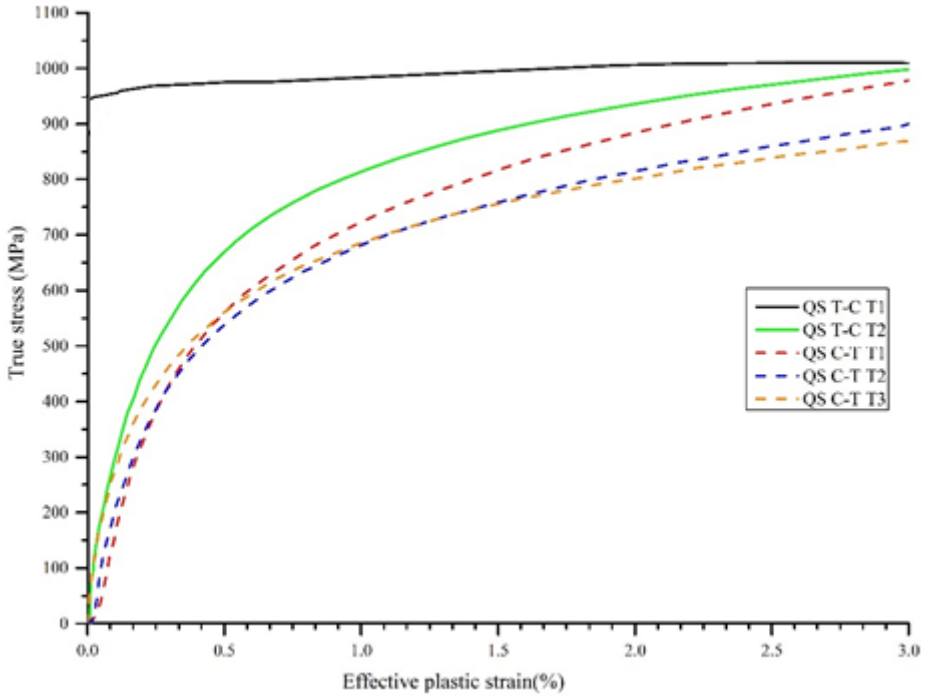

Figure 47 True stress vs effective plastic strain of all the tensile loads of both C-T and T-C QS tests.

Table 2 below presents all the results of the Bauschinger effect energy parameter determination calculated according to the procedure described in the introduction of this point (4), and allows to obtain a clearer picture of the change of plastic work derived from the Bauschinger effect.

Table 2 Bauschinger effect energy parameters of the quasi-static tests.

QS		**load**		**Plastic work (N·mm/mm³)**	**E_s (N·mm/mm³)**	**β_E (-)**
C-T	**compression**	**$E_{p\ compression}$**	**C1**	**2967.61**	-	1
		E_r	C2	2373.59	593.41	0.2
			C3	2296.58	670.42	0.225
	Tension	**E_r**	T1	2242	731.02	0.245
			T2	2096.73	876.29	0.295
			T3	2101.93	871.09	0.293
T-C	**tension**	**$E_{p\ tension}$**	**T1**	**2973.02**	-	1
		E_r	T2	2458.56	514.46	0.173
	compression	**E_r**	C1	2233.12	574.66	0.247
			C2	2120.48	646.92	0.285

The B.E. ratios (β_E) presented in Table 2 show that for both the C-T and T-C tests, the B.E. is more prominent in the cases in which the loading has been conducted in the opposite direction to their pre-strain or initial load, confirming the observed in Figure 47. This fact indicates that the initial deformation exerted during the pre-strain has a permanent effect on the material and governs its B.E., facilitating deformation in the opposite direction even after several load cycles.

However, the exact causes of this effect cannot be determined without a dedicated microstructural scale study of the microstructural mechanisms that rule B.E. (see point 2.2).

This did not fall within the scope of the present work, but it should be considered for future work on this topic.

4.2.1 B.E. HR

Once the quasi-static tests have been investigated, the study shifts towards the high-rate test results presented in 3.3.2.

The true stress-strain response of the tests shown in Figure 48 allow for a comparison that phases out the geometrical effects due to the specimen deformation during cyclic loading, and sets the basis for the following analysis of the Bauschinger effect energy parameters in this section.

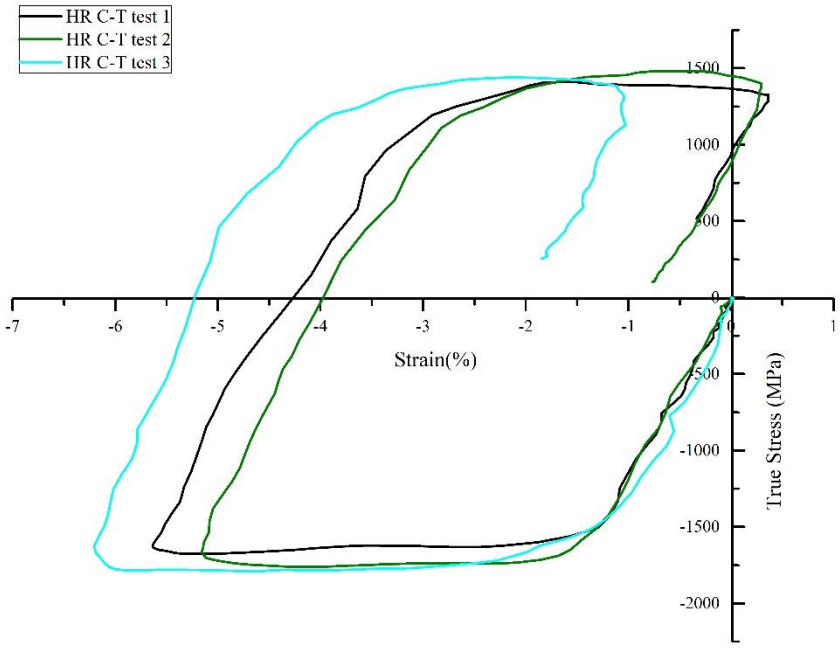

Figure 48 True stress vs strain of the three compression-tension high-rate tests included in the analysis.

Due to the already mentioned presence of asymmetry between the compressive and tensile responses of Ti64, each loading direction will be treated separately. Accordingly, comparisons will be effectuated between the compressive parts of the three high-rate compression-tension tests presented in Figure 48 on one side, and their tensile loadings on the other.

- ***Compression***

Both Figure 49 and Figure 50 show that the compressive cycles present a very similar behaviour in all three tests. The material doesn't show any prominent sign characteristic of B.E., with the reloads (cycles C2, C3) not manifesting any lowering of the yield or change in the linearity of the elastic dominated region. No permanent softening exists since the reverse flow curves (C2, C3) match the prestrain curve C1. It is important to point out that, due to the limitations of the experimental technique utilised, there are interruptions between each of the tests, whilst the quasi-static testing has been carried out in a single continuous loading.

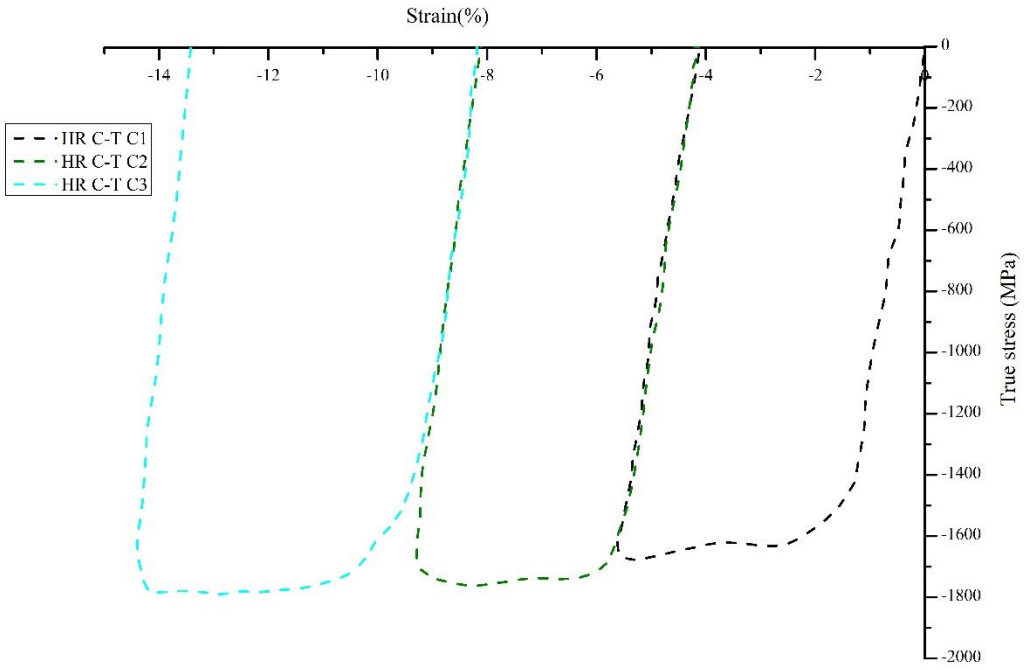

Figure 49 True stress vs accumulated strain of the compressive loadings of the three high-rate compression-tension tests shown in Figure 48.

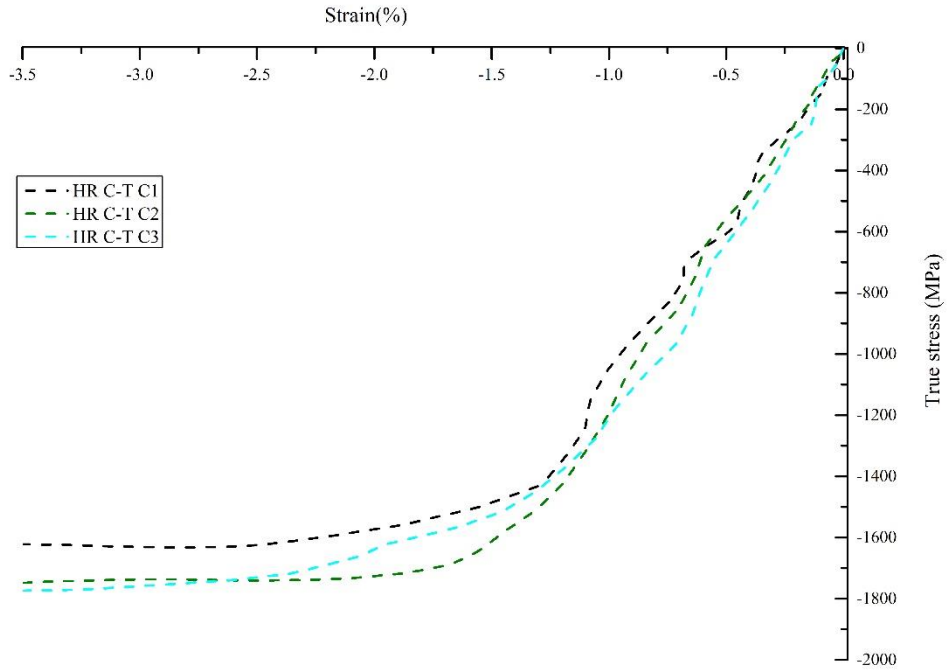

Figure 50 Detail of the yielding of the true stress vs strain response of the compression loads of the HR C-T tests.

The true stress-effective plastic strain response of the material shown in Figure 51 confirms the observed above, the there is no drop in the plastic work between the prestrain (HR C-T C1) and the reloads (HR C-T C2, HR C-T C3). The determination of the B.E. energy ratios shows a marginal increase in the energy in the reloads and therefore they don't lead to assure the presence of Bauschinger effect (β_E<0).

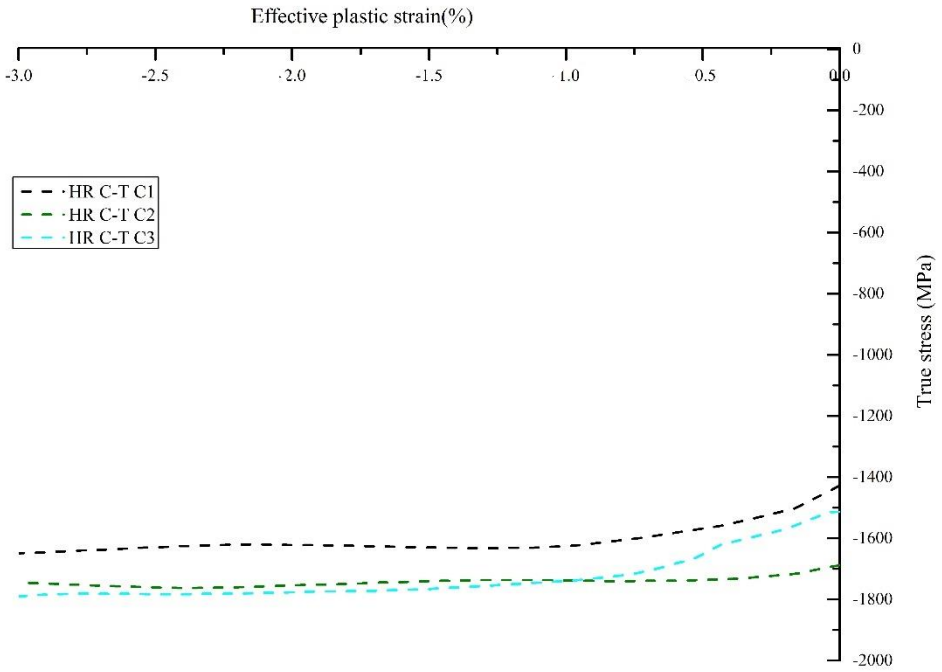

Figure 51 True stress vs effective plastic strain of the HR C-T compressive loadings.

- ***Tension***

Figure 52 and *Figure 53* show the tensile part of the material response of the tests presented in *Figure 48*. In this case, it is important to highlight that since all the tests included in this analysis present a compression-tension loading sequence, all the tensile loadings are expected to manifest B.E. since they are subsequent to a previous compressive cycle. Consequently, the

graphs referenced do not include the pre-strain that should show the ideal mechanical behaviour of the material, and instead, only are able to depict the evolution of the B.E along the repetition of loading cycles.

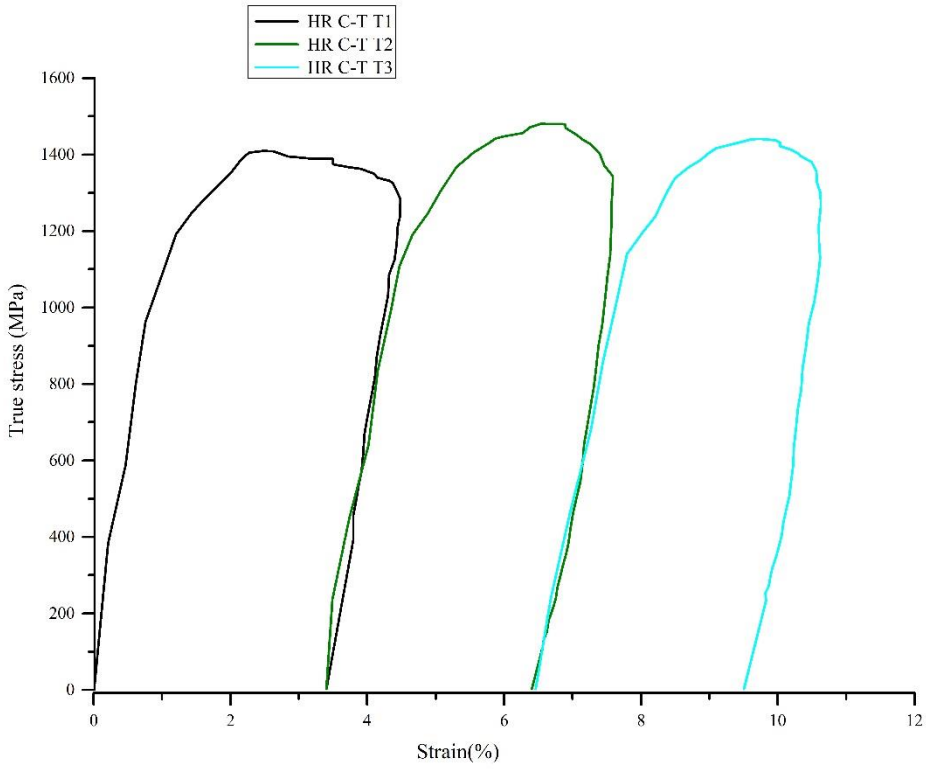

Figure 52 True stress vs accumulated strain of the tensile cycles of the HR C-T.

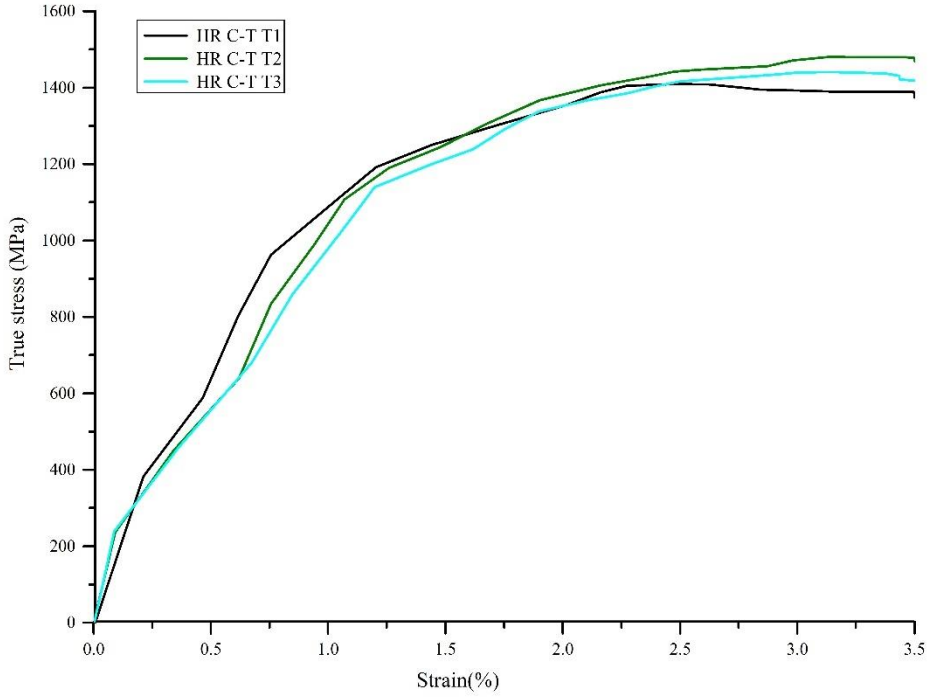

Figure 53 Detail of the yielding in the true stress vs strain response of the tensile loads studied.

The comparison between the tensile loads does not show much variation on the response of the material, and presents no noticeable changes between first and third tensile loads as can be seen in *Figure 53*. It is very interesting to observe how in contrast with the compression flow curves presented in *Figure 50* in this case the tensile curves do present a noticeable transient softening, manifested in the loss of a distinct transition between elastic and plastic dominated flows.

Figure 54 is presented below with the aim of determining the B.E. energy parameters of the tensile loads studied. The true stress vs effective plastic strain calibration curve for the Johnson Cook tabulated model [85] of Ti64 at the strain rate of 2500 s^{-1} is added to the comparison, in order to provide the data of tensile pre-strain equivalent and comparable with the reverse load cycles of the study.

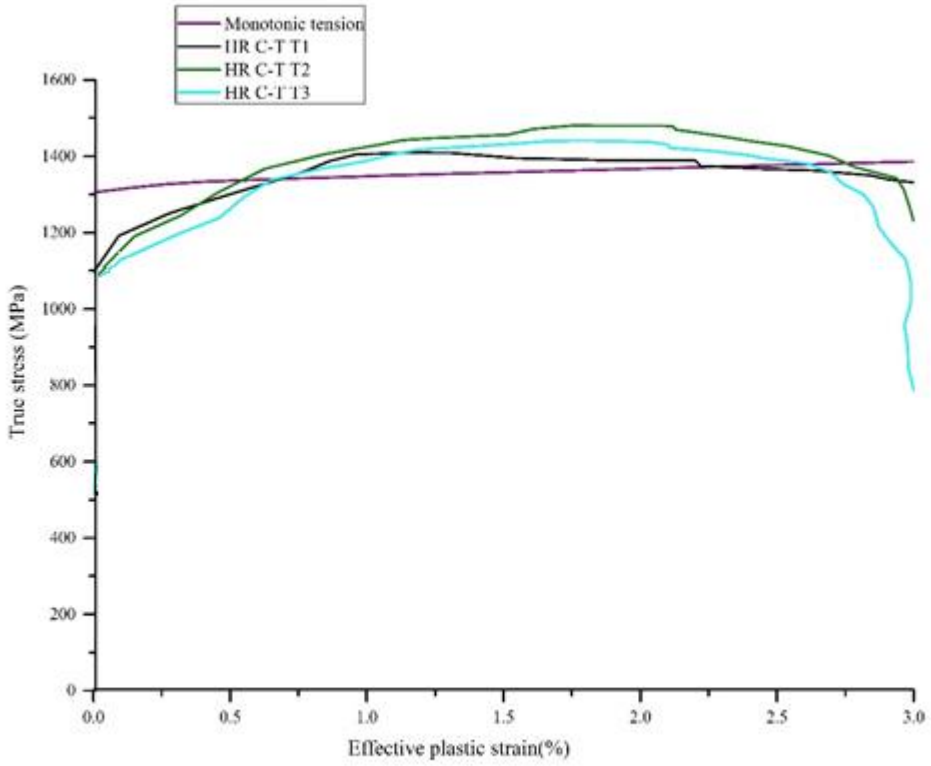

Figure 54 True stress vs effective plastic strain of the HR C-T compressive loadings.

The true stress-effective plastic strain curves in Figure 54 confirm the observed above. The reloads (HR C-T T1, T2 and T3) feature the yield lowering phenomenon typically attributed to the Bauschinger effect. The transition between elastic and plastic dominated deformation regions of the stress-strain response of the material, occur at lower stresses comparing with the monotonic curve of reference. This lowering of the yield appears to accentuate with the successive cycling of the material, with the third tensile load (HR C-T T3) presenting the lowest stress between all of them. The difference in flow stress and strain hardening between the monotonic tension and the reloads can be attributed to differences in the material, since this study could not include tensile monotonic tests of the same strains rates and exact material as

the used for the cyclic testing. The B.E. ratios calculated up to the set threshold of 3% are zero or very close for the tensile curves (see

Table 3). Nonetheless, these results need to be taken with caution before concluding that the B.E. in this case is negligible. Firstly, it is important to remark that the B.E. parameters have been calculated employing data extracted from the literature (HR monotonic tension), and therefore some of its testing conditions are going to be inevitably different (specimen geometry, experimental rig used), affecting the comparison between the two sets of data. Microstructural differences between the specimens tested in literature, and the material used in this study can also explain the differences in the flow of the material, ultimately leading to the small difference in plastic work between the pre-strain flow stress of the material and the reloads ($\beta_{E\approx}0$).

Lastly, the characteristics of the high strain rate data presented can also be a factor to account for when analysing the differences with the monotonic tensile data. The relatively long duration and notably high velocities (SR above 2000 s^{-1}) of the HR compression-tension split Hopkinson bar tests, together with the technical limitations of the currently available high-speed cameras (Kirana, Specialized Imaging), result in a limited strain data acquisition rate. The experimental nature of the reverse loading split Hopkinson system used in the testing involves the inevitable presence of noise sources in the force signals acquired (Pochhammer-Cree waves and reflections generated in the load reversal during the test). This together with the relatively small strain data pool leads to a HR experimental stress-strain response very sensitive to the mentioned noise interferences.

Nonetheless, the comparison of the B.E. characteristics between the strain-rate regimes studied allows to reckon that at high strain rates, the material shows a much more limited expression of the B.E., presenting only a certain degree of transient softening, and very reduced level of

decrease in plastic work versus the equivalent monotonic deformation. This difference may be attributed to the fact that the B.E. is mainly ruled by dislocation movement mechanisms [1,25,36] (see point 2.2), that are the prominent deformation mechanisms at QS strain rates, but aren't at high strain rates, where the twinning deformation mechanisms are more prevalent (see point 2.3) [51,53]. Consequently, the decrease in the activity of dislocation deformation mechanisms at high strain rate may lead to a minor level of B.E. at higher strain rates. However, a dedicated microstructural investigation into the differences in deformation mechanisms in each case would be required to confirm this.

Table 3 Bauschinger effect energy parameters of the high-rate tests.

HR		**load**		**Plastic Work (N·mm/mm³)**	**E_s (N·mm/mm³)**	**β_E (-)**
Monotonic		**$E_{p\ tension}$**	**Tension**	**4066.93**	-	1
C-T	**Test 1**	**$E_{p\ compression}$**	**C1**	**4816.64**	-	1
		E_r	T1	4058.49	8.44	0
	Test 2	**E_r**	C2	5228.78	-412.14	0
			T2	4174.29	-107.36	0
	Test 3	**E_r**	C3	5188.09	-1121.16	0
			T3	4004.05	62.88	0.015

In order to overcome the limitations in the B.E. determinations for HR, a wider data set needs to be acquired, including tensile prestrain test using the same matching conditions as the compression-tension high-rate data presented. Additional studies as the effect of the change of strain rate in between prestrain and reload, combining a quasi-static prestrain with a high-rate load and vice versa could also provide with a better understanding on strain rate influence on the B.E.

4.3 Numerical study

Finally, having obtained and discussed the experimental reverse loading results, a series of explicit finite element (FEA) simulations of the experimental tests (see point 3.1) using LS-Dyna have been conducted with the intention of benchmarking the performance of the models described in section 2.4 of the literature review, and exploring their capabilities regarding the B.E. in the material response under cyclic loading. The model parameters and properties for the Ti-6Al-4V alloy studied in this work have been extracted from the work of B. Cousins [86], and in the case of the Johnson Cook tabulated model from the report authored by S. Haight, P. Dubois and S. Kan [73]. In both cases the models were calibrated for monotonic loading of Ti64 at quasi-static and high strain rates.

The simulations will focus on modelling the initial cycle of the compression-tension cyclic tests presented in the previous results. This case study alone allows to evaluate the capabilities of the models to predict the material response to cyclic loading, putting special emphasis on its particularities (see point 2.3): a strong presence of strength differential effects, and the manifestation of transient softening in the yielding of the material due to Bauschinger effect. The strain rate dependency of the material will be studied by conducting two separate sets of

simulations matching the two strain rate testing conditions of the experimental testing: quasi-static (QS) and high strain rate (HR) compression-tension cyclic tests.

The specimen geometry (see 3.1) has been modelled using under-integrated hexahedral solid elements with an average size in the gauge length of the specimen of 0.1547 mm for the HR simulations, and 0.0962 mm for the QS (Figure 55). Only 1/8 of the model was simulated for the QS case, making use of the symmetry of the specimen. However, for the HR case the full specimen was modelled to better capture dynamic effects, such as wave propagation.

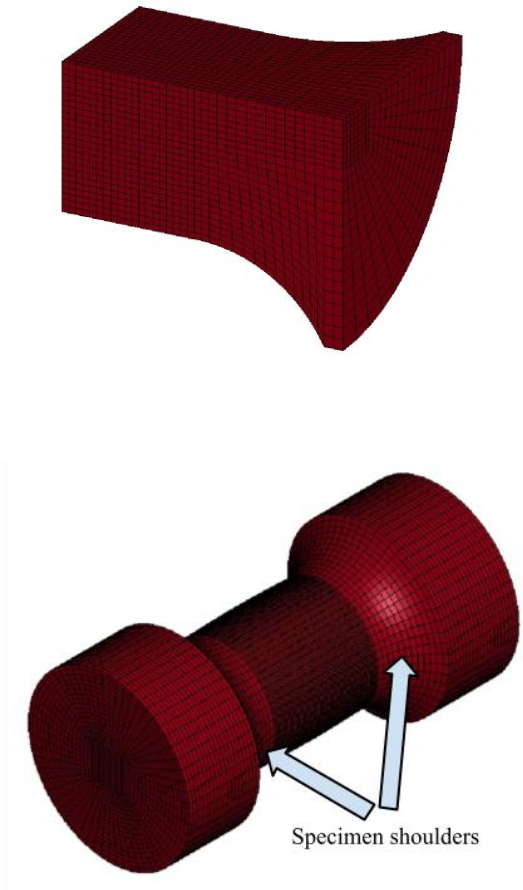

Figure 55 Detail of the meshed specimens for the quasi-static (upper image) and high rate (lower image) simulations.

Specific displacement inputs for each simulation set have been generated using the DIC methodology already detailed (3.1.1) to determine the relative displacements between the specimen shoulders.

The testing conditions for each simulation are reproduced by fixing one end of the specimen, whilst applying the displacement inputs to the other. Once the simulations were concluded, the average stresses at the input and output of the specimen and the strain along the gauge length were extracted to compare against the experimental results. This allows to acquire data of the simulations equivalent to the experimental data whilst avoiding the need to model the whole experimental rig used in the testing.

4.3.1 QS simulations

The quasi-static compression-tension simulations take as reference the experimental test presented in Figure 27 (crosshead velocity of v=0.003 mm/s).

Selective mass scaling is introduced in the simulations in order to reduce the computational times while retaining a satisfactory level of accuracy, since all simulations were using an explicit time integration solution scheme in LS-Dyna. Mass is augmented automatically in order to obtain a minimum time step of 5.00E-07 s, which allows to achieve reasonable computation times. In order to validate that the results retain a physical validity, it is key to make sure that the kinetic energy is negligible in front of the internal energy due to the mass introduced. As can be seen in Figure 56, the validity conditions described above are fulfilled, allowing to ensure that the artificial mass increase added and its consequent increase in the inertial forces does not alter the solution of the problem simulated.

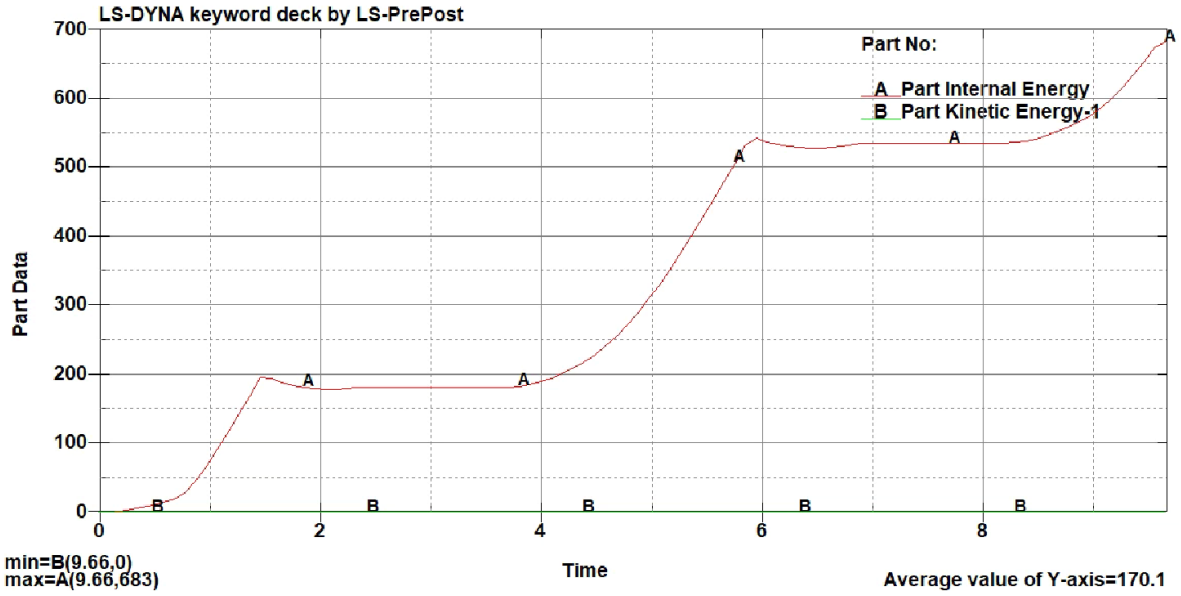

Figure 56 Internal and kinetic energies in a quasi-static simulation.

The results of the simulations are presented next. Figure depicts the true stress-strain response for all models included. The experimental reference test is attached in order to allow for the direct comparison and evaluation of the accuracy of the models.

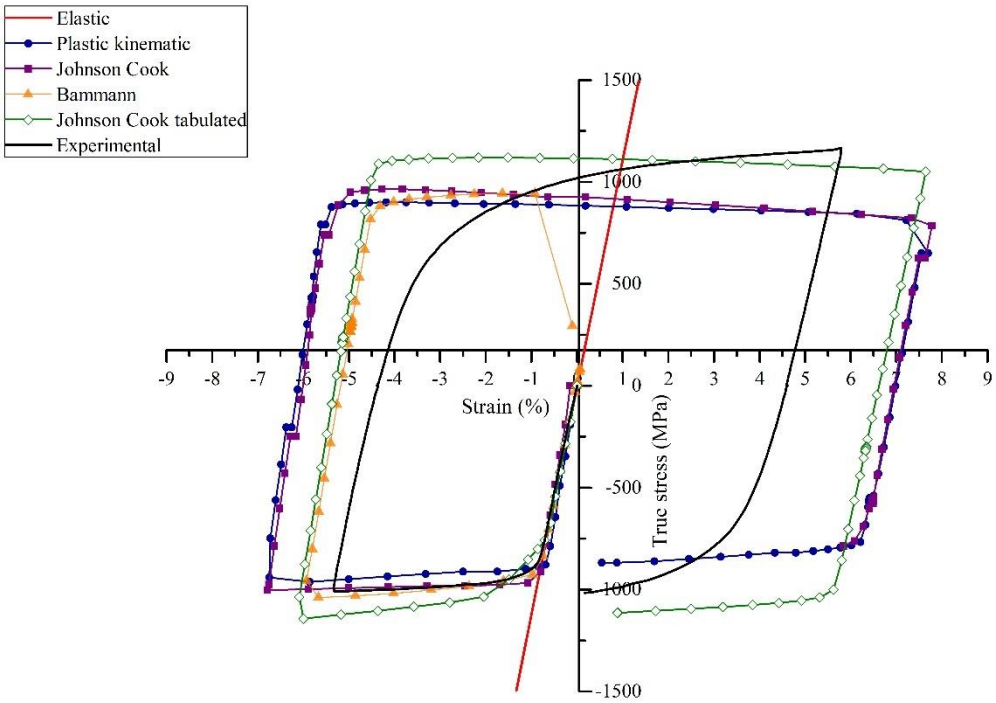

Figure 57 True stress vs strain of the quasi-static response comparison between the constitutive models included in the study and their reference experimental test.

Before entering into the comparison between the simulation results, it's necessary to note that for all models (with the exception of the elastic model, only included to serve as validation of the elastic properties of the material for the simulations), the simulations overstate the strains reached during the test. This can be explained due to the existence of non-negligible deformations outside the gauge length of the specimen during the compression-tension experimental cyclic testing. In particular, these deformations are considerable at the shoulder region of the specimen, where deformations in the longitudinal direction reach values of a 1.3%. These deformations are not predicted accurately in the numerical study, where under the ideal conditions of the simulations, the maximum strains in the shoulders only get to a 0.7% in

strain. This discrepancy in the deformation in the specimen shoulders contributes in the difference in the strains calculated in the gauge length. In light of this, the 1/8 model and the boundary conditions applied for the QS simulations may have been overly simplified, limiting the amount of deformation outside of the gauge length. In addition, the fact that the parameters of the models have been calibrated primarily using high strain-rate data, relying on the strain-rate scaling capabilities of the models to simulate the quasi-static test may be an additional factor adding up in the divergence observed.

In any case, while the simulation of the QS test cases could be improved, the obtained results already show the inability of the different constitutive models to describe the B.E. in quasi-static reverse loading.

In addition, the Bammann constitutive model presents poor damage parameter calibration at quasi-static strain rates, predicting a premature failure in tension that doesn't comply with the reality in any of the experimental tests conducted in this study. Since the failure occurs past the yielding point in the reverse load, the model is included in the analysis as it allows for the analysis of the B.E. prediction aptitude of the model.

All models show an acceptable level of accuracy predicting the flow stress of the material in compression, however all but the Johnson Cook tabulated model tend to overstate the strength differential effect of the material, showing a sizeable difference with the experimental data presented in the stress values of the flow stress in tension.

None of the models are able to represent the transient softening attributed to the B.E. described in the experimental material response in the section 4.2 B.E. QS. The difference is very clear due to the contrast between the acute, clean yielding of the simulations with the experimental progressive nonlinear transition. The subsequent analysis of the plastic work will shed more light into these differences.

The true stress vs effective plastic strain curves for each model, shown in Figure 56 and 57 for the compressive and tensile parts of the compression-tension cycle, confirm the importance of the B.E. for the constitutive models to be able to predict the response of the material.

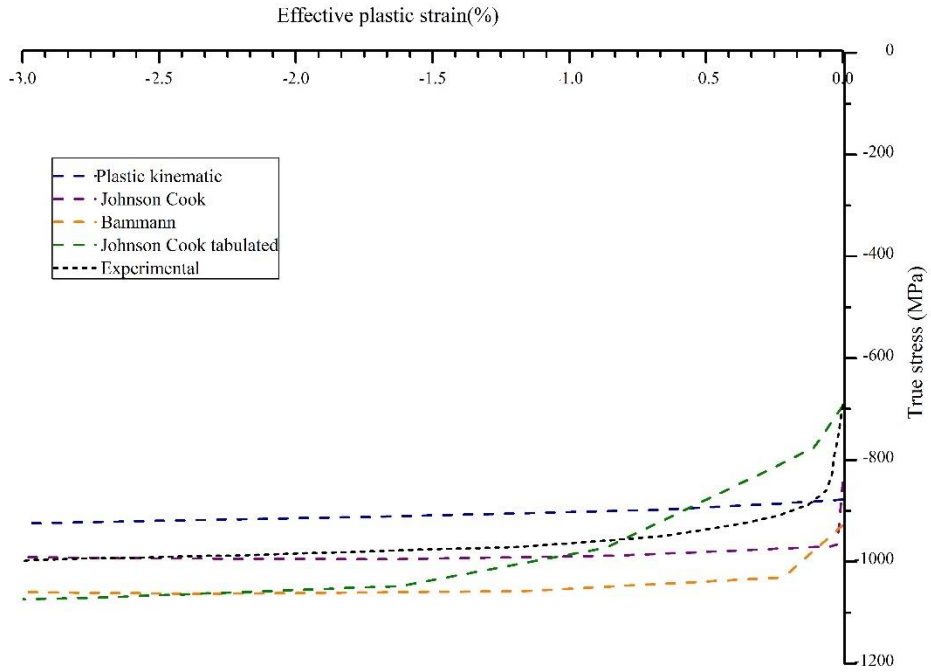

Figure 58 True stress vs effective plastic strain of the QS C-T compressive loadings of the models included in the numerical study and the experimental test of reference.

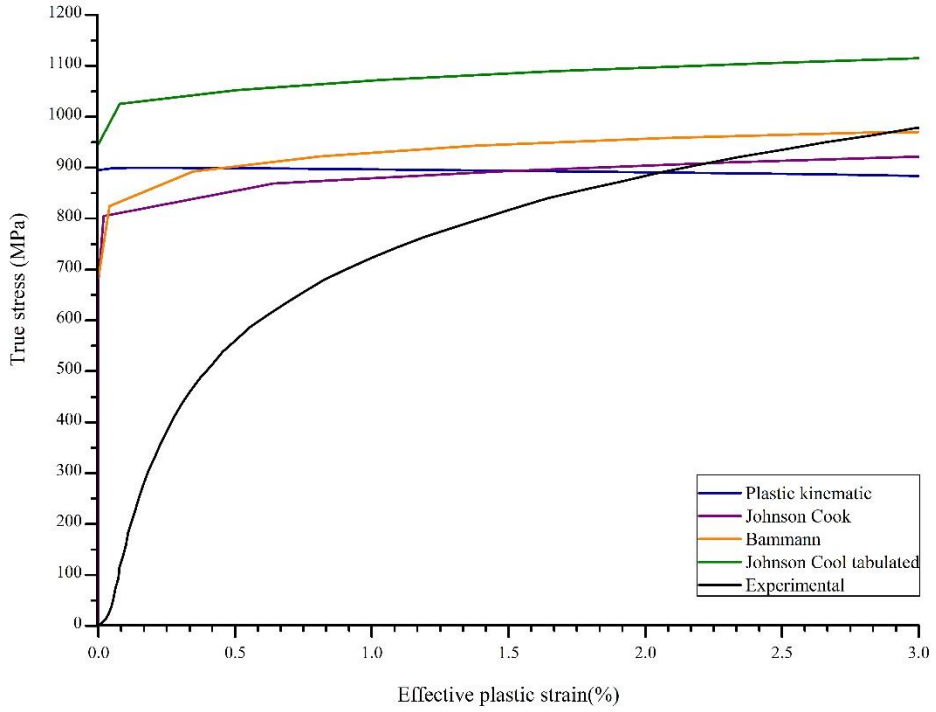

Figure 59 True stress vs effective plastic strain of the QS C-T tensile loadings of the models included in the numerical study and the experimental test of reference.

In compression all models show a very similar behaviour to the shown by the experimental test, with some minor variation in the yield stress and hardening slope. On the other hand, for the tensile part of the cycle (Figure 62) it can be clearly seen that this is not the case, and that the presence of B.E. in the experimental response of the material induces significant differences that the simulations are not able to predict. The B.E. in the experimental data not only manifests in the yield of the material and induces a significant difference in the plastic work exerted during the material straining, but also affects the whole flow stress of the material in the tensile reload, as the wide transition between the elastic and plastic deformation caused by the B.E. also introduces a very acute strain hardening compared to the model predictions.

Therefore, the B.E. is shown to be a major factor in the ability of these models to accurately predict the cyclic loading response of Ti64 at quasi-static strain rates and proves to be an important factor in order to obtain reliable models of the material to complex loading conditions.

4.3.2 HR simulations

The high strain rate simulations take as reference the experimental compression-tension test depicted in Figure 60 (maximum strain rate in the test of 2000 s^{-1})

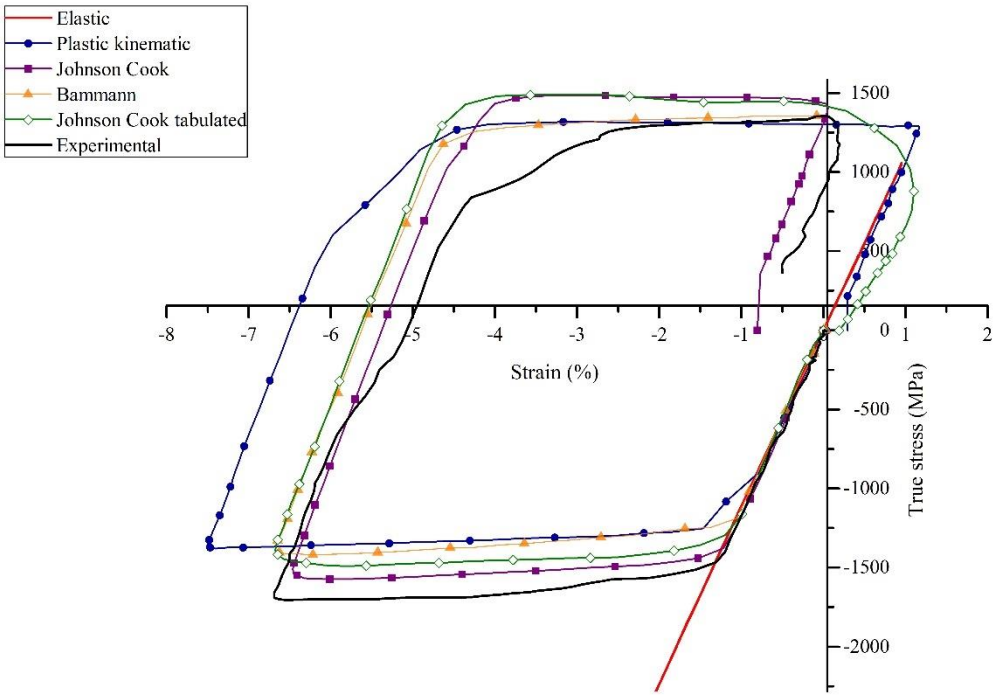

Figure 60 True stress vs strain of the high-rate response comparison between the constitutive models included in the study and their reference experimental test.

Figure 60 shows a better accuracy of the simulations, predicting a much closer response of the material when comparing with the QS case. This is in line with the factors mentioned above that the calibration of model parameters is mainly carried out at high strain rates, and that as shown in the previous section 3.4 the B.E. is much less prominent at high strain rates.

The main inaccuracies in the simulations are centred in underestimating the strain hardening in the first compressive part of the cycle, and in predicting the flow stress of the material in the tensile part of the cycle. Where it appears that the transient softening typical of the B.E. in Ti64 affects the yield as well as the strain hardening.

Figure 61 and Figure 62 allow to compare the plastic work exerted in the material during the simulated test for each model and for a clearer picture of the differences between the simulations and the reference test.

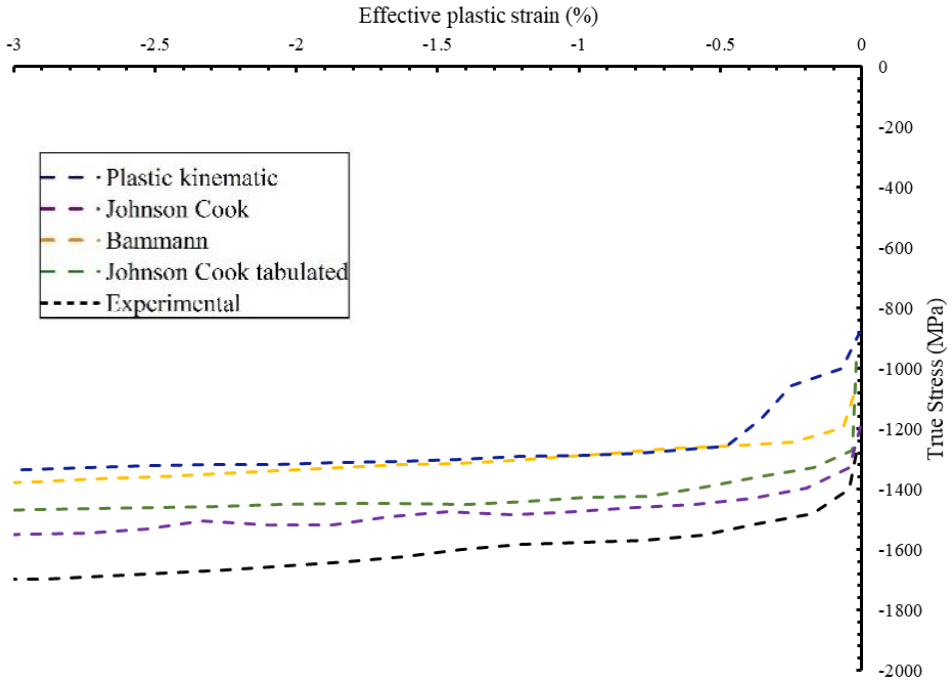

Figure 61 True stress vs effective plastic strain of the HR C-T compressive loadings of the models included in the numerical study and the experimental test of reference.

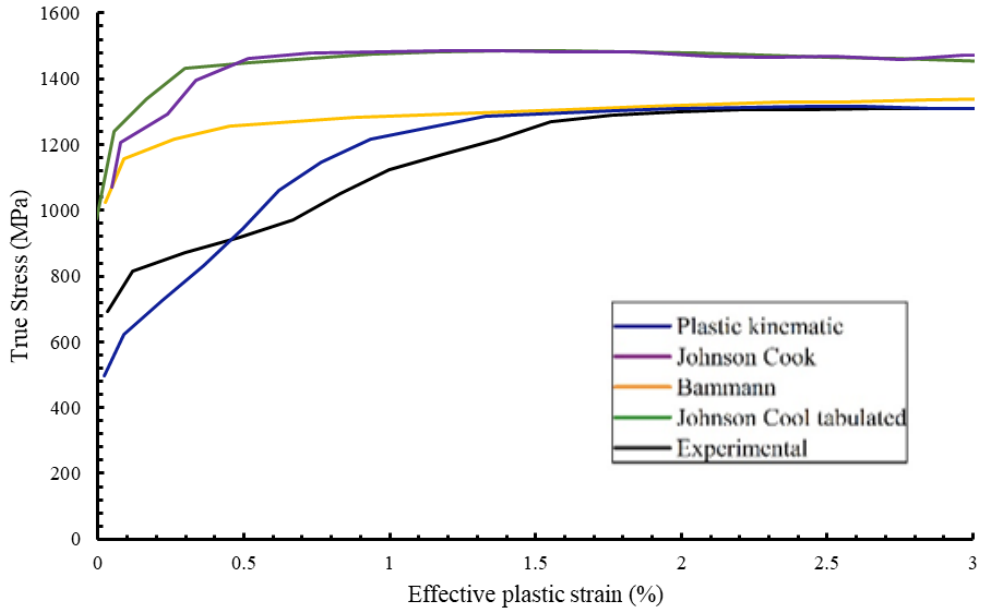

Figure 62 True stress vs effective plastic strain of the HR C-T tensile loadings of the models included in the numerical study and the experimental test of reference.

The simulations understate the hardening of the material in all cases, and as can be seen in Figure 61 the flow stress of the experimental test shows significantly higher stress levels. The fact the B.E. presents a much lesser degree of importance in the reverse loading response of the material at high strain rates can be confirmed in Figure 62.

However, although the degree of B.E. observed in the HR test is significantly reduced in comparison to the QS tests, there is still a noticeable effect in the reverse tension load. The slight reduction of the yield stress and change in the hardening behaviour is best captured by the plastic-kinematic model, while all others show no significant B.E.

The fact that the plastic kinematic model presents a reasonable description of the Bauschinger effect at HR but not at QS may point to a change in micro-scale deformation mechanisms affected by the strain rate, slipping dominating the quasi-static response of Ti64, and twinning

being more prevalent at high strain rates (see 2.3). Furthermore, also indicates that, in a phenomenological manner, it may be possible to describe the differences in the Bauschinger effect at different strain rates in Ti64 by using a combination of isotropic and kinematic hardening, where the ratio between the two is also rate-dependent to reflect the change in micro-scale deformation mechanisms.

5. Conclusions

The review of the literature showed a lack of studies on the reverse loading of titanium alloys that include strain-rate and strength differential effects. In addition, it revealed that the study of the Bauschinger effect under dynamic loading conditions is a vastly uncharted topic for any metal, and that the understanding of deformation mechanisms in Ti64 and its interaction with the Bauschinger effect, is still not complete.

The experimental campaign presented in this work provides significant novel data for the study of the Bauschinger effect under dynamic loading conditions in Ti-6Al-4V alloys and enables the specific analysis of the strain rate effects on the reverse loading response for the material. The analysis of the data acquired shows that for Ti-6Al-4V alloys, the Bauschinger effect manifests principally in the form of a noticeable loss of a distinct transition between elastic and plastic dominated deformation regions (transient softening) [79], and the presence of plasticity at very low stress levels, well below the theoretical yield stress of the material. This phenomenon has as consequence the lowering of the plastic work expended on the deformation of the material when subjected to cyclic loading.

The study of the effect of the initial load or prestrain direction on the quasi-static reverse loading response of the material, shows that the Bauschinger effect is more prominent in the cases in which the loading has been conducted in the opposite direction to their prestrain. This fact indicates that the initial deformation exerted during the prestrain may have a permanent effect on the material and governs its Bauschinger effect, even after multiple subsequent load cycles.

The analysis of the cyclic response of the material under quasi-static and high strain-rate regimes allows to identify an inversely proportional relationship with the B.E.

At high strain rates, the material shows a much more limited expression of the B.E., presenting only a certain degree of transient softening, and very reduced level of decrease in plastic work versus the equivalent quasi-static deformation. This difference may be attributed to the fact that the manifestation of the B.E. is directly linked to the presence of dislocation movement deformation mechanisms, more prominent at QS strain rates than at high strain rates, where the twinning deformation mechanisms are more prevalent [1,53,62,64].

The numerical study conducted shows that general, widely used constitutive models calibrated with monotonic data are not able to predict accurately the cyclic loading response of Ti-6Al-4V alloys, and proves that the Bauschinger effect is an important factor to account for in order to obtain reliable models of the material's response to complex loading paths.

The work presented in this study offers a new insight on the mechanical characterization of Ti-6Al-4V, proving the relevance of the Bauschinger effect as influence factor in the modelling of the mechanical response of the material under cyclic loading, and determining its interaction with the strain rate effects in the Ti-6Al-4V alloy studied.

6. Future work

In this section, a series of improvements and measures to progress further in the study of the Bauschinger effect in Ti-6Al-4V alloys are proposed. The measures and dedicated studies presented in this chapter are twofold: on one hand, they consist of improvements to the experimental methodology presented in chapter 3 and the proposition of new experimental test designs and, on the other hand, of a series of requirements to accurately model the Bauschinger effect in Ti64.

In turn, these proposals are presented in two different formats, as a series of propositions to expand the study conducted in this thesis, and as exploratory preliminary studies, which present a higher level of development. The later are presented in the section 7 Annex A., since they are more of a complement than an expansion the work presented in this thesis.

6.1 Experimental proposals

6.1.1 Proposed improvements of the existing experimental methodologies.

The first of the proposed measures to improve the current experimental capabilities in the study of the B.E. is to adopt a video extensometer strain control system to replace the laser extensometer system used in the quasi-static experimental campaign in this work (section 3.2). This upgrade would allow to improve the reliability of the current testing methodology, that currently disposes of a low success rate and leads as consequence to avoidable time and resource inefficiencies.

For the case of the high-rate testing methodologies presented in chapter 3.3, a preliminary study of the current capabilities and the possible improvements to introduce is presented below.

6.1.2 Microstructural and texture analysis of the material

A comprehensive study of the microstructure of the material studied should be a top priority to any future work centred on the topic presented in this thesis.

Since, as shown in this work, the Bauschinger effect is directly tied to the microstructural deformation mechanisms present in the material, having a good understanding of the texture (grain size, orientation), and of the microstructure characteristics of the material (inclusions, dislocation, twinning) would allow to reach a deeper understanding of it.

Doing a study of the material's microstructure "as received" (before any testing), and after each of the reverse loading cycles would allow to correlate the microstructure evolution in the material to the B.E. manifestation shown by the material in its mechanical response. Analysing the microstructure of the material after quasi-static and high-rate tests would also shed light to the interaction between slipping and twinning deformation mechanisms and B.E.

There are several techniques that could allow for the aforementioned characterization: for texture characterization and twinning in the material optical micrographs, SEM micrography and EBSD would be very useful. X-rays diffraction and CT scanning techniques could be employed to the study of the materials microstructure evolution in-situ, while the material is subjected to the mechanical testing and allowing for a much deeper analysis of the microstructure and its evolution during reverse loading.

6.2 Ti-6Al-4V cyclic loading modelling advances

As shown in the chapter 4.3 of this work, most widely used constitutive models are not capable of representing the complexity of the response of Ti-6Al-4V alloys under cyclic loading.

In this section a review of more advanced constitutive models not so widely used at this time, is presented as part of the future work proposed to expand on the modelling work presented, focusing specifically on the requirements to accurately model rate-dependent cyclic loading and the observed Bauschinger effect in the material.

In order for a constitutive model to accurately predict the response of Ti-6Al-4V alloys under cyclic loading at quasi-static and dynamic loading rates, it must account for the non-linear stress-strain response of the material, strength differential effects, and strain-rate, temperature effects. Damage mechanics will be left out of the scope of this work since they are not relevant for the characterization of the elastic and plastic response of Ti-6Al-4V in this study, where the maximum strain will be well below the threshold of void and damage initiation

Based on a deeper review of the literature, two preliminary candidates have been identified that may best fit the requirements of this study.

First, the model developed by Cousins [86] proposes a physically-based thermodynamically consistent model within the field of Internal State Variable (ISV) to study the pressure, strain-rate and temperature dependent deformation processes in Ti-6Al-4V. This model is based on the BCJ model, or Sandia Damage Model, expanded by Bamman and Aifantis [89] to include kinematic hardening and the effect of directional stresses. However, while it complies with most of the main requirements of this study, the ability of the model to predict the response under reverse loading has not been addressed and may require further investigation.

Second, Tuninetti and Habraken asymmetric and anisotropic yielding model with an added temperature dependence for Ti-6Al-4V [2] is able to account for the orthotropic and asymmetric behaviour of the material . However, it can’t account for the stress softening characteristic of the Bauschinger effect and it has not been tested for high strain-rates, where anisotropy may be less relevant [86].

An extended investigation by Khan et al. [90] included the effects of anisotropy, temperature, strain rate as well as multiaxial non-proportional loading, although no considerations were made regarding the adiabatic conditions at high strain rate. Furthermore, these authors did not include either kinematic hardening necessary to reproduce the load reversals appearing during a high-rate impact event.

With this in mind, further work to evaluate these two models with the novel QS and HR reverse loading data obtained in this work could give some interesting insight into the best modelling approach for the description of Ti64 under reverse loading at different strain rates.

7. Annex A

In this section a series of works centred on enhancing and development new solutions for a split Hopkinson compression-tension reverse loading bar is presented.

7.1 Reverse loading split-Hopkinson pressure bar enhancement study

As explained in section 2.1. The University of Oxford's Impact Engineering Laboratory (IEL) disposes of a series of equipment and methodologies to do so. The first step of the proposed improvements is to commission the existing experimental rig and determine their main limitations.

The main criteria considered in these evaluations are:

1. Reliability: The capacity of the methods to deliver the desired strain values consistently.
2. Single step: The transition between forward and reverse loads should occur minimizing interruptions to avoid elastic stress relaxation effects and allow the study of the effect of adiabatic heating at high strain rates.
3. Strain reversibility: Strain recovery is needed to study the B.E. in the material, therefore the techniques evaluated have to be able to do a full strain cycle.

The main areas to introduce improvements are: (i) the momentum trapping capabilities, to eliminate some of the remaining reflections with the aim of conducting reverse loading tests with a more controlled loading history; and (ii) improving the efficiency of the load reversal, in order to, on one hand, lower the minimal strain in the forward load that the bars are able to reverse and, on the other, to conduct full strain cycles in the material.

Numerical modelling of the bars

A series of explicit simulations of the current C-T RL SHB set up using Abaqus CAE is presented. The aim of the study is to provide a better understanding of the functioning of the bar and issues detected during the evaluation of the current design. Modelling the equipment also allows the exploration and validation of the proposed enhancements and modifications in the workplan.

A series of explicit transient stress thermal coupled simulations of the SHB designs for HR testing are implemented in Abaqus CAE 6.14. Their main goal is to provide a better understanding of the functioning of the bars and issues detected during the evaluation of the current design. Modelling the equipment also allows the exploration and validation of the proposed enhancements and modifications in the workplan.

The size and complexity of the experimental rig to be modelled and their symmetry allows the use of axisymmetric elements, reducing the number of elements and, in turn, the computational cost of the simulations. In addition, the dimensions of the simulated specimen reflect those of the specimens employed for the experiments. The sample threads are not modelled. The specimen is meshed with 2D linear quadrilateral elements of type CAX4RT (4-node thermally coupled axisymmetric quadrilateral with bilinear displacement and temperature, and reduced integration and hourglass control). The element size in the gauge section is chosen as 0.05 mm in all the simulations to obtain precise comparable results in the region of interest of the tests. The mesh in the bars is finer (0.5 mm) than the strain gage dimensions (2x1.5 mm) to avoid smoothing effects in the wave signals obtained from the simulations. Figure 63 Figure 63. Model of the C-T bar used in the simulations presents the images of the current SHCT apparatus modelling and mesh.

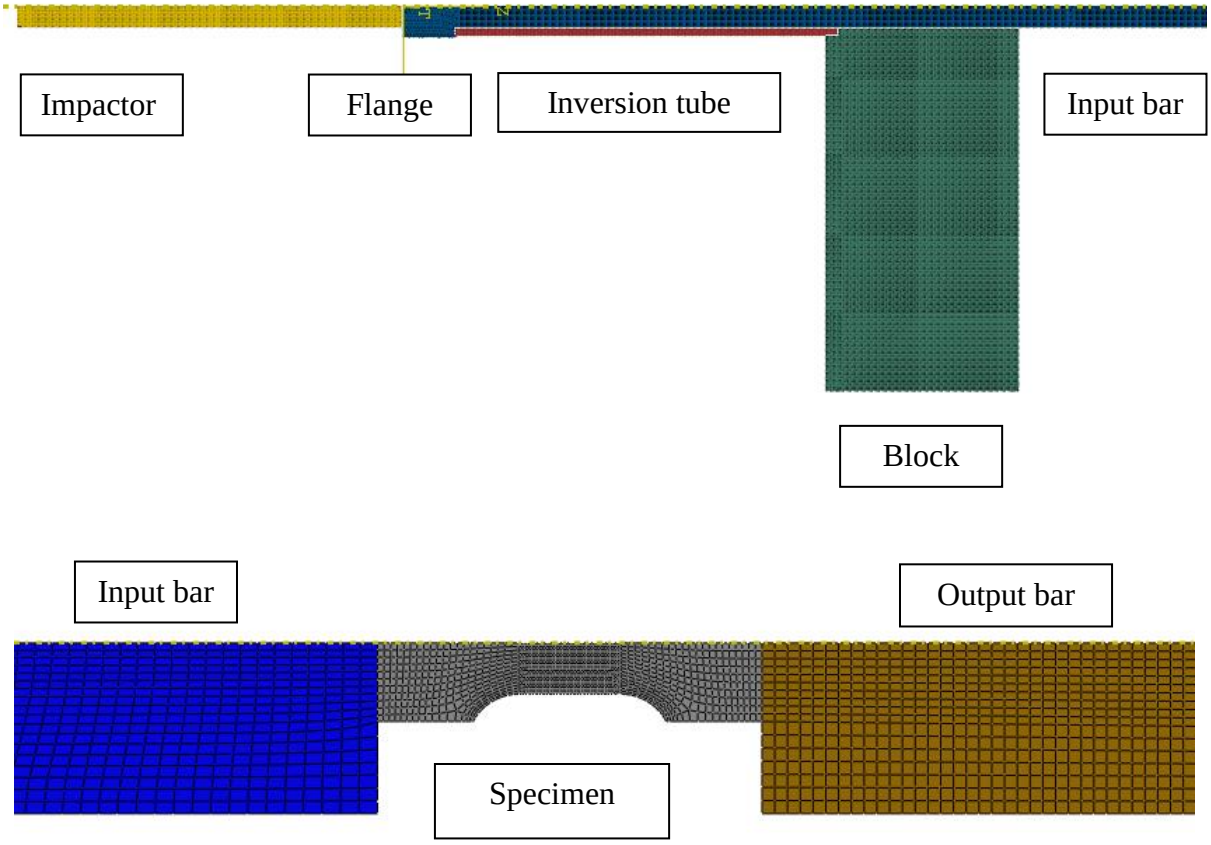

Figure 63. Model of the C-T bar used in the simulations

The interactions in the simulations are defined as frictionless in the tangential direction and as "hard" contact with the default constraint enforcement method in the normal, separation is allowed after contact. Surface to surface explicit contacts between the components are defined setting a kinematic contact method with finite sliding. A contact is defined for each pair of surfaces ensuring that the mesh between the two are close in size, with the slave surface slightly coarser in order to avoid penetration problems during the simulations.

All components of the assembly but the specimen are modelled as isotropic elastic materials, since by design their service conditions will always fall in the elastic regime. A Johnson-Cook plastic material model is chosen for the specimen to account for the plasticity during the testing,

this will not allow the study of the response of Ti-6Al-4V to reverse loading since the Johnson-Cook model doesn't include kinematic hardening, asymmetry and pressure effects but will suffice for the purpose of the present simulations, whose main focus is the study of the generated RL stress waves reaching the specimen.

The dynamic deformation of titanium alloys is associated with a temperature rise due to the conversion of mechanical energy into heat. The integration of the transient stress-thermal balance equation, assuming adiabatic conditions, while neglecting thermoelastic couplings, results in (10):

$$\beta_{int} \int_0^{\alpha} \sigma d\varepsilon_p = \rho c_p \Delta T \qquad (23)$$

where ρ is the material density, c_p is the specific heat capacity and ΔT is the temperature rise. β_{int} is the integral Taylor-Quinney factor [49], which expresses the fraction of the plastic strain energy density converted into heat.

The material properties of all the materials included in the simulations are shown in Table 4:

Table 4 Properties for the material models used in the numerical simulations:

Material	**Conductivity (S/m)**	**Density (kg/m³)**	**Elastic properties**		**Expansion coefficient α**	**Specific heat (J/k)**	**Inelastic heat fraction β_{int} (-)**
			Young Modulus (Pa)	Poisson ratio (-)			
Ti64	6.7	4430	$113{,}8 \cdot 10^9$	0.342	$8.6 \cdot 10^5$	526	0.9
Phosphor bronze elastic	208	8921	$117{,}5 \cdot 10^9$	0.33	$1.78 \cdot 10^5$	380	

	Plastic rate dependent hardening Johnson Cook properties					
	A (Pa)	B (Pa)	n	m	Melt. Temp. (K)	Transition Temperature (K)
Ti64	$896 \cdot 10^6$	$656 \cdot 10^6$	0.5	0.8	1878	298

Two parallel simulations were run under the same exact conditions to evaluate the effectiveness of the momentum trap in the current design, the only difference being the presence or not of the momentum trap at the output. In both cases an impactor velocity of 15 m/s was used. The stress vs time curves in the central section of the specimen are shown in

Figure 64.

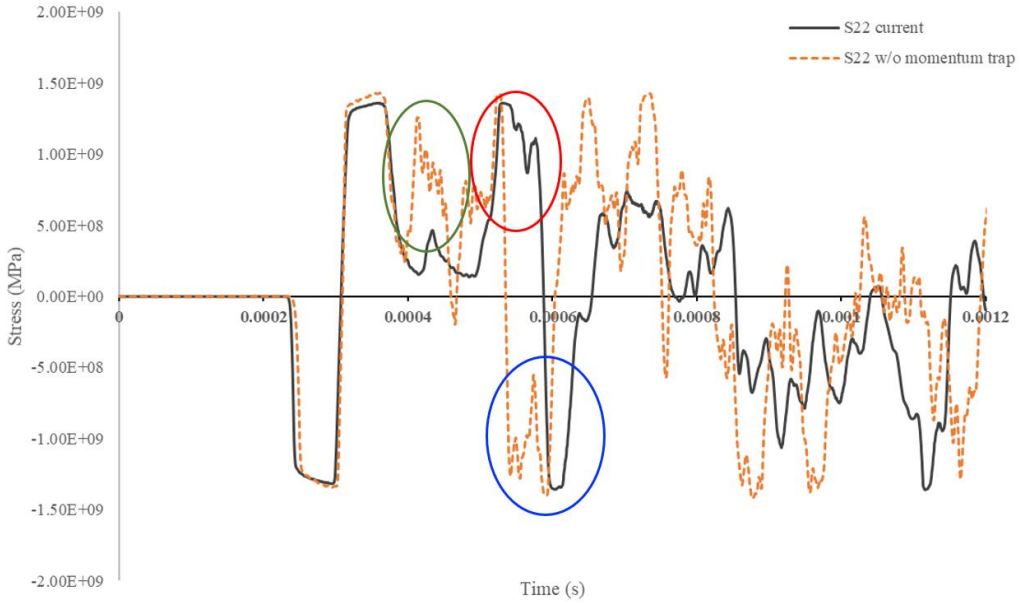

Figure 64. Stress vs time plot at the centre of the specimen of the current rig with and without momentum trap.

The results show that the current equipped momentum trap does indeed work, eliminating part of the tensile reflections that arrive at the specimen (green circle). On the other hand, part of the reflections in tension seen are still present. The second consecutive stress peak in tension (red circle) appears independently of the presence of the momentum trap and was also measured in the experimental tests by the gauges Figure 32. From looking at the wave propagation in the simulations, this appears to be caused by the cross-section discontinuity between the loading bar and the input bar, although further investigation is required to confirm this. As was expected by design, the compressive reflected pulses (blue circle) are not filtered

out and they impact the specimen. Therefore, a potential interest in developing new SHB designs able to control the loading history of the specimen and study the material microstructure post-test emerges.

The presented simulations are set at an impactor velocity on the high end of the spectrum of the velocities contemplated in the experimental study with the intention of exploring the design capabilities of achieving strain in the reverse load. The strains obtained Figure 65 are higher than the ones measured experimentally due to the inevitable energy loss due to wave dissipation and friction between parts. Under ideal conditions and using a high velocity in the impact the current design is only able to accomplish a backwards strain in tension (3%) of about a third of the forwards strain reached in compression (16%). To be able to do strain reversal experiments the design will have to be modified either by the addition of strain control rings that limit the strain in compression or modifying the section area proportions between the incident tube and the loading bar to generate asymmetric stress pulses. The feasibility of this modifications should be studied in the future before selecting a final design.

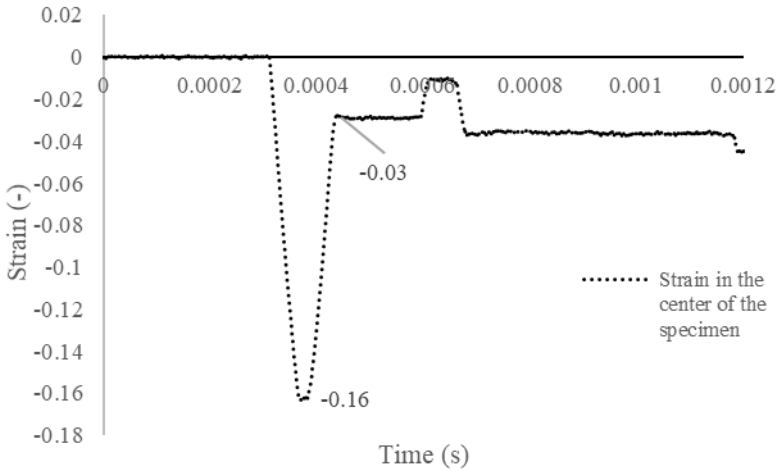

Figure 65. Strain vs time plot at the centre of the specimen.

Temperature effects

The study of B.E. at HR in Ti64 requires to account for adiabatic heating effects. The simulations of the current C-T RL design (section 4.3) allow for an initial exploration of this phenomenon. Figure 66 shows the temperature evolution in the centre of the specimen during reverse loading:

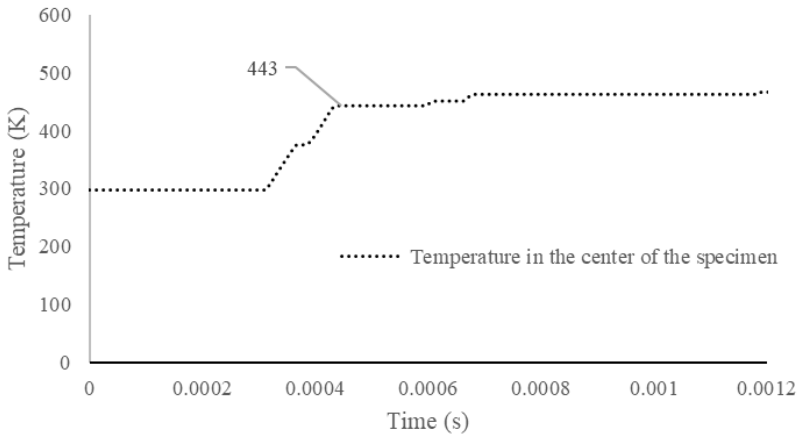

Figure 66 Temperature due to adiabatic heating in a C-T test in the current design.

As seen in Figure 66, the material presents a temperature rise of 143 degrees right after the initial compression-tension cycle, confirming that adiabatic heating effects are sizeable. Hence, temperature is confirmed as being worth including as study parameter. This preliminary result points at necessity to employ experimental techniques with minimal time gaps between loads in the HR RL campaign, future experimental studies should investigate further the role of adiabatic heating in the material response to reverse loading.

Design modifications

The results of the numerical study of the current C-T RL SHB equipment (Figure 64. Stress vs time plot at the centre of the specimen of the current rig with and without momentum trap.) show issues in its effectiveness eliminating unwanted wave reflections in the specimen.

Since the strains employed for the study of B.E are low, the specimens don't break after the first compression-tension cycle, ending up receiving successive wave reflections of non-negligible amplitude. The most relevant reflection detected (see blue circle in Figure 64) consists in a second compressive pulse of similar amplitude as the initial, product of the reflection of the transmitted tensile pulse at the free end of the output bar. This fact impedes the possibility of carrying out tests with a controlled loading history, which would allow much improved studies on the strain history dependency and material texture and microstructural studies of B.E.

A first improvement to address the uncontrolled incidence of reflected waves in the specimen is the addition of a T-shaped flange at the end of the output bar and a concentric tube in contact with it. Figure 67 shows axisymmetric view of the new parts of the assembly at the end of the output bar:

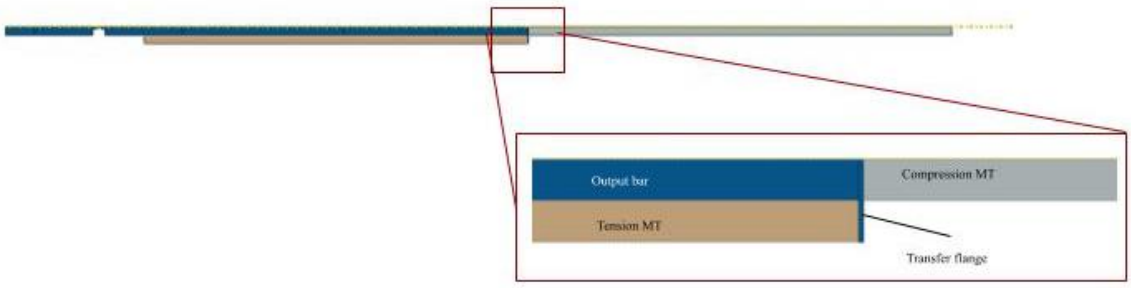

Figure 67 New design for a C-T RL SHB with two momentum traps.

The transfer flange and tension momentum trap are given the same material properties as the output bar and compression momentum trap (Phosphor bronze). The section area of the tension momentum trap matches the area of the output bar in order to get as close as possible to impedance matched contact. The length of the tension momentum trap (longer than 2 times the length of the projectile used) ensures that pulse is completely transmitted before it moves from the flange.

A simulation following the same conditions and parameters as shown in, section 4.3, for the current design is carried out with the new modified bar (impactor velocity 15 m/s).

Figure 68 shows the stress in the centre of the specimen in the new design:

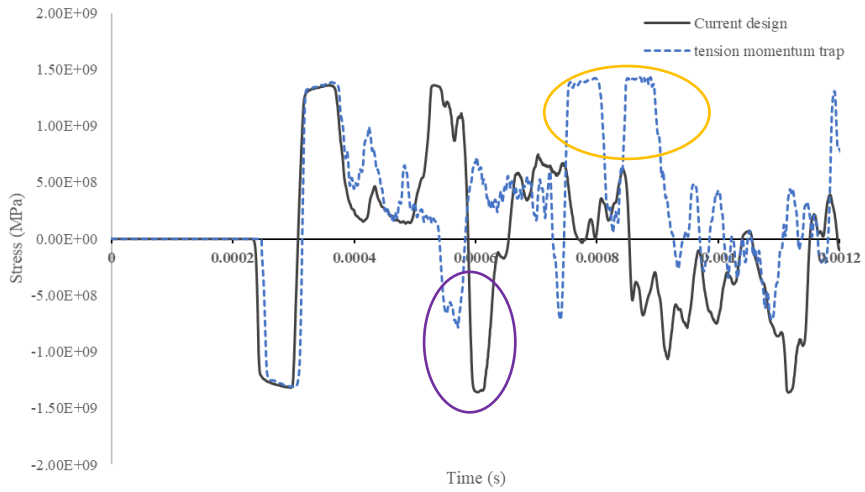

Figure 68 Stress vs time plot at the centre of the specimen of the current rig and the modified design with the addition of a new tensile momentum trap.

The stress measures in central element of the specimen for the new tension momentum trap design look promising. The reflections are in general reduced, and in particular, the compressive wave reflection (purple circle) product of the transmitted tensile wave presents a significantly smaller amplitude, indicating that the new tension momentum trap is able to partially capture it. On the other hand, new tensile reflections are observed (orange circle). Lacking further investigation, they are attributed to the effect of the transfer flange, where the transmitted tensile wave partially transmits to the tensile momentum trap and partially reflects back and forth in the flange until reaching the specimen.

Figure 69 presents the strain plots of both designs in order to evaluate the impact of the newly introduced reflections in the material:

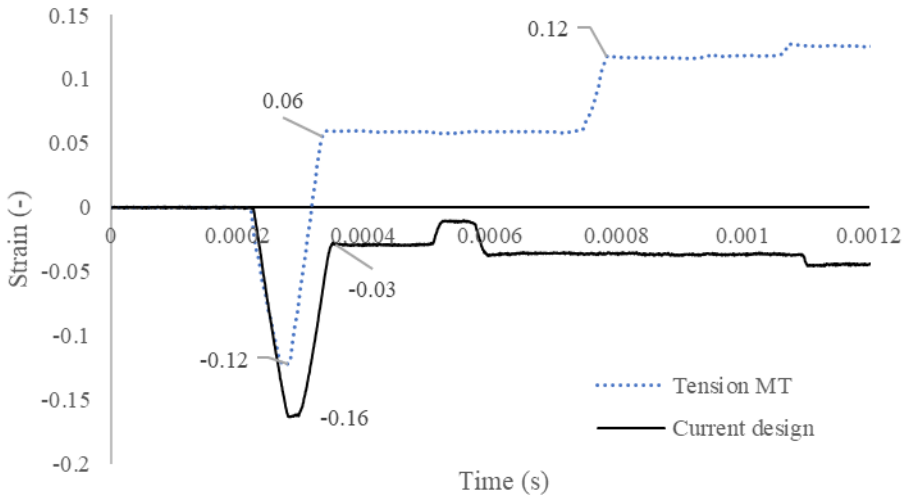

Figure 69 Strain plots of in the centre of the specimen for the current design and the proposed new tension momentum trap.

The new design presents interesting strain results, able to reverse cycle in strain, whereas the current design only could do it in stress. The effect of the reflections marked in orange in Figure

68 can be seen in the second tensile stain jump around t=7s. This supposes a difficulty to overcome in order to achieve a method able to carry out HR reverse loading tests with controlled loading history.

8. References

[1] Deak GI. A study on the causes of the Bauschinger effect. Masssachussetts Institute of technology, 1962:181.

[2] Tuninetti V, Gilles G, Milis O, Pardoen T, Habraken AM. Anisotropy and tension – compression asymmetry modeling of the room temperature plastic response of Ti – 6Al – 4V 2015;67:53–68. https://doi.org/10.1016/j.ijplas.2014.10.003.

[3] Rasband W. The ImageJ User Guide The ImageJ User Guide 2010.

[4] Franck A. Understanding Rheology of Thermoplastic Polymers. TA Instruments 2004;118:1–8.

[5] Ren Y, Yu X, Tan C, Li X. Dynamic mechanical properties and adiabatic shearing behavior of the shock prestrained Ti–6Al–4V alloy having bimodal microstructure. J Alloys Compd 2019;773:1054–63. https://doi.org/10.1016/j.jallcom.2018.09.207.

[6] Frederick CO, Armstrong PJ. A mathematical representation of the multiaxial Bauschinger effect. Mater High Temp 2007;24:1–26. https://doi.org/10.3184/096034007X207589.

[7] Eleiche a. M, Campbell JD. Strain-rate effects during reverse torsional shear. Exp Mech 1976;16:281–90. https://doi.org/10.1007/BF02324016.

[8] Nevill GE, Myers CD. Strain rate effects during reversed loading. J Mech Phys Solids 1968;16:187–94. https://doi.org/10.1016/0022-5096(68)90027-6.

[9] Sowerby R, Uko DK, Tomita Y. A review of certain aspects of the Bauschinger effect in metals. Mater Sci Eng 1979;41:43–58. https://doi.org/10.1016/0025-5416(79)90043-0.

[10] Sathianathan S. The development of Reverse Loading Split Hopkinson Pressure Bar systems for the study of the Dynamic Bauschinger Effect. 2010.

[11] Verleysen P, Peirs J. Quasi-static and high strain rate fracture behaviour of Ti6Al4V. Int J Impact Eng 2017;108:370–88. https://doi.org/10.1016/j.ijimpeng.2017.03.001.

[12] Parry DJ, Walker AG, Dixon PR. Hopkinson bar pulse smoothing. Meas Sci Technol 1995;6:443–6. https://doi.org/10.1088/0957-0233/6/5/001.

[13] Pierron F, Zhu H, Siviour C. Beyond Hopkinson ' s bar Subject Areas : 2014.

[14] Gerlach R, Sathianathan SK, Siviour C, Petrinic N. A novel method for pulse shaping of Split Hopkinson tensile bar signals. Int J Impact Eng 2011;38:976–80. https://doi.org/10.1016/j.ijimpeng.2011.08.007.

[15] Peirs J, Verleysen P, Verbeken K, Coghe F, Degrieck J. High strain rate torsion and Bauschinger tests on Ti6Al4V 2012;709:774–9. https://doi.org/10.4028/www.scientific.net/MSF.706-709.774.

[16] Ogawa K. Impact-tension compression test by using a split-Hopkinson bar. Exp Mech 1984;24:81–6. https://doi.org/10.1007/BF02324987.

[17] Peirs J, Verleysen P, Degrieck J. Study of the dynamic Bauschinger effect in Ti6Al4V by torsion experiments. EPJ Web Conf 2012;26:1023. https://doi.org/10.1051/epjconf/20122601023.

[18] Ogawa K. Mechanical Behaviour of Metals under Tension Compression Loading at High Strain Rate. Int J Plast 1985;1:347–58. https://doi.org/10.1016/0749-6419(85)90020-8.

[19] Nemat-Nasser S, Isaacs JB, Starrett JE. Hopkinson Techniques for Dynamic Recovery Experiments. Proc R Soc A Math Phys Eng Sci 1991;435:371–91.

https://doi.org/10.1098/rspa.1991.0150.

[20] Gerlach R, Kettenbeil C, Petrinic N. A new split Hopkinson tensile bar design. Int J Impact Eng 2012;50:63–7. https://doi.org/10.1016/j.ijimpeng.2012.08.004.

[21] Geng L, Wagoner RH. Role of plastic anisotropy and its evolution on springback. Int J Mech Sci 2002. https://doi.org/10.1016/S0020-7403(01)00085-6.

[22] Bauschinger J. Civilingenieur, 27 (1881) 289. Civil 27 1881:289.

[23] Sowerby R, Uko DK, Tomita Y. A review of certain aspects of the Bauschinger effect in metals. Mater Sci Eng 1979. https://doi.org/10.1016/0025-5416(79)90043-0.

[24] Kostryzhev AG. Bauschinger effect in nb and v microalloyed line pipe steels. University of Birmingham,Theses 2009:206.

[25] Abel A, Muir H. The bauschinger effect and discontinuous yielding. Philos Mag 1972;26:489–504. https://doi.org/10.1080/14786437208227444.

[26] G. Masing and W. Maukch. On Heyn's hardening theory of metals due to inner elastic stresses (in German). Wiss Vero¨ff. Siemens-Konzern, 3, 231–239 (1923) n.d.

[27] G. Masing and W. Maukch. m'issen T'er. Sienaens- Konrern, 4, 244 (1925) n.d.

[28] Buckley SN, Entwistlet KM. the bauschinger effect in super-pure aluminum single crystals and polycrystals. Acta Metallurgica, vol 4, July 1956.

[29] Hencky H. Zngenieur-Archiu 16, 72-76. ijber die berucksichtigung der schubverzerrung in ebenen platten. (German) 1947.

[30] HJ Gough, SJ Wright DH. Some further experiments on the behaviour of single crystals of aluminium under reversed torsional stresses 1926.

[31] Sachs G, Shoji H. Zug-Druckversuche an Messingkristallen (Bauschingereffekt).

Zeitschrift f??R Phys 1927;45:776–96. https://doi.org/10.1007/BF01329555.

[32] Davison H. Research memorandum. Library (Lond) 2000.

[33] Gan W, Bong HJ, Lim H, Boger RK, Barlat F, Wagoner RH. Materials Science & Engineering A Mechanism of the Bauschinger e ff ect in Al-Ge-Si alloys 2017;684:353–72. https://doi.org/10.1016/j.msea.2016.12.020.

[34] Kassner ME, Geantil P, Levine LE. Long range internal stresses in single-phase crystalline materials. Int J Plast 2013;45:44–60. https://doi.org/10.1016/j.ijplas.2012.10.003.

[35] Brown LM. Orowan's explanation of the Bauschinger effect. Scr Metall 1977;11:127–31. https://doi.org/10.1016/0036-9748(77)90291-5.

[36] Mughrabi H. Dislocation clustering and long-range internal stresses in monotonically and cyclically deformed metal crystals. Rev Phys Appliquée 2007;23:367–79. https://doi.org/10.1051/rphysap:01988002304036700.

[37] Yang X, Xiong X, Yin Z, Wang H, Wang J, Chen D. Interrupted Test of Advanced High Strength Steel with Tensile Split Hopkinson Bar Method. Exp Mech 2014;54:641–52. https://doi.org/10.1007/s11340-013-9828-0.

[38] Seeger A. Structure and Mechanical Properties of Metals, HMSO n.d.

[39] Mott NF, Nabarro FRN. Dislocation theory and transient creep. Report on strength of solids. Bristol Phys Soc Conf 1948:1–19. https://doi.org/10.1111/j.1469-8137.1975.tb01370.x.

[40] Thakur A, Nemat-Nasser S, Vecchio KS. Dynamic Bauschinger effect. Acta Mater 1996. https://doi.org/10.1016/1359-6454(95)00385-1.

[41] Khan AS, Pandey A, Gnäupel-Herold T, Mishra RK. Mechanical response and texture evolution of AZ31 alloy at large strains for different strain rates and temperatures. Int J Plast 2011;27:688–706. https://doi.org/10.1016/j.ijplas.2010.08.009.

[42] Kassner ME, Wall MA, Sleeswyk AW. Some observations during in-situ reversed deformation of aluminum single crystals in the HVEM using the X-Y method. Scr Metall Mater 1991;25:1701–6. https://doi.org/10.1016/0956-716X(91)90478-J.

[43] Kassner ME, Wall MA. Microstructure and mechanisms of cyclic deformation in aluminum single crystals at 77 K: Part II. Edge dislocation dipole heights. Metall Mater Trans A Phys Metall Mater Sci 1999;30:777–9. https://doi.org/10.1007/s11661-999-0069-x.

[44] A.W. Sleeswyk, m.r. james dhp. Reversible strain in cycle plastic defprmation. Acta Metall 1978;26:1265–71.

[45] Gould D, Hirsch PB, Humphreys FJ. The Bauschinger effect, work-hardening and recovery in dispersion-hardened copper crystals. Philos Mag 1974;30:1353–77. https://doi.org/10.1080/14786437408207287.

[46] W.F. Hosford RHZ. Metall. Trans. 3 (1972) 113–121 n.d.

[47] P. van Liempt JS. Mater. Sci. Eng. A 662 (2016) 80–87 n.d.

[48] McDowell DL. Mater. Sci. Eng. R. Rep. 62 (2008) 67–123 n.d.

[49] Pederson R (Department of AP and MED of EM. Microstructure and Phase Transformation of Ti-6Al-4V 2002:27–30. https://doi.org/LTU-LIC-0230-SE.

[50] Mughrabi H. A two-parameter description of heterogeneous dislocation distributions in deformed metal crystals. Mater Sci Eng 1987;85:15–31. https://doi.org/10.1016/0025-5416(87)90463-0.

[51] Wielewski E, Arthington MR, Siviour CR, Petrinic N. Characterising the Effects of Strain Rate, Crystallographic Texture and Direction of Loading on the Mechanical Behaviour of Ti-6Al-4V. J Dyn Behav Mater 2015;1:462–71. https://doi.org/10.1007/s40870-015-0040-4.

[52] Wielewski E, Siviour CR, Petrinic N. On the correlation between macrozones and twinning in Ti – 6Al – 4V at very high strain rates. Scr Mater 2012;67:229–32. https://doi.org/10.1016/j.scriptamat.2012.04.026.

[53] Lainé SJ. The Role of Twinning in the Plastic Deformation of Alpha Phase Titanium 2017.

[54] Gerlach R, Siviour CR, Wiegand J, Petrinic N. The Strain Rate Dependent Material Behavior of S-GFRP Extracted from GLARE. Mech Adv Mater Struct 2013;20:505–14. https://doi.org/10.1080/15376494.2011.627646.

[55] Salem AA, Kalidindi SR, Semiatin SL. Strain hardening due to deformation twinning in α-titanium: Constitutive relations and crystal-plasticity modeling. Acta Mater 2005;53:3495–502. https://doi.org/10.1016/j.actamat.2005.04.014.

[56] Salem a a, Kalidindi SR, Doherty RD, Semiatin SL. Strain hardening due to deformation twinning in alpha-titanium: Mechanisms. Work 2006;37:259–68. https://doi.org/10.1007/s11661-006-0171-2.

[57] Handfield L, Dickson JI. The Cyclic Behaviour of Annealed and Prestrained Titanium (Ti-40). Can Metall Q 2014;20:331–8. https://doi.org/10.1179/cmq.1981.20.3.331.

[58] Picu RC, Majorell A. Mechanical behavior of Ti-6Al-4V at high and moderate temperatures - Part II: Constitutive modeling. Mater Sci Eng A 2002;326:306–16. https://doi.org/Pii s0921-5093(01)01507-6\r10.1016/s0921-5093(01)01507-6.

[59] Zhu D, Zhang H, Li DY. Materials Science & Engineering A Effects of nano-scale grain boundaries in Cu on its Bauschinger ' s effect and response to cyclic deformation 2013;583:140–50. https://doi.org/10.1016/j.msea.2013.06.050.

[60] Zhang M, McDowell DL. Crystal plasticity modeling of Ti-6Al-4V and its application in cyclic and fretting fatigue analysis. Mech Eng 2008;Doctor of.

[61] Badr OM, Barlat F, Rolfe B, Lee MG, Hodgson P, Weiss M. Constitutive modelling of high strength titanium alloy Ti-6Al-4 v for sheet forming applications at room temperature. Int J Solids Struct 2016;80:334–47. https://doi.org/10.1016/j.ijsolstr.2015.08.025.

[62] Sinha S, Gurao NP. In situ electron backscatter diffraction study of twinning in commercially pure titanium during tension-compression deformation and annealing. Mater Des 2017;116:686–93. https://doi.org/10.1016/j.matdes.2016.10.060.

[63] Hama T, Nagao H, Kobuki A, Fujimoto H, Takuda H. Materials Science & Engineering A Work-hardening and twinning behaviors in a commercially pure titanium sheet under various loading paths. Mater Sci Eng A 2015;620:390–8. https://doi.org/10.1016/j.msea.2014.10.024.

[64] Sinha S, Gurao NP. Materials Science & Engineering A The role of crystallographic texture on load reversal and low cycle fatigue performance of commercially pure titanium. Mater Sci Eng A 2017;691:100–9. https://doi.org/10.1016/j.msea.2017.03.043.

[65] Chun BK, Kim HY, Lee JK. Modeling the Bauschinger effect for sheet metals, part II: applications. Int J Plast 2002;18:597–616. https://doi.org/10.1016/S0749-6419(01)00047-X.

[66] Livermore Software Technology Corp. LS-Dyna Theory Manual r:11261. vol. 19. 2019.

[67] Key SW, Krieg RD. On the numerical implementation of inelastic time dependent and time independent, finite strain constitutive equations in structural mechanics. Comput Methods Appl Mech Eng 1982;33:439–52. https://doi.org/10.1016/0045-7825(82)90118-9.

[68] Murugesan M, Jung DW. Johnson cook material and failure model parameters estimation of AISI-1045 medium carbon steel for metal forming applications. Materials (Basel) 2019;12. https://doi.org/10.3390/ma12040609.

[69] Bergström J. Plasticity Models. Mech Solid Polym 2015:353–69. https://doi.org/10.1016/b978-0-323-31150-2.00007-8.

[70] Johnson GR, Cook WH. Fracture characteristics of three metals subjected to various strains, strain rates, temperatures and pressures. Eng Fract Mech 1985;21:31–48. https://doi.org/10.1016/0013-7944(85)90052-9.

[71] Bammann DJ, Johnson GC. On the Kinematics of Finite-Deformation Plasticity 1987;13.

[72] Bammann DJ. Modeling temperature and strain rate dependent large deformations of metals. Appl Mech Rev 1990;43:S312–9. https://doi.org/10.1115/1.3120834.

[73] Report F. Development of a Titanium Alloy Ti-6Al-4V Material Model Used in LS-DYNA 2016.

[74] Practices G, Quanti U. A Good Practices Guide for Digital Image Correlation 2018.

[75] Pan B. Digital image correlation for surface deformation measurement : historical developments , recent advances and future goals 2018.

[76] Reu P. All about speckles : Speckle Size Measurement 2014;44:4–5.

[77] Weinong Chen BS. Split hopkinson bar. Design, Testing and Applications. 2011. https://doi.org/10.1007/978-1-4419-7982-7.

[78] De Cola F, Pellegrino A, Glößner C, Penumadu D, Petrinic N. Effect of Particle Morphology, Compaction, and Confinement on the High Strain Rate Behavior of Sand. Exp Mech 2018;58:223–42. https://doi.org/10.1007/s11340-017-0331-x.

[79] Paul JDH, Hoppe R, Appel F. On the Bauschinger effect in TiAl alloys. Acta Mater 2016;104:101–8. https://doi.org/10.1016/j.actamat.2015.10.036.

[80] A.S. argon. chapter 21 - mechanical properties of single-phase crystalline media: deformation at low temperatures,. vol. 25. Fourth. North-Holland: Elsevier B.V.; 1996. https://doi.org/10.1063/1.1771186.

[81] Marcadet SJ, Mohr D. Effect of compression-tension loading reversal on the strain to fracture of dual phase steel sheets. Int J Plast 2015;72:21–43. https://doi.org/10.1016/j.ijplas.2015.05.002.

[82] Karaman I, Sehitoglu. H, Chumlyakov YI, Maier HJ, Kireeva I V. The effect of twinning and slip on the bauschinger effect of hadfield steel single crystals. Metall Mater Trans A Phys Metall Mater Sci 2001;32:695–706. https://doi.org/10.1007/s11661-001-1005-x.

[83] Saleh Y, Margolin H. Bauschinger effect during cyclic straining of two ductile phase alloys. Acta Metall 1979;27:535–44. https://doi.org/10.1016/0001-6160(79)90005-1.

[84] Paul JDH, Hoppe R, Appel F. Acta Materialia On the Bauschinger effect in TiAl alloys. Acta Mater 2016;104:101–8. https://doi.org/10.1016/j.actamat.2015.10.036.

[85] Kay G. Failure Modeling of Titanium-61-4V and 2024-T3 Aluminum with the Johnson-

Cook Material Model. US Dep Transp 2002:27.

[86] Thomas B, Cousins S. Development of Improved Numerical Techniques for High Strain Rate Deformation Behaviour of Titanium Alloys 2016.

[87] Li Z, Gu H. Bauschinger effect and residual phase stresses in two ductile-phase steels. Part I. The influence of phase stresses on the Bauschinger effect. Metall Trans A, Phys Metall Mater Sci 1990;21 A:717–24.

[88] Li Z, Gu H. Bauschinger effect and residual phase stresses in two ductile-phase steels. Part II. The effect of microstructure and mechanical properties of the constituent phases on Bauschinger effect and residual phase stresses. Metall Trans A, Phys Metall Mater Sci 1990;21 A:725–32.

[89] Aifantis EC. A Model for Finite-Deformation Plasticity 1987;117:97–117.

[90] Khan AS, Kazmi R, Farrokh B. Multiaxial and non-proportional loading responses, anisotropy and modeling of Ti-6Al-4V titanium alloy over wide ranges of strain rates and temperatures. Int J Plast 2007. https://doi.org/10.1016/j.ijplas.2006.08.006.